University of Liege
Faculty of Applied Sciences

Implementation of a viscous-inviscid interaction scheme in a finite element full potential solver

Graduation Studies conducted for obtaining the Master's degree in Aerospace Engineering

By Amaury Bilocq

Supervisor : Prof. Dr. Vincent E. Terrapon

Members of the jury: Prof. Dr. Grigorios Dimitriadis

Adrien Crovato

Academic year 2019-2020

Abstract

During preliminary design of an aircraft, high fidelity simulations are not ideal due to their computational cost. Even, RANS simulations are of the order of hours and are not suitable for rapid modifications in the design during early stages. Methods have been developed to lower the computational cost such as the full potential equation. This equation allows to simulate flow in the transonic regime but neglects the viscosity of the fluid. Therefore, the method is not able to predict interesting features such as stall or an accurate drag coefficient.

The purpose of this master's thesis is to implement a viscous correction into a finite element full potential solver *Flow*. A viscous-inviscid interaction scheme has been implemented. The first goal of this work is to define a theoretical model which can handle either incompressible or compressible, attached or separated flows. The viscous formulation is based on the two-equations dissipation integral boundary layer method coupled with a transition formulation of the e^9 type. The viscous solver is coupled to the inviscid solver by a quasi-simultaneous interaction method. This coupling method provides an easy integration without modifying the inviscid solver and allows to compute weak separation regions.

The second goal of the thesis is the numerical implementation of the scheme. The fully coupled non linear system of the viscous solver is discretized by a finite-difference method and is resolved by a robust Newton solution procedure. The results presented demonstrate the ability of *Flow* to predict with accuracy aerodynamic loads and laminar to turbulent transition for attached incompressible and compressible flow cases. Moreover, *Flow* is able to simulate with accuracy separated or highly compressible flows. However, some limits of *Flow* are reached by these extreme cases and are presented in this work. A concise summary of the main outcomes and few hints for future work are provided in the conclusion.

Acknowledgements

First of all, I would like to express my deep gratitude to Adrien who supervised me during the master thesis. He was always available, even by videoconference during the lockdown and ready to answer with kindness to my questions. It was a real pleasure to work with him. Moreover, I would like to thank him for the opportunity to develop a topic which I particularly appreciate.

I would also like to express my gratitude to Prof. Terrapon for his welcome to the MTFC research group and for his wise advice during the group meetings.

Finally, I would like to thank Kathleen, the person who shares my life. She was the only one who believed in me when I wanted to start this second master and who never stopped believing in me throughout those two years. Without her support none of this would have been possible. Despite all the financial difficulties and long evenings of solitude watching me work, she never gave up and was always by my side. It is by being well supported that you become a better version of yourself. For all this, I would like to thank her from the bottom of my heart.

Contents

List of Figures

List of Tables

Nomenclature

Latin Symbols

c_d	Drag coefficient,
C_D	Dissipation coefficient,
C_E	Entrainment coefficient,
C_f	Skin friction coefficient,
c_l	Lift coefficient,
C_{p}	Pressure coefficient,
C_τ	Shear stress coefficient,
c_v	Specific heat at volume constant,
E	Total energy per unit mass,
h	Enthalpy,
h^0	Total enthalpy,
H	Shape parameter,
H^*	Kinetic energy shape parameter,
H^{**}	Density shape parameter,
H_k	Kinematic shape parameter,
H_1	Turbulent shape parameter,
k	Thermal conductivity coefficient,
L	Characteristic length,
M_e	Mach number at the edge of the boundary layer,
M_∞	Freestream Mach number,
N	Amplification ratio,
N_{crit}	Critical amplification ratio,
Re	Momentum thickness Reynolds number,

Re_θ	Momentum thickness Reynolds number,
p	Pressure,
q	Speed,
Q	Heat source,
R	Ideal gas constant,
s	Entropy,
T	Temperature,
Tu	Freestream turbulence intensity,
u_e	Velocity at the edge of the boundary layer,
u_∞	Freestream velocity,
U_S	Slip velocity.

Greek Symbols

α	Angle of attack,
γ	Specific heat ratio,
δ^*	Displacement thickness,
δ^{**}	Density thickness,
ϵ	Streamwise boundary layer coordinate,
η	Normal boundary layer coordinate,
θ	Momentum thickness,
θ^*	Kinetic energy thickness,
μ_e	Dynamic viscosity at the edge of the boundary layer,
ρ	Density,
ρ_e	Density at the edge of the boundary layer,
ρ_∞	Freestream density,
τ	Shear stress,
ϕ	Potential of the velocity,
ψ	Test function,
γ	Vorticity.

Abbreviations

DNS	Direct Numerical Simulation
LES	Large Eddy Simulation
RANS	Reynolds Average Navier Stokes
VII	Viscous Inviscid Interaction

Chapter 1

Introduction

1.1 Motivation

Today, computational fluid dynamics is a powerful aid to aerodynamic design. This tool allows to reduce the wind-tunnel tests and even actual flight tests which are time consuming and expensive, especially for transonic aircraft. Therefore, the amount of time used for design refinement is improved. Depending on the design stage, simulations with various levels of fidelity are applied. The higher order fidelity is the Direct Numerical Simulation (DNS) which solves the Navier-Stokes equations. This kind of simulation is extremely costly since all the turbulence scales are resolved. To lower the computational time, the Large Eddy Simulation (LES) can be applied. By filtering out the smallest turbulence scales, LES allows to use coarser grids. However, both methods capture the chaotic nature of the flow, which is unattractive during the early design stages. At this point in the aircraft design, the Reynolds Average Navier-Stokes (RANS) equations represent the highest level of fidelity that can be of practical interest. These equations allow a statistical representation of the turbulence. RANS simulations reduce the computational costs of the order of hours.

However, it is still not ideal during the preliminary design of the aircraft. To further reduce the computational costs, lower fidelity model where the viscosity of the fluid is neglected were developed. Such models are the Euler equations and by assuming the irrotationality of the flow, the full potential equation. The latter reduces the computational costs in the order of the seconds for subsonic flows and in the order of minutes in the case of transonic flows. The main drawbacks of these inviscid methods are an overestimation of the lift coefficient and their inability to predict a correct drag coefficient.

Therefore, a method that could combine the accurate predictions of a higher fidelity simulation such as

RANS to the low computational costs of the inviscid models is interesting. It would make it possible to correctly estimate the aerodynamic loads during the preliminary design of the aircraft. Then, aircraft performance such as the fuel consumption, the lift generated during take-off and landing would be more predictable and this would reduce the time spent in the early stages of design.
This method is called a *viscous-inviscid interaction* and the aim of this master's thesis is to implement such a method into *Flow*, an inviscid full potential solver developed at the University of Liège by Crovato [1].

1.2 Viscous-inviscid interaction

The viscous-inviscid interaction proposes to split the flow domain into two distinct regions. The first one, the external region, consists in an inviscid flow where the viscosity is neglected. The second one, the internal region, is the viscous region where the viscosity is taken into account. This region models the boundary layer of the body as illustrated in Fig. 1.2.1 and developed by Prandtl [2].

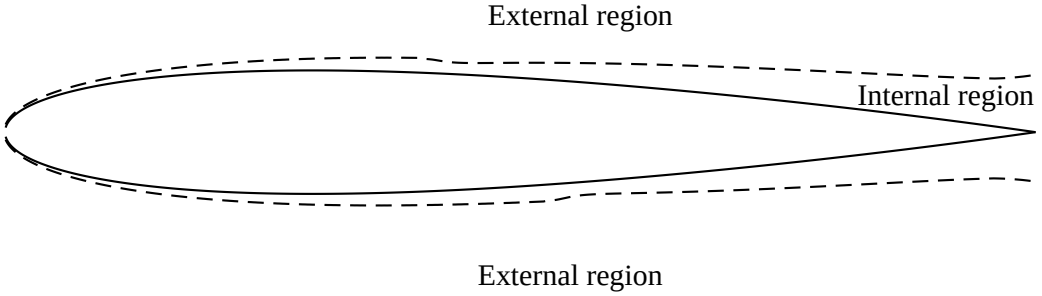

Figure 1.2.1: Separation of the domain in two flow regions, an external, inviscid region and an internal, viscous region.

Both inviscid and viscous models are derived from the Navier-Stokes equations. In the external region, the fluid is considered inviscid and the flow is assumed to be steady, three-dimensional and isentropic. Therefore, the flow is irrotational and the velocity derives from a potential. Thus, the full potential equation is used. The isentropic assumption restricts the flow to the transonic regime with weak shocks. The inviscid formulation is discretized by a finite-element method.

In the internal region, the fluid is viscous and the flow is assumed to be steady, two-dimensional and under the transonic regime. Moreover, the region is extremely thin compared to the length of the body. Therefore, the compressible boundary layer equations are defined. Then, by assuming that the details of the flow inside the boundary layer are not interesting, the boundary layer equations can be integrated

along the thickness of the boundary layer. This gives the so-called integral equations which reduce the number of dimension by one. In the case of this work, there is only one dimension remaining.

However, the splitting of the flow into two regions is only a modeling approach, it does not represents the reality. Therefore, the continuity between the variables at the edge of the inviscid and viscous regions must be enforced. This can be performed by a smart coupling method. Both flows are intrinsically coupled. The boundary layer decelerates the flow due to the viscous effects. Hence, the boundary layer thickens along the body and modifies the velocity inside the inviscid domain. The two variables measuring these effects are the *displacement thickness* δ^* and the *velocity at the edge of the boundary layer* u_e. The first coupling method is the *direct* method. The velocity at the edge of the boundary layer is prescribed by the inviscid solver and then, the viscous solver derives a displacement thickness. In an iterative procedure, the flow in both regions is solved until a solution is found. The main drawback of this method is that it cannot handle separated flows. Hence, an *inverse* method was defined and the displacement thickness is now prescribed to the boundary layer to handle the separation. This method is not suited for this project since it increases drastically the computational time. Finally, a mixture between both methods was introduced with the *semi-inverse* method where the boundary layer displacement is used as an input for the inviscid and viscous solvers. Then, the output is the velocity and the displacement thickness for the next iteration is determined via a relaxation formula. All of the previous methods are called *weak interaction* methods since they assume a hierarchy between the inviscid and the viscous flows.

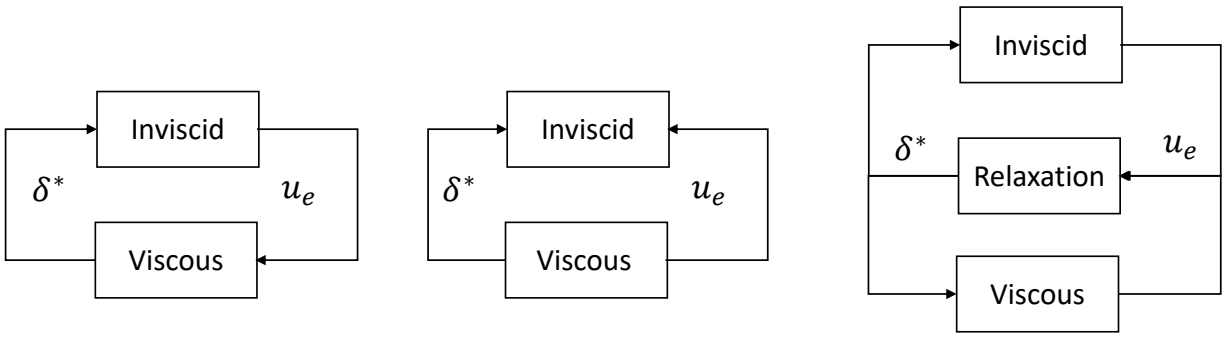

Figure 1.2.2: Weak interaction methods. From the left to the right: the direct interaction, the inverse interaction and the semi-inverse interaction.

However, no hierarchy can be assumed when the flow separates. The velocity and the displacement thickness are equally important and are both unknowns of the system. Hence, a *simultaneous* method was developed to solve the inviscid flow equations and the boundary layer flow equations simultaneously. The main drawback of this method is the complexity of the system in terms of algorithm. Moreover, a

requirement of this work was to be able to implement a viscous correction without modifying the existing inviscid solver.

The last coupling technique is the *quasi-simultaneous* method developed by Veldman [3] and is employed in this work. It assumes that the velocity is an approximation of the external flow. This approximation is modeled as a function of the displacement thickness and is solved simultaneously with the boundary layer equations. The function is called the *interaction law* and its purpose is to help the convergence without influencing the results.

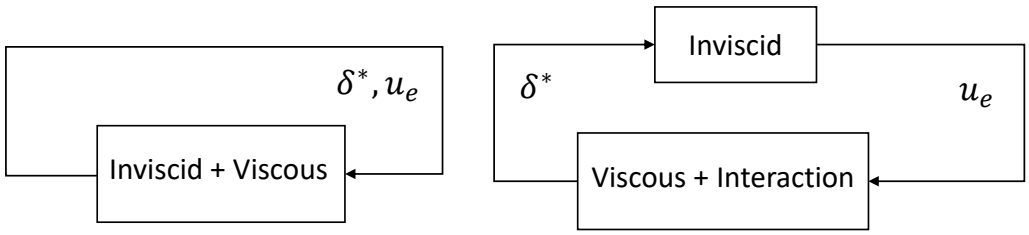

Figure 1.2.3: Strong interaction methods. From left to right: the simultaneous interaction and the quasi-simultaneous interaction.

1.3 Thesis objectives and outlook

The main purpose of the work is to develop a code which can compute a two-dimensional steady attached and separated compressible but not transonic flow around a body by taking into account the viscosity effects. Hence, the various objectives of the master's thesis are the following:

- Establishing the theoretical model which can handle attached and separated, incompressible and compressible flows. Moreover, the model must predict an accurate laminar to turbulent transition. Chapter 2 is consecrated to the derivation of such a model from the Navier-Stokes equations. In a first time, the inviscid model is introduced from the work of Crovato [1]. Then, the viscous model is introduced from the literature. The boundary layer equations are presented and used to derive the integral boundary layer equations. The laminar and turbulent closure relations are given to close the set of equations and the transition model is explained. Chapter 3 focuses on the interaction method used to couple the inviscid and viscous solvers. The blowing velocity and its implementation into the inviscid solver are presented. All the methods are detailed and an interaction law for the quasi-simultaneous interaction is determined.

- Developing the numerical model based on the framework of Crovato [1]. First, the numerical procedure is presented in Chapter 4. The input parameters, the initial and boundary conditions are presented. Then, the equations are discretized with a finite-difference method and the Newton iteration is explained. The procedure to deal with the transitional interval and the wake is shown. After that, the numerical procedure is applied to case studies. The first case is the simulation of an attached incompressible and compressible flow around a NACA 0012 airfoil. Then, the same airfoil is used to simulate a separated flow. The last case study is a simulation of a highly compressible flow around a RAE 2822 airfoil.

Finally, conclusions of the different sections are given in Chapter 6 and hints for future works are introduced.

Chapter 2

Flow models

The aim of the viscous-inviscid interaction is to split the computational domain into two distinct regions. An external region where the flow is assumed to be inviscid and an internal region close to the airfoil where the viscosity is taken into account. Assuming an inviscid external flow helps to reduce the computational cost of the simulation. Two different models are then used to simulate the two regions.
The first section of this chapter will introduce the inviscid formulation. The governing equations are derived and the domain on which the equations are discretized is shown. The second section is consecrated to the formulation of the viscous region which is mainly based on the boundary layer concept. The discretization of this region will be explained in Chapter 4.
The two flow models are based on simplifications of the Navier-Stokes equations. The system is given here in the conservative form

$$\frac{\partial \rho}{\partial t} + \nabla \cdot (\rho \mathbf{u}) = 0, \tag{2.0.1a}$$

$$\frac{\partial \rho \mathbf{u}}{\partial t} + \nabla \cdot (\rho \mathbf{u} \times \mathbf{u}) = -\nabla p + \nabla \cdot \boldsymbol{\tau} + \mathbf{F}, \tag{2.0.1b}$$

$$\frac{\partial \rho E}{\partial t} + \nabla \cdot (\rho E) = \nabla \cdot (k \nabla T) + \nabla \cdot (-p\mathbf{u} + \boldsymbol{\tau} \cdot \mathbf{u}) + \mathbf{u} \cdot \mathbf{F} + Q, \tag{2.0.1c}$$

where ρ is the density, $\mathbf{u}$ is the flow velocity, p is the pressure, $\boldsymbol{\tau}$ is the viscous shear stress tensor, $\mathbf{F}$ represents the body accelerations acting on the continuum which will be neglected in this work, E is the total energy per unit mass, k is the thermal conductivity coefficient, T is the temperature and Q is the heat source.

The stress tensor for a Newtonian fluid is given by

$$\boldsymbol{\tau} = \mu \left(\nabla \mathbf{u} + \nabla \mathbf{u}^{\mathrm{T}} - \frac{2}{3} \mathbf{I} \nabla \cdot \mathbf{u} \right). \tag{2.0.2}$$

The system of equations is closed with state equations from the perfect gas assumption

$$E = c_v T + \frac{1}{2} \mathbf{u}^2, \tag{2.0.3}$$

$$p = \rho R T, \tag{2.0.4}$$

where c_v is the specific heat capacity at constant volume and R is the ideal gas constant.

2.1 Inviscid flow model

This section summarizes the work done by Crovato [1] [4]. The inviscid formulation is already implemented in *Flow* at the beginning of this thesis. Its purpose is the simulation of three-dimensional transonic and inviscid flows.

2.1.1 Full potential equation

First the lagrange identity, the vorticity vector and the first law of thermodynamics are defined respectively

$$\mathbf{u} \cdot \nabla \mathbf{u} = (\nabla \times \mathbf{u}) + \frac{1}{2} \nabla \left(\mathbf{u} \cdot \mathbf{u} \right), \tag{2.1.1}$$

$$\omega = \nabla \times \mathbf{u}, \tag{2.1.2}$$

$$\frac{1}{\rho} \nabla p = \nabla h - T \nabla s, \tag{2.1.3}$$

where h is the enthalpy and s is the entropy of the flow.
Implementing the previous relations into the momentum equation (Eq. 2.0.1b) gives the Crocco's equation

$$\frac{\partial \mathbf{u}}{\partial t} + \omega \times \boldsymbol{u} = T \nabla s - \nabla h^0 - \frac{1}{\rho} \nabla \cdot \tau, \tag{2.1.4}$$

where $H = h + \frac{1}{2}\mathbf{u}^2$ is the total enthalpy.
Assuming a smooth, steady, inviscid and isentropic flow leads to

$$\omega \times \boldsymbol{u} = 0. \tag{2.1.5}$$

Hence, the flow is irrotational and the velocity derives from a potential ϕ such that

$$\mathbf{u} = \nabla\phi, \tag{2.1.6}$$

and the mass conservation (Eq. 2.0.1a) yields to the full potential equation

$$\nabla \cdot (\rho\nabla\phi) = 0. \tag{2.1.7}$$

The fluid density is formulated by the isentropic relation

$$\rho = \rho_\infty \left[1 + \frac{\gamma - 1}{2} M_\infty^2 \left(1 - |\nabla\phi|^2\right)\right]^{\frac{1}{\gamma-1}}, \tag{2.1.8}$$

where ρ_∞ is the freestream fluid density, γ is the heat capacity ratio and M_∞ is the freestream Mach number.

However, the full potential equation is limited to isentropic flow. Since the entropy produced through a shock-wave is related to $\nabla s = \mathcal{O}\left(M_n^2 - 1\right)^3$, where M_n is the normal Mach number. The assumption is valid for transonic flow with weak shock up to $M_n < 1.3$, as explained in Crovato [4].

2.1.2 Solver implementation

The weak formulation of the full potential equation is obtained by multiplying Eq. 2.1.7 by a test function ψ and integrating by part over the domain Ω

$$\int_\Omega \rho\nabla\phi \cdot \nabla\psi dV - \int_\Gamma \overline{\rho\nabla\phi} \cdot \mathbf{n}\psi dS = 0, \quad \forall\psi, \tag{2.1.9}$$

where Γ is the boundary of the volume Ω, $\mathbf{n}$ is the normal to the boundary pointing inside the domain and $\overline{\rho\nabla\phi}$ is the known mass-flux through the boundary. Finite element method is used to discretize the domain Ω and the weak formulation of the full potential equation (Eq. 2.1.9) is defined on each element.

As seen in Fig. 2.1.1, the surface boundary Γ is split into a farfield Γ_f and a body Γ_b boundaries on which a Neumann condition is imposed

$$\int_{\Gamma_\mathrm{f}} \overline{\rho \nabla \phi} \cdot \mathbf{n} \psi dS = \int_{\Gamma_\mathrm{f}} \rho_\infty \mathbf{u}_\infty \cdot \mathbf{n} \psi dS, \tag{2.1.10a}$$

$$\int_{\Gamma_\mathrm{b}} \overline{\rho \nabla \phi} \cdot \mathbf{n} \psi dS = 0, \tag{2.1.10b}$$

where ρ_∞ is the density and $\mathbf{u}_\infty$ is the velocity vector in the freestream. The body boundary will be modified during the viscous-inviscid interaction to take into account the effect of the boundary layer on the external region as seen in Chapter 3. Finally, a Dirichlet condition is applied on the upstream boundary Γ_u

$$\bar{\phi}\big|_{\Gamma_u} = \phi_\infty, \tag{2.1.11}$$

where ϕ_∞ is the freestream potential.

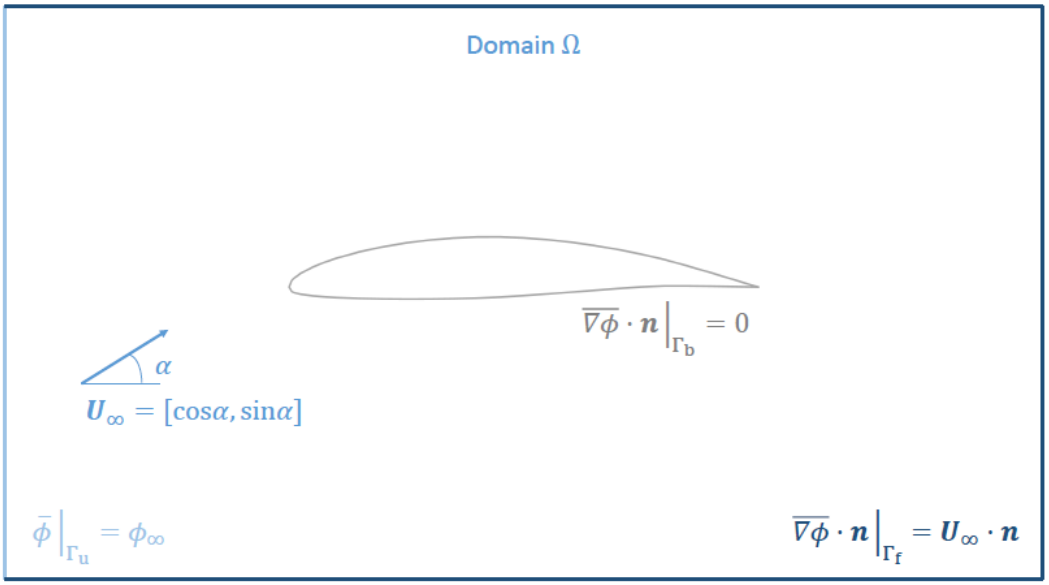

Figure 2.1.1: Computational domain of the inviscid external region. Taken from Crovato [4].

Finally, the Kutta condition must be implemented to allow a potential flow to generate lift. In *Flow*, a flat wake sheet Γ_w from the trailing edge of the lifting body to the farfield boundary downstream is created. Then, different conditions are imposed in order to enforce the Kutta condition. The first condition is to

ensure the continuity of the mass flux on both sides of the wake

$$\int_{\Gamma_w} \rho_u \nabla\phi_u \cdot \mathbf{n}_u dS = -\int_{\Gamma_w} \rho_l \nabla\phi_l \cdot \mathbf{n}_l dS, \tag{2.1.12}$$

where the subscript u refers to the upper side of the wake and the subscript l refers to the lower side of the wake.
The second condition is the zero-pressure jump. For potential flows, this condition simplifies to continuity in the velocity magnitude

$$\int_{\Gamma} (\psi + \Psi) \left[\left[|\nabla\phi|^2\right]\right] dS = 0, \tag{2.1.13}$$

where the double brackets represent a jump between the upper and lower sides of the wake. The test function is enhanced with

$$\Psi = \frac{1}{2}\frac{h}{u_\infty} \left(\mathbf{u}_\infty \cdot \nabla\phi\right). \tag{2.1.14}$$

where u_∞ is the norm of the freestream velocity vector u_∞ and h is a characteristic length. Ψ can be set to zero when dealing with two-dimensional flow, as explained in Crovato [1].

2.2 Viscous flow model

The aim of this section is to derive a theoretical model dealing with steady, two-dimensional, attached and separated compressible flows. Since transonic flows are beyond the scope of the present work, the compressibility effects are taken into account up to the high subsonic limit.

2.2.1 Boudary layer equations

The first major development of viscous-inviscid interaction occurred in 1904 when Prandtl presented the boundary layer model [2]. This model describes the thin layer close to the surface of a body where viscosity cannot be neglected. The first assumption of this model is that the ratio between the inertial and the viscous forces is large. The latter is given by the Reynold number

$$Re = \frac{\boldsymbol{u}L}{\nu}, \tag{2.2.1}$$

where $\boldsymbol{u}$ is the characteristic velocity, L is the characteristic length and ν is the kinematic viscosity. The second assumption is that the boundary layer thickness δ is small compared to the characteristic length L

$$\delta << L. \tag{2.2.2}$$

Moreover, the boundary conditions at the surface are the following

$$y = 0: \quad u = 0; \quad v = 0. \tag{2.2.3}$$

Thus, by performing an order of magnitude analysis with $y \sim \delta$, $x \sim L$ and by applying these assumptions to the conservation laws, the steady two-dimensional compressible boundary layer equations can be derived[1]

$$\frac{\partial}{\partial x}(\rho u) + \frac{\partial}{\partial y}(\rho v) = 0, \tag{2.2.4a}$$

$$\rho u \frac{\partial u}{\partial x} + \rho v \frac{\partial u}{\partial y} = -\frac{\partial p}{\partial x} + \frac{\partial}{\partial y}\left(\mu \frac{\partial u}{\partial y}\right), \tag{2.2.4b}$$

$$\frac{\partial p}{\partial y} = 0 \tag{2.2.4c}$$

$$\rho u \frac{\partial h^0}{\partial x} + \rho v \frac{\partial h^0}{\partial y} = u \frac{\partial p}{\partial x} + \mu \left(\frac{\partial u}{\partial y}\right)^2 + \frac{\partial}{\partial y}\left(\frac{\mu}{\sigma}\frac{\partial h}{\partial y}\right). \tag{2.2.4d}$$

At the edge of the boundary layer, the velocity matches the inviscid one

$$y = \delta: \quad u = u_e; \quad p = p_e. \tag{2.2.5}$$

From Eq. 2.2.4c, the pressure in normal direction is constant inside the boundary layer: $p(\mathrm{x}, \mathrm{y}) = p(\mathrm{x})$. The Euler equations hold at the edge of the boundary layer, where the viscosity has little effect. Thus, the pressure term can be written

$$-\frac{\partial p}{\partial x} = \rho_e u_e \frac{\partial u_e}{\partial x} \tag{2.2.6}$$

where u_e is the 'driving' velocity given by the outer inviscid flow. The main advantage of the boundary layer model is the modification of the elliptic character of the Navier-Stokes equations to an easier handled parabolic character. The stable direction of the boundary layer equations is prescribed by the sign of u and the direction switches in reversed-flow regions. Therefore, various solutions to solve this problem can be taken into account as seen in Chapter 3.

[1] The full derivation can be found in Sells [5].

2.2.2 Integral boundary layer equations

The second major development of viscous-inviscid interaction appeared in 1921. Theodore von Kármán realized that there is not always an interest in the details of the flow inside the boundary layer [6]. Hence, its idea was to integrate the boundary layer equations of 2.2.4 over the boundary layer thickness δ. Therefore, the system of equations is reduced by one dimension but additional unknowns, the integral thicknesses, are introduced.
These parameters represent the distance by which the external flow streamlines must be displaced by the boundary layer to ensure a quantity similar to the one of the inviscid flow, as explained in Anderson [7]. For a compressible flow, the integral thicknesses are

- The displacement thickness for the mass flow: $\delta^* = \int_0^\delta (1 - \frac{\rho u}{\rho_e u_e}) \mathrm{d}\eta$;
- The density thickness for the density: $\delta^{**} = \int_0^\delta (\frac{u}{u_e})[1 - \frac{\rho}{\rho_e}] \mathrm{d}\eta$;
- The momentum thickness for the momentum: $\theta = \int_0^\delta (\frac{\rho u}{\rho_e u_e})[1 - \frac{u}{u_e}] \mathrm{d}\eta$;
- The kinetic energy thickness for the kinetic energy: $\theta^* = \int_0^\delta (\frac{\rho u}{\rho_e u_e})[1 - \frac{u^2}{u_e^2}] \mathrm{d}\eta$;

Finally, a last type of parameters is defined for the integral boundary layer equations

- The shape parameter: $H = \frac{\delta^*}{\theta}$;
- The kinetic energy shape parameter: $H^* = \frac{\theta^*}{\theta}$;
- The density shape parameter: $H^{**} = \frac{\delta^{**}}{\theta}$;
- The kinematic shape parameter: $H_k = \int_0^\delta (1 - \frac{u}{u_e}) \mathrm{d}\eta / \int_0^\delta (\frac{u}{u_e})[1 - \frac{u}{u_e}] \mathrm{d}\eta$;

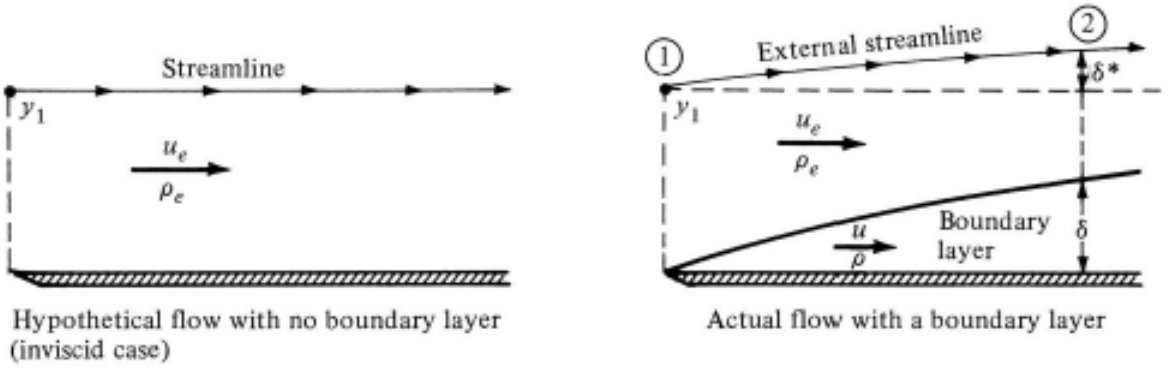

Figure 2.2.1: Representation of the displacement thickness δ^*. On the left, the inviscid case; one the right, the boundary layer case. Taken from Anderson [7].

The integral boundary layer equations are derived by integrating the momentum equation 2.2.4b over δ, using the inviscid condition of the flow at the edge of the boundary layer and the continuity equation. It gives the well-known von Kármán equation

$$\frac{\mathrm{d}\theta}{\mathrm{d}\xi} + \left(2 + H - M_e^2\right) \frac{\theta}{u_e} \frac{\mathrm{d}u_e}{\mathrm{d}\xi} = \frac{C_f}{2}, \tag{2.2.7}$$

where M_e is the Mach number at the edge of the boundary layer and C_f is the dimensionless skin friction

$$C_f = \frac{\tau_w}{\frac{1}{2}\rho u_e^2}, \tag{2.2.8}$$

where $\boldsymbol{\tau_w}$ is the shear stress at the wall. Pohlhausen [8] solved Eq. 2.2.7 by assuming a 4^{th} order polynomials velocity profile with unknown coefficients and additional conditions on the profile. Although it was the method of choice before the advent of computers, this resolution is limited to laminar and attached flows. An easier method to compute laminar and attached flows was proposed by Thwaites [9]. The basic idea is to use empirical correlations to link C_f, θ and H instead of assuming a velocity profile. In the same time, Green's entrainment method, which is based on the entrained mass into the boundary layer [10], was used to compute the turbulent boundary layer. Neither formulation were able to compute separated flows since one equation methods univocally link the shape parameter to the local pressure parameter. In separating flow, this is a nonunique relationship, as stated in Drela [11].

Then, the need of a second equation arises to handle separation. Two solutions are considered in literature. The first one is the kinetic energy shape parameter equation employed in the so-called dissipation integral method [12]

$$\theta\frac{\mathrm{d}H^*}{\mathrm{d}\xi} + \left[2H^{**} + H^*(1-H)\right]\frac{\theta}{u_e}\frac{\mathrm{d}u_e}{\mathrm{d}\xi} = 2C_D - H^*\frac{C_f}{2}, \tag{2.2.9}$$

where the dissipation coefficient is equal to

$$C_D = \frac{1}{\rho_e u_e^3}\int_0^\delta \tau\frac{\partial u}{\partial \eta}\mathrm{d}\eta. \tag{2.2.10}$$

This equation is derived by combining the von Kármán equation with the kinetic energy thickness equation (2.2.11)

$$\frac{\mathrm{d}\theta^*}{\mathrm{d}\xi} + \left(\frac{\delta^{**}}{\theta^*} + 3 - M_e^2\right)\frac{\theta^*}{u_e}\frac{\mathrm{d}u_e}{\mathrm{d}\xi} = 2C_D. \tag{2.2.11}$$

The two-equations dissipation integral method have been used by Drela [11], Nishida [13] Le Balleur [14], Whitfield [15] and many others.

The second method is called the entrainment integral method [16], which is an extension of Green's formulation, and employs a second equation which is different in the laminar and turbulent cases.

For the laminar case, the second equation is the mechanical energy equation

$$\frac{\partial \rho_e u_e^3 \theta^*}{\partial \xi} = C_D \rho_e u_e^3, \tag{2.2.12}$$

while for the turbulent case, the second equation is the Head's entrainement equation [10] [17] (the integrated form of the continuity equation)

$$\frac{1}{\rho_e u_e}\frac{\partial(\rho_e u_e \theta H_1)}{\partial \xi} = C_E, \tag{2.2.13}$$

where the turbulent shape parameter and the entrainment coefficient are respectively

$$H_1 = \frac{\delta - \delta^*}{\theta}, \tag{2.2.14}$$

$$C_E = \frac{1}{\rho_e u_e}\frac{d}{d\xi}\int_0^s \rho u \mathrm{d}\eta. \tag{2.2.15}$$

This method has been used by Bijleveld (Veldman's student) [18], Ye [19], Le Balleur [20] and others.

2.2.3 Boundary layer modeling

In the present work, the two-equation integral formulation based on dissipation integral method is chosen. The main advantage of this method is the use of the same two equations for the laminar and turbulent cases

$$\frac{\mathrm{d}\theta}{\mathrm{d}\xi} + \left(2 + H - M_e^2\right)\frac{\theta}{u_e}\frac{\mathrm{d}u_e}{\mathrm{d}\xi} = \frac{C_f}{2}, \tag{2.2.16a}$$

$$\theta\frac{\mathrm{d}H^*}{\mathrm{d}\xi} + \left[2H^{**} + H^*(1-H)\right]\frac{\theta}{u_e}\frac{\mathrm{d}u_e}{\mathrm{d}\xi} = 2C_D - H^*\frac{C_f}{2}. \tag{2.2.16b}$$

These equations are dependent on three unknowns: θ, H and u_e. The edge velocity u_e can be either prescribed by the inviscid solver for a *direct* coupling, computed by an algebraic equation added to the previous system for a *quasi-simultaneous* coupling or be a total unknown for the other coupling methods as seen in details in Chapter 3.

However, different closure terms are still needed for H^*, H^{**}, C_f and C_D. These terms depend on whether the flow is laminar or turbulent and the following functional dependencies are assumed,

$$C_f = F\left(H_k, M_e, Re_\theta\right), \tag{2.2.17a}$$

$$C_D = F\left(H_k, M_e, Re_\theta\right), \tag{2.2.17b}$$

$$H^* = F\left(H_k, M_e, Re_\theta\right), \tag{2.2.17c}$$

$$H^{**} = F\left(H_k, M_e\right), \tag{2.2.17d}$$

where H_k, the kinematic shape parameter has been derived by Whitfield [21] for adiabatic flows in air. Since correlations (2.2.17) are only defined in terms of velocity profile and not of density profile, H_k is defined by taking a constant density across the boundary layer

$$H_k = \frac{H - 0.290M_e^2}{1 + 0.113M_e^2}. \tag{2.2.18}$$

The last term is the momentum thickness Reynolds number defined as

$$Re_\theta = \frac{\rho_e u_e \theta}{\mu_e}. \tag{2.2.19}$$

The following section exposes the various relations firstly developed by Drela [22] and then improved by Nishida [13]. Since the purpose of this work is neither to derive, nor to validate closure terms, the following equations will just be explained and accepted without any modification.

2.2.3.1 Laminar closure terms

The goal is to link particular unknowns to other variables that are known and validate the relationships by experimental data or analytical solutions. The methodology employed to derive the laminar closure terms is based on velocity profile fitting. In a steady incompressible flow, for a given shape parameter, any laminar velocity profile is similar to the Falkner-Skan profile family. Therefore, the latter is chosen to derive the laminar relationships.

Kinematic energy shape parameter:

$$H^* = \begin{cases} 1.528 + 0.0111\dfrac{(H_k - 4.35)^2}{H_k + 1} - 0.0278\dfrac{(H_k - 4.35)^3}{H_k + 1} \\ \quad -0.0002[(H_k - 4.35)H_k]^2, & H_k < 4.35 \\ 1.528 + 0.015\dfrac{(H_k - 4.35)^2}{H_k}, & H_k \geq 4.35 \end{cases} \tag{2.2.20}$$

In this model, the flow separation occurs at $H_k = 4.35$. As mentioned above, the empirical relationships are very accurate for the incompressible case. Hence, an additional compressibility correction obtained from Whitfield [21] is applied to H^*,

$$H^* = \frac{H^* + 0.025M_e^2}{1 + 0.014M_e^2}. \tag{2.2.21}$$

Density shape parameter:

$$H^{**} = \left(\frac{0.064}{H_k - 0.8} + 0.251\right) M_e^2. \tag{2.2.22}$$

Skin friction coefficient:

$$\overline{C_f} = \begin{cases} \frac{1}{2}\left[-0.07 + 0.0727\dfrac{(5.5 - H_k)^3}{H_k + 1}\right], & H_k < 5.5 \\ \frac{1}{2}\left[-0.07 + 0.015\left(1 - \dfrac{1}{H_k - 4.5}\right)^2\right], & H_k \geq 5.5 \end{cases} \tag{2.2.23}$$

where $\overline{C_f} = C_f \dfrac{Re_\theta}{2}$.

Dissipation coefficient:

$$\overline{C_D} = \begin{cases} 0.207 + 0.00205(4 - H_k)^{5.5}, & H_k < 4 \\ 0.207 - 0.0016\dfrac{(H_k - 4)^2}{1 + 0.02(H_k - 4)^2}, & H_k \geq 4 \end{cases} \tag{2.2.24}$$

where $\overline{C_D} = 2Re_\theta \dfrac{C_D}{H^*}$.

In the case of the skin friction and dissipation coefficients, the Whitfield's compressibility correction drops out. Thus, the only compressibility effect comes from H_k.

2.2.3.2 Laminar to turbulent transition

The purpose of this section is to derive a transition model accurate whether the flow is attached or separated. Different methods are well-known to predict the transition, as the simple Michel's critera [23]

$$Re_\theta > 1.175\left(1 + \frac{22400}{Re_x}\right) Re_x^{0.46}, \tag{2.2.25}$$

or the semi-empirical e^N method pioneered by Smith and Gamberoni [24] and van Ingen [25]

$$N(x) = \ln \frac{A}{A_{crit}}, \tag{2.2.26}$$

where $N(x)$ is the amplification ratio whose value is mostly prescribed at transition according to experiments. The most commonly used value is $N_{crit} = 9$. A is the amplitude envelope of Tollmien-Schlichting waves. The model used in this work is based on the semi-empirical e^N. The latter will be further investigated after a theorical reminder. Since no roughness or freestream turbulence are taking into account,

only the natural transition is investigated. Fig. 2.2.2 illustrates the process of natural transition.

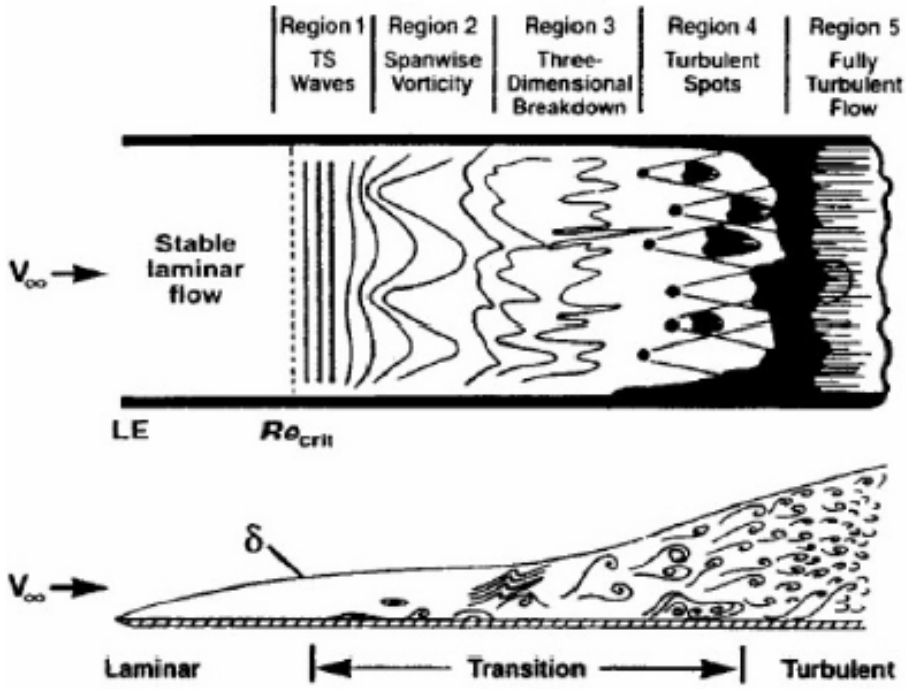

Figure 2.2.2: Illustration of the natural transition process in a boundary layer from Schlichting [26].

When the flow reaches a critical Reynolds number Re_{crit}, unstable two-dimensional Tollmien-Schlichting waves start to grow and superimpose onto the laminar boundary layer flow. Then, three-dimensional disturbances appear due to secondary instabilities. The disturbances remain small and the *linear stability theory* can be used to predict the amplification rate of these disturbances. This lead to vortex formation (Λ *structure*) which will start to break further downstream, as explained in Schlichting [26]. Then, vortices are replaced by turbulent spots and the transition to fully turbulent boundary layer is initiated. Finally, at $Re = Re_{tr}$, the transition is over and the flow is fully turbulent further downstream. For this part composed of region 3 and 4, the disturbances are highly non-linear. Thus, semi-empirical method or DNS are used to model it.

The idea behind the e^N method is that transition occurs when the most unstable Tollmien-Schlichting wave grows by a given amplification factor. In this case, the factor is $e^9 \sim 8100$. As explained previously, 9 is a chosen value. Other values could have been chosen, they depend mostly on the percentage of freestream turbulence T_u. The following relation was developed by Mack [27] in order to link the

maximum amplification ratio N_{crit} to T_u

$$N_{crit} = -8.43 - 2.4 \ln(T_u). \tag{2.2.27}$$

A good historical review of the e^N method and other relations for N_{crit} are given in van Ingen [28]. Then, the last step is to rely the disturbance growth rates to the local boundary layer parameters. Gleyzes [29] proposes a linear approximation of the envelopes of the spatial amplification curves of the Orr-Sommerfeld solutions for the Falkner-Skan profile family. This approximation can be seen in Fig. 2.2.3 and is given by

$$N = \frac{\mathrm{d}N}{\mathrm{d}Re_\theta} (H_k) \left[Re_\theta - Re_{\theta_0} (H_k) \right]. \tag{2.2.28}$$

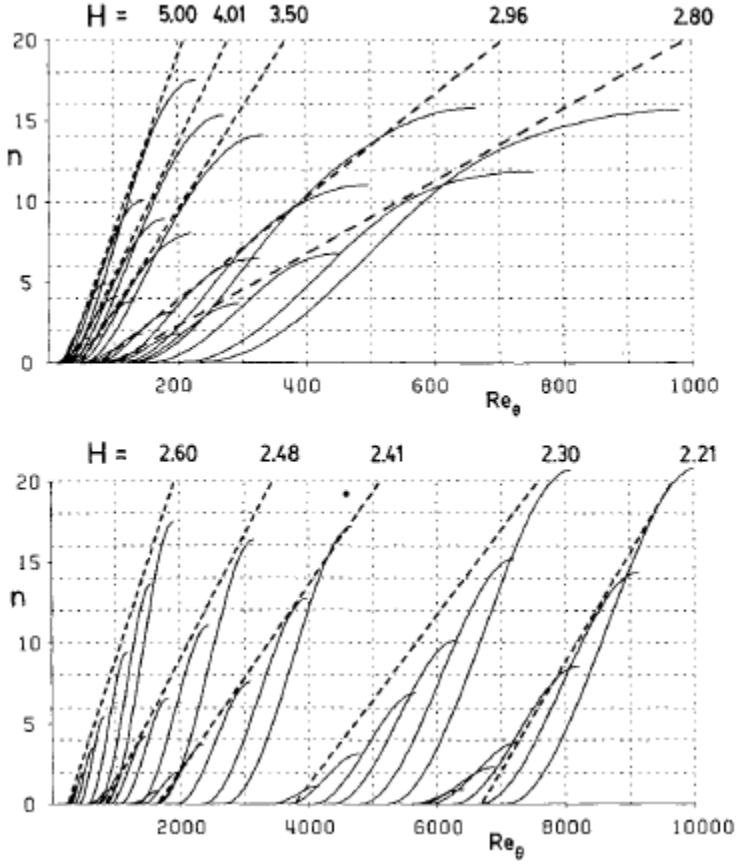

Figure 2.2.3: Linear approximation of the Orr-Sommerfeld solutions for different shape parameters, from Drela[11].

The critical Reynolds number Re_{θ_0} represents the value at which the disturbance appears and starts to grow. Below this value, there is no amplification. The slope $\frac{\mathrm{d}N}{\mathrm{d}Re_\theta}$ and Re_{θ_0} are expressed by the following empirical relations

$$\frac{\mathrm{d}N}{\mathrm{d}Re_\theta} = 0.028(H_k - 1) - 0.0345 \exp\left(-\left(\frac{3.87}{H_k - 1} - 2.52\right)\right)^2, \tag{2.2.29}$$

$$\log_{10} Re_{\theta_0} = 2.492 \left(\frac{1}{H_k - 1}\right)^{0.43} + 0.7 \left(\tanh\left(\frac{14}{H_k - 1} - 9.24\right) + 1\right). \tag{2.2.30}$$

Eq. 2.2.28 directly gives the amplitude ratio N as a function of the streamwise coordinate ξ for an attached flow. This is due to the fact that H_k is a constant and Re_θ depends almost uniquely on ξ for that kind of flow. However, the model must enforce a prediction of the transition for a separated flow. An equation relating the amplification ratio to the streamwise coordinate ξ and empirical relations have been determined by Drela [11]

$$\frac{\mathrm{d}N}{\mathrm{d}\xi}(H_k, \theta) = \left(\frac{\mathrm{d}N}{\mathrm{d}Re_\theta}\frac{\mathrm{d}Re_\theta}{\mathrm{d}\xi}\right)_{att} + A_{sep}, \tag{2.2.31}$$

$$\theta\frac{\mathrm{d}Re_\theta}{\mathrm{d}\xi} = -0.05 + \left(\frac{2.7}{H_k - 1}\right) - \left(\frac{5.5}{H_k - 1}\right)^2 + \left(\frac{3}{H_k - 1}\right)^3 + 0.1 \exp\left(\frac{-20}{H_k - 1}\right), \tag{2.2.32}$$

$$A_{sep} = \frac{1}{\theta}\left[0.086 \tanh\left[1.2\left(\log_{10} -0.3 + 0.35 \exp\left(-0.15(H_k - 5)\right)\right)\right] - \left(\frac{0.25}{H_k - 1}\right)^{1.5}\right], \tag{2.2.33}$$

where A_{sep} is the modified envelope amplification rate which must be added to the normal one in case of a separated flow. Eq. 2.2.31 is solved simultaneously with the momentum and the kinetic energy thickness integral equations for a laminar flow.

2.2.3.3 Turbulent closure

Finding empirical relationships for a turbulent case is far more complicated due to the presence of the Reynolds stresses in Eq. 2.2.16b. The issue comes from the two-layer structure of the boundary layer since the thickness of each layer varies differently depending on the local momentum thickness Reynolds number Re_θ. From this, it is not possible to find a one-parameter velocity profile family which fits all the turbulent boundary layers.

The first step is to define an empirical relation for the skin friction coefficient. The latter is the major scaling parameter for the wall layer. The following relation has been derived firstly by Swafford [30] and

has been improved by Nishida and Drela [13]

$$F_c C_f = \frac{0.3e^{-1.33H_k}}{\left(\frac{\ln Re_\theta}{2.3026}\right)^{-1.74-0.31H}} + 0.00011\left[\tanh\left(4 - \frac{H_k}{0.875}\right) - 1\right], \tag{2.2.34}$$

where $F_c = \sqrt{1 + \frac{\gamma-1}{2}M_e^2}$ and the heat capacity ratio $\gamma = 1.4$ for the air. The kinetic energy shape parameter can be defined by

$$H^* = \begin{cases} 1.5 + \dfrac{4}{Re_\theta} + \left(0.5 - \dfrac{4}{Re_\theta}\right)\left(\dfrac{H_0 - H_k)}{H_0 - 1}\right)^2 \left(\dfrac{1.5}{H_k + 0.5}\right), & H_k < H_0 \\ 1.5 + \dfrac{4}{Re_\theta} + (H_k - H_0)^2 \left[\dfrac{0.007 \ln Re_\theta}{\left(H_k - H_0 + \dfrac{4}{\ln Re_\theta}\right)} + \dfrac{0.015}{H_k}\right], & H_k \geq H_0 \end{cases} \tag{2.2.35}$$

with

$$H_0 = \begin{cases} 3 + \dfrac{400}{Re_0} & H_0 \geq 400, \\ 4, & H_0 < 400. \end{cases} \tag{2.2.36}$$

The density shape parameter is equal to

$$H^{**} = \left(\frac{0.064}{H_k - 0.8} + 0.251\right) M_e^2. \tag{2.2.37}$$

Finally, a last closure relationship is needed for the dissipation coefficient. The difficulty to derive such an expression is due to its dependence on the Reynolds stress distribution across the boundary layer [22]. The method developed by Thomas [12] and Le Balleur [14] consists in separating the contributions to the dissipation coefficient in two: the wall layer and the wake layer. Each contribution is composed by a velocity scale and a stress scale. The following equation illustrates the concept,

$$C_D = \frac{C_f}{2} U_s + C_\tau (1 - Us), \tag{2.2.38}$$

where U_s is an equivalent normalized wall slip velocity and C_τ is the shear stress coefficient. Fig. 2.2.4 shows the representation of a typical turbulent boundary layer profile. The latter is composed of a wall layer where the total shear stress remains almost constant along η and the velocity increases as well as a

wake layer where the opposite happens.

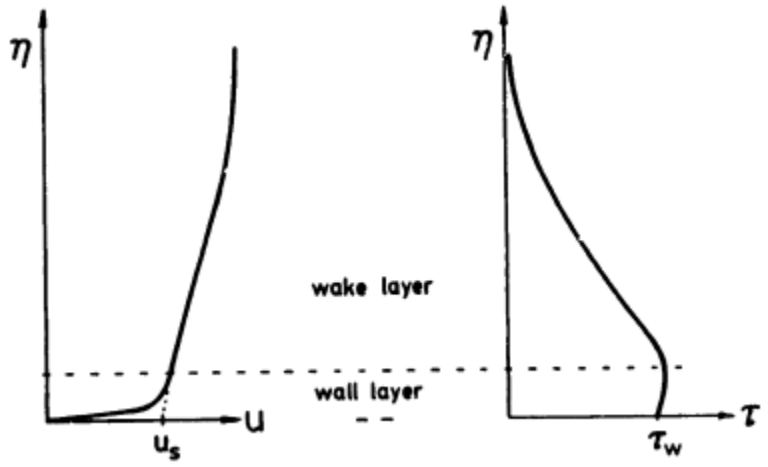

Figure 2.2.4: Typical velocity profile (on the left) and shear stress profile (on the right) inside a turbulent boundary layer, from Drela [22]

The slip velocity U_s is given by

$$U_s = \frac{H^*}{2}\left(1 - 4\left(\frac{H_k - 1}{3H}\right)\right). \tag{2.2.39}$$

The wall contribution of Fig. 2.2.38 containing the skin friction coefficient is consistent with the principle of the universal wall layer since it is determined only by the local boundary layer variable Re_θ and H_k. However, the wake layer containing the Reynolds stresses cannot depends only on the local boundary layer variable. As a matter of fact, the stresses are known to respond slowly to variations and to be affected by the upstream history. Hence, an equation is needed to take into account these upstream history effects

$$\frac{\delta}{C_\tau}\frac{dC_r}{d\xi} = 5.6\left(C_{\tau_{EQ}}^{1/2} - C_r^{1/2}\right) + 2\delta\left\{\frac{4}{3\delta^*}\left[\frac{C_f}{2} - \left(\frac{H_k - 1}{6.7H_k}\right)^2\right] - \frac{1}{u_e}\frac{du_e}{d\xi}\right\}. \tag{2.2.40}$$

Eq. 2.2.40, the shear-lag equation, is a simplification of the stress-transport equation of Bradshaw and Ferriss [31] and it was defined by Drela [32]. This equation models the deviations of the wake layer dissipation coefficient C_D from the local equilibrium value.

Finally, a closure term for the boundary layer thickness δ was obtained by Green [16]

$$\delta = \theta\left(3.15 + \frac{1.72}{H_k - 1}\right) + \delta^*. \tag{2.2.41}$$

And the equilibrium shear stress coefficient is given by

$$C_{\tau_{EQ}} = 0.015 H^* \frac{(H_k - 1)^3}{(1 - U_s) H_k^2 H}. \tag{2.2.42}$$

Finally, the flow in the external and the internal regions has been modeled. The external region is governed by the full potential equation while the internal region is governed by the integral boundary layer equations with different closure terms whether the flow is laminar or turbulent.

An other way to resolve the boundary layer equations could have been to used the self-similarity of the flow coupled with a mixing length turbulent closure. Even if this method gives the exact solution in the case of laminar flows, it creates a lot of unknowns and is way more complex to implement than the integral method. Further informations are given in Moran [33] and Cebeci [34].

The next step is to couple the two formulations and to enforce the continuity of the variables in the interface between the two regions.

Chapter 3

Interaction methods

The last part of the viscous-inviscid interaction consists in the coupling method to connect the inviscid and the viscous regions. Since this separation does not exist physically, an interface must be established to enforce the continuity between the two domains. There is two possibilities to take into account the effect of the boundary layer on the flow. Either by modifying the geometry of the obstacle by the displacement thickness δ^* or by modifying the impermeability boundary condition in the inviscid solver by the so-called *blowing velocity*. Even if the first method requires less steps to be implemented, the second one is preferred because there is no need to change the mesh during the computation.

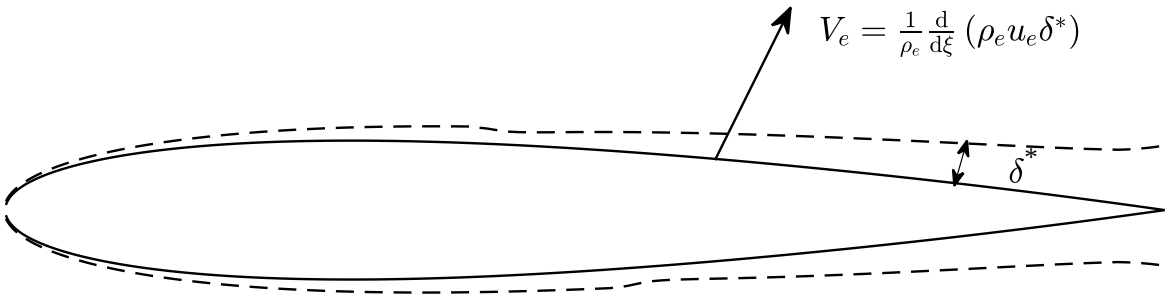

Figure 3.0.1: Representation of the blowing velocity as a boundary condition for the inviscid computation.

As seen in Fig. 3.0.1, the blowing velocity is the velocity component normal to the wall at a distance y large compared to the boundary layer thickness but small compared to the characteristic length L. The concept was defined by Lighthill [35] for incompresible flow. Then, the formulation is adapted for the

compressible flow study in this work. By starting with the definition of the blowing velocity

$$\rho v(\mathrm{x},\mathrm{y}) = \int_0^y \frac{\partial(\rho v)}{y'}(\mathrm{x},\mathrm{y}')\mathrm{d}y'. \tag{3.0.1}$$

Then, by using the continuity equation (2.2.4a)

$$\rho v(x,y) = -\int_0^y \frac{\partial \rho u}{\partial x}(x,y')\,\mathrm{d}y' = -\frac{\partial}{\partial x}\int_0^y \rho u \mathrm{d}y', \tag{3.0.2}$$

$$= -\frac{\partial}{\partial x}\int_0^y \rho(\rho_e U_e - (\rho_e U_e - \rho u))\mathrm{d}y', \tag{3.0.3}$$

$$= -\frac{\mathrm{d}(\rho_e U_e)}{\mathrm{d}x}y + \frac{\partial}{\partial x}\int_0^y \rho_e U_e\left(1-\frac{\rho u}{\rho_e U_e}\right)\mathrm{d}y. \tag{3.0.4}$$

After that, using the definition of the displacement thickness,

$$\delta^* = \int_0^\delta (1-\frac{\rho u}{\rho_e u_e})\mathrm{d}\eta, \tag{3.0.5}$$

and evaluating the normal velocity at the wall[1]: $y = 0$,

$$V_e(\mathrm{x}) = \frac{1}{\rho_e}\frac{\mathrm{d}(\rho_e U_e \delta^*)}{\mathrm{d}x}. \tag{3.0.6}$$

Therefore, the body boundary Eq. 2.1.10b in the inviscid formulation is transformed into

$$\int_{\Gamma_\mathrm{b}} \overline{\rho\nabla\phi}\cdot\mathbf{n}\psi dS = \int_{\Gamma_b} V_e\mathbf{n}\psi dS. \tag{3.0.7}$$

Finally, the viscous-inviscid interaction leads to the following coupled system of equation

$$P: \begin{cases} u_e = E\left(\delta^*\right), \\ u_e = B\left(\delta^*\right), \end{cases} \tag{3.0.8}$$

where E represents the set of equations of the inviscid flow and B the one of the boundary layer. For the next section, the displacement thickness δ^* is used as the output of the boundary layer equations since it is easier to physically understand than the blowing velocity. Fig. 3.0.2 shows the relation between u_e and δ^* for the inviscid flow (E) and the boundary layer flow (B).

[1]Since the blowing velocity is on the scale of the inviscid flow.

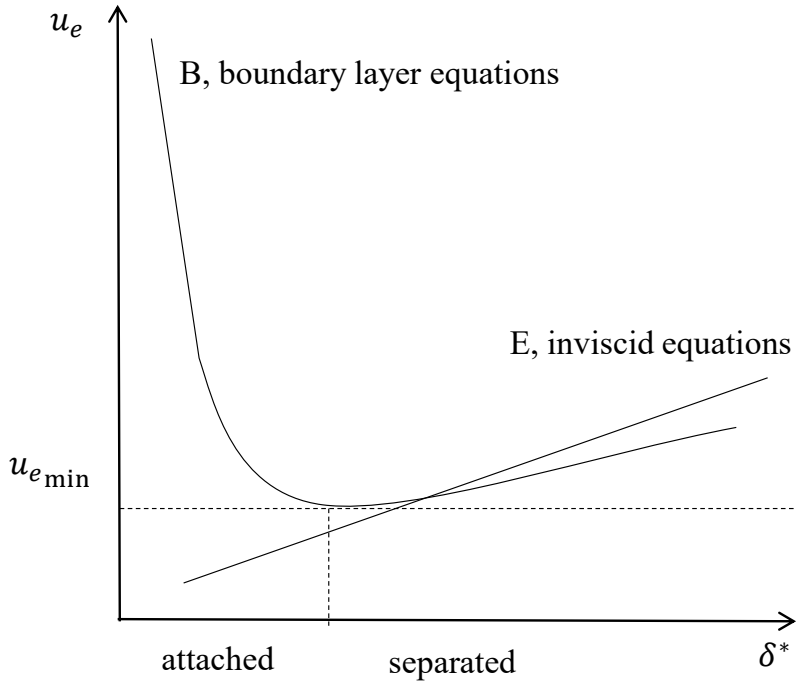

Figure 3.0.2: Illustration of the inviscid and boundary layer flow behaviour to the variation of the displacement thickness δ^*. Adapted from Veldman [36].

The essential feature of this graph is to show that B possesses a minimum edge velocity which corresponds at a flow separation. Below this value, there is no result for the boundary layer equations and the solution totally breaks down. This issue was studied by Goldstein [37] and became the Goldstein-singularity. It shows that if the driving factor of the boundary layer is the velocity prescribed by the inviscid flow, no corresponding displacement thickness can be found at the separation. Therefore, two types of interaction are deduced:

- The weak interactions that assume hierarchy between the flow solutions;
- The strong interactions that do not assume hierarchy between the flow solutions. All unknowns are solved simultaneously in an iterative process.

3.1 Weak interaction methods

3.1.1 Direct method

The direct method is the most simple and intuitive coupling method. The inviscid solver prescribed the edge velocity to the viscous solver, which computes the displacement thickness. Then, the inviscid solver computes a new velocity with the displacement of the boundary layer. The process is repeated until convergence. The direct method can be described by the following system,

$$P_{\text{direct}} : \begin{cases} u_e^n &= E(\delta^{*n-1}), \\ \delta^{*n} &= B^{-1}(u_e^n), \end{cases} \tag{3.1.1}$$

where n is the coupling iteration number. Since the matrix B must be inverted, the determinant should not be zero to avoid singularity. However, Goldstein and others faced such an issue at the point of flow separation. A mathematical analysis of the system (2.2.16),

$$\frac{\mathrm{d}\theta}{\mathrm{d}\xi} + \left(2 + H - M_e^2\right) \frac{\theta}{u_e} \frac{\mathrm{d}u_e}{\mathrm{d}\xi} = \frac{C_f}{2} \tag{3.1.2}$$

$$\theta \frac{\mathrm{d}H^*}{\mathrm{d}\xi} + \left[H^{**} + H^*(1-H)\right] \frac{\theta}{u_e} \frac{\mathrm{d}u_e}{\mathrm{d}\xi} = 2C_D - H^* \frac{C_f}{2} \tag{3.1.3}$$

can be performed by eformulating the system in the form $A\dfrac{\mathrm{d}\boldsymbol{U}}{\mathrm{d}\xi} = R$ with $\boldsymbol{U} = \{\delta^*, H\}^T$, it gives

$$A = \begin{bmatrix} \dfrac{1}{H} & -\dfrac{\delta^*}{H^2} \\ 0 & \dfrac{\delta^*}{H} \dfrac{\mathrm{d}H^*}{\mathrm{d}H} \end{bmatrix}; \quad R = \begin{bmatrix} \dfrac{Cf}{2} - \left(\dfrac{2}{H} + 1 - \dfrac{Me^2}{H}\right) \dfrac{\delta^*}{u_e} \dfrac{\mathrm{d}u_e}{\mathrm{d}\xi} \\ 2C_D - H^* \dfrac{C_f}{2} - \left(\dfrac{H^{**}}{H} + \dfrac{H^*}{H}(1-H)\right) \dfrac{\delta^*}{ue} \dfrac{\mathrm{d}u_e}{\mathrm{d}\xi} \end{bmatrix} \tag{3.1.4}$$

Hence, the system will break down if $\dfrac{\delta^*}{H^2} \dfrac{\mathrm{d}H^*}{\mathrm{d}H} = 0$. Since δ^* and H are never zero, the Goldstein-singularity must appear when $\dfrac{\mathrm{d}H^*}{\mathrm{d}H} = 0$. Fig. 3.1.1 highlights by experiments the existence of a minimum in the curve of H^*. All relations point the minimum near $H \approx 3$ which represents the start of flow separation.

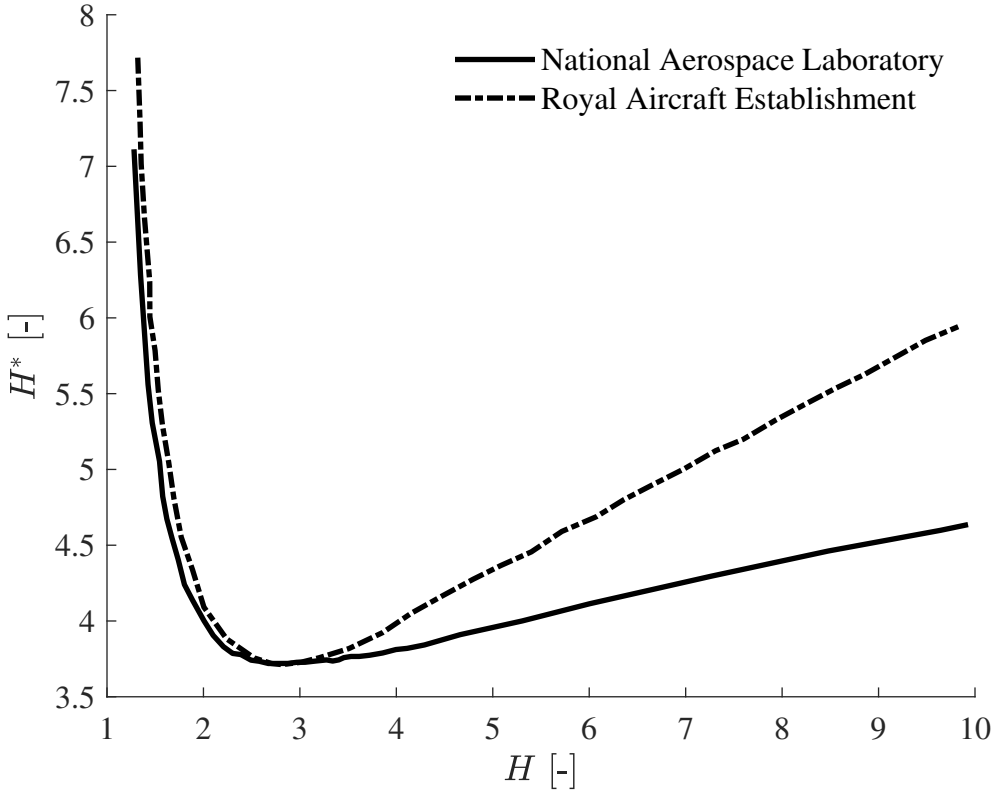

Figure 3.1.1: Experimental data illustrating the relation between the kinetic shape factor and the conventional shape factor. Adapted from Veldman [36].

3.1.2 Inverse method

The first trial of an inverse interaction method was done by Catherall and Mangler [38] in 1966. Instead of the edge velocity, the inviscid solver prescribed a displacement thickness to the boundary layer solver which computes a new edge velocity as following:

$$P_{\text{inverse}} : \begin{cases} \delta^{*n} & = E^{-1}(u_e^{n-1}), \\ u_e^n & = B(\delta^{*n}). \end{cases} \tag{3.1.5}$$

This method helps them to avoid the Goldstein-singularity at the point of flow separation. However, the solution breaks down inside the zone of flow separation. The reason is that, even if the computation survives to the singularity, it is still assuming a hierarchy between the flow solutions. Hence, the numerical procedure is not valid anymore on larger scales of the flow as seen in Fig. 3.1.2.

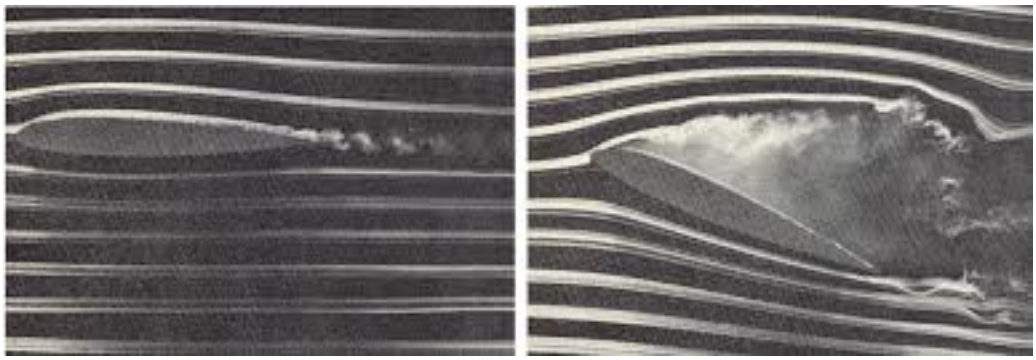

Figure 3.1.2: On the left: boundary layer attached to the airfoil; on the right: boundary layer separated of the airfoil. Taken from Prandtl [39].

Moreover, the major drawback of this method is the need of underrelaxation and the slowness of its convergence as proven by Lock & Williams [40].

Aftosmis et al. [41] show that the two previous methods can be used for more complex configurations by combining a multilevel Cartesian-mesh Euler solver with a viscous solver. The laminar flow is resolved with a direct interaction while the turbulent flow is resolved with an inverse interaction. Their investigations demonstrate the usability of these techniques on 2D supersonic airfoils and full-aircraft configurations.

3.1.3 Semi-inverse method

In this method, the direct solution of the inviscid solver is matched with the inverse solution of the boundary layer equations. The purpose is that two estimates of the edge velocity are given by both solvers. Then, the difference between these velocities is used via a relaxation formula to obtain the new displacement thickness, which is introduced in the two solvers again until convergence. The following system illustrates the process

$$P_{\text{semi-inverse}} : \begin{cases} u_{e_E}^n = E\left(\delta^{*(n-1)}\right), \\ u_{e_B}^n = B\left(\delta^{*(n-1)}\right), \\ \delta^{*n} = \delta^{*(n-1)} + \omega\left(u_{e_B}^n - u_{e_E}^n\right), \end{cases} \tag{3.1.6}$$

where ω is the relaxation factor. The previous system was developed by LeBalleur [20] and Carter [42] for turbulent boundary layer computations. It shows great results for transonic and separated flows.

3.2 Strong interaction methods

3.2.1 Simultaneous method

When Veldman [43] highlighted the strong simultaneous feature of the interaction between inviscid and viscous flows near the separation point, the first proposed coupling technique was a fully-simultaneous coupling. In this method, the inviscid and viscous flows are solved together in one iteration. The outputs for the new step are the edge velocity and the displacement thickness as presented in the following system

$$P_{\text{simultaneous}} : \begin{cases} u_e^n - E\left(\delta^{*n}\right) = 0, \\ u_e^n - B\left(\delta^{*n}\right) = 0, \end{cases} \tag{3.2.1}$$

which is essentially a Newtonian structure. This coupling has very good convergence properties as analysed by Brune et al.[44]. A solution to the system exists as long as $[E - B]$ is not singular that is, when an intersection exists between the curves in Fig. 3.0.2.

The fully-simultaneous interaction is well suited for attached and separated flows since it assumes no hierarchy between the edge velocity and displacement thickness. However, the limitation of the model comes from the limitation of the boundary layer concept itself. Hence, it is not valid anymore in the case of too large flow separations.

The major drawback of this method is the complexity in term of algorithm since both equations of the system above (3.2.1) must be solved simultaneously in one big system of equations. Moreover, the system allows almost no modularity in the solver. It is not possible to modify only the inviscid equations without modifying the boundary layer equations.

The method was developed and applied to supersonic computations by Lees and Reeves [45]. Then, Drela improved the global method by combining a Euler solver with the integral boundary layer equations in Xfoil [32]. Finally, the method was extented for three-dimensional flows by Drela & Nishida [13].

3.2.2 Quasi-simultaneous method

The last technique and the one used in this work is a combination between the direct and the fully-simultaneous method. The quasi-simultaneous coupling has the ease of implementation of the direct method due to the same process of resolution of the system of equations. The inviscid solver prescribes the edge velocity to the boundary layer equations and the latter derives the new displacement thickness for the inviscid calculation. However, the boundary layers equations are solved simultaneously with a simple but good approximation of the inviscid equations. This simpler equation is called an *interaction law* and must model the velocity as a function of the displacement thickness. Moreover, the interaction law must decrease the complexity of the algorithm and describe the flow locally. The following system represents such a method,

$$P_{\text{quasi}-\text{simultaneous}} : \begin{cases} u^n_{e_B} - I\left(\delta^*\right) = u^{n-1}_{e_B} - I\left(\delta^{*n-1}\right), \\ u^n_{eB} - B\left(\delta^{*n}\right) = 0, \\ u^n_{e_E} - E\left(\delta^{*n}\right) = 0, \end{cases} \tag{3.2.2}$$

where I, the interaction law, is used in defect formulation to not influence the final converged result. Hence, it is only improving the rate of convergence. Moreover, it allows to treat the velocity as an unknown in the viscous solver. Therefore, there is no hierarchy between the flow solutions and the method can handle attached and separated flow in the same way as the fully-simultaneous method. This idea of a quasi-simultaneous interaction was developed by Veldman [3] and has been used by Cebeci et al. [46], Bijleveld [18] and others.
The main remaining objective is to find a suitable interaction law which is easy to implement but still allows a robust coupling between the two solvers.

3.3 The interaction law

3.3.1 Behaviour of the interaction law

A solution to the quasi-simultaneous method exists if the curve of the boundary layer equations and the one of the interaction law have an intersection, as seen in Fig. 3.3.1. Physically, the absence of intersection means that the flow is highly separated and that the assumption of the boundary layer is not valid anymore. However, as shown in Chapter 4, such a singularity can still hold numerically.

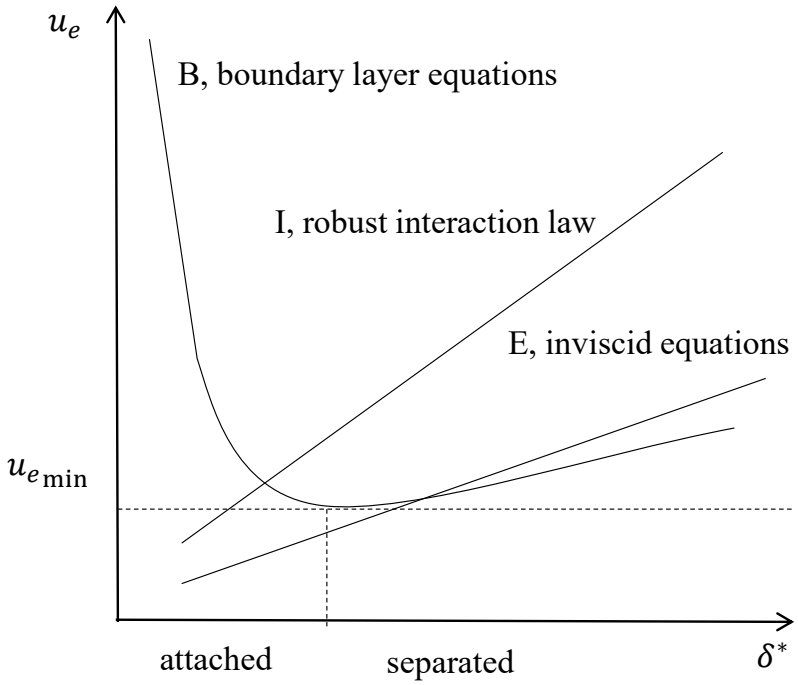

Figure 3.3.1: Illustration of the variation of the edge velocity u_e according to the displacement thickness δ^* for the boundary layer equations, inviscid equations and the interaction law. Adapted from Veldman [36].

Tthe interaction law must satisfy a few criteria. The relation must be linear and steep enough to meet the boundary layer equations curve. Moreover, the steeper the curve, the faster the convergence, as stated by Veldman [3]. Then, the interaction law must link the external flow velocity to the displacement thickness

$$I: \quad u_e = f\left(\delta^*\right). \tag{3.3.1}$$

The triple-deck theory described below allows to connect the local influence of the inviscid flow to the displacement thickness of the boundary layer.

3.3.2 Triple-deck theory

Veldman based the derivation of the interaction law on the triple deck theory, developed independently by Stewardson and Williams [47], Messiter [48] and Neiland [49]. This theory decomposes the boundary layer in three distinct layers:

- A viscous sublayer (lower deck) of thickness $\mathcal{O}(Re^{-5/8})$ gouverned by the boundary layer equations;
- An inviscid middle layer (main deck) of thickness $\mathcal{O}(Re^{-1/2})$ where a vertical shift of the oncoming velocity profile happens due to the displacement effect of the viscous sublayer;
- A top layer (upper deck) of thickness $\mathcal{O}(Re{-}3/8)$ where the flow is assumed irrotational and inviscid. Therefore, this layer can be described with a potential flow equation based on thin airfoil theory.

The information is distributed from the lower to the upper deck. Velocity perturbations are transmitted from the lower deck to the main deck. In this layer, the perturbations are seen as a displacement of the streamlines which is transmitted to the upper deck. This displacement produces a disturbance of pressure which is transmitted back to the lower deck powering the velocity disturbances. Hence, at the point of flow separation, the boundary layer becomes as important as the inviscid flow. The latter is not driving the boundary layer anymore. Fig. 3.3.2 illustrates the concept of the triple deck boundary layer.

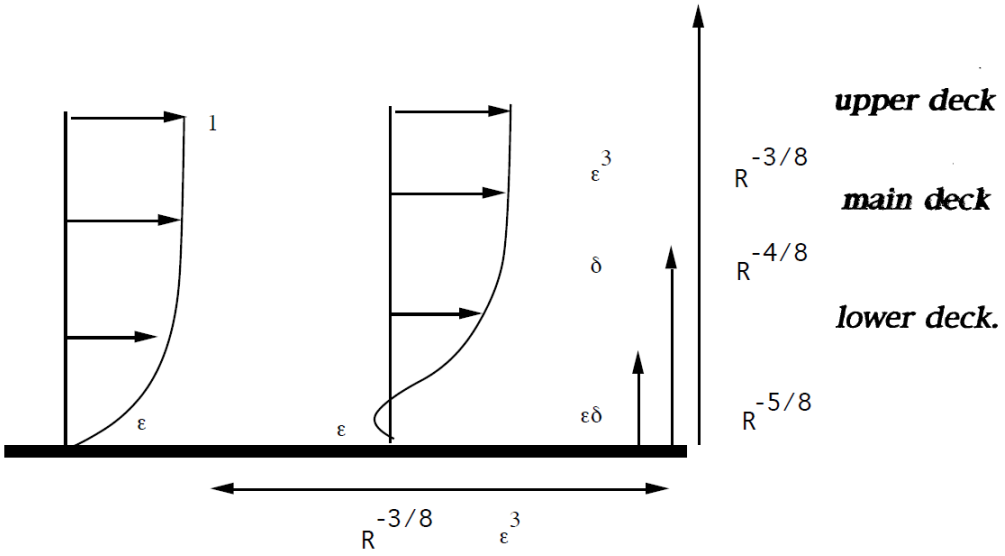

Figure 3.3.2: Illustration of the triple deck theory from Lagrée [50]. The thickness of the lower, main and upper deck are represented.

The major outcome of the theory is the possibility to couple the velocity at the top of the main deck (depending on the displacement thickness) and the one at the bottom of the upper deck (depending on the inviscid velocity)

$$P(x) = \frac{1}{\pi}\int_{-\infty}^{\infty}\frac{G'(\xi)}{x-\xi}\mathrm{d}\xi, \tag{3.3.2}$$

where $P(x_\alpha)$ is the pressure in the main deck, $G'(\xi)$ is a function related to the displacement thickness, ξ is the streamwise coordinate and x is the position of the singularity.

3.3.3 Derivation of the law

Since the purpose of this work is not to define a new interaction law, only the major steps are shown in this section. The derivation of the interaction law was performed by Coenen [51] and Veldman [52] and a good explanation can be found in [18]. They apply a panel method for the discretization of the external flow in order to use thin airfoil theory.

From Eq. 3.3.2, Veldman [52] derives the first interaction law

$$I[\delta^*] = \frac{1}{\pi}\int_{\Gamma}\frac{d\delta^*}{d\xi}\frac{\mathrm{d}\xi}{x-\xi}. \tag{3.3.3}$$

Coenen [51] transforms the previous relation by discretizing it with N number of panels in order to obtain an expression for the velocity

$$u_{e_i} = \sum_{k=1}^{N+1}\mathcal{A}^u_{ik}q_{e_k}\delta^*_{x_k} + u_{0_{e_i}}, \tag{3.3.4}$$

where q_e is the absolute value of the velocity. This formula takes into account the singularity at x = ξ. Moreover, the matrix $\mathcal{A}^u_{ik}$ contains the effect of the various panels on the point i where the velocity is calculated. Coenen [51] shows that the matrix is positive definite and diagonally dominant.
From triple deck theory, only the local influence can be considered to derive the interaction law. Therefore, the diagonal elements of $\mathcal{A}^u_{ii}$ are sufficient [51]. The last requirement is a large slope of I. Coenen shows that by using the minimum number of diagonals from matrix $\mathcal{A}$ to approximate the flow, the slope of I will be larger than the slope of E.
The first equation of the quasi-interaction method (system 3.2.2 is

$$u^n_{e_B} - I(\delta^{*n}) = u^{n-1}_{e_E} - I\left(\delta^{*n-1}\right). \tag{3.3.5}$$

When, by applying the interaction law of Eq. 3.3.4 at point i

$$u_{e_B}^n - \mathcal{A}_{ii}^u q_{e_i}^n \delta_i^{*n} = u_{e_E}^{n-1} - \mathcal{A}_{ii}^u q_{e_i}^n \delta_{x_k}^{*(n-1)}. \tag{3.3.6}$$

Then, the element $\mathcal{A}_{ii}^u$ is given by Veldman [52] as

$$\mathcal{A}_{ii}^u = \frac{4}{\pi \Delta x}, \tag{3.3.7}$$

where Δx is the mesh size. Finally, the absolute value of the velocity can replaced by the freestream velocity since the interaction law has no influence on the converged result. The law is equal to the following algebraic equation

$$\left(u_e + \frac{4u_\infty}{\pi \Delta x}\delta^*\right)^{(\text{new})} = \left(u_e + \frac{4u\infty}{\pi \Delta x}\delta^*\right)^{(\text{old})}. \tag{3.3.8}$$

3.3.4 Mathematical analysis

The same mathematical analysis as for the direct method is performed. However, the interaction law will now be taken into account in the integral boundary layer equations (2.2.16). To do so, the interaction law equation is substituted into the system by its derivative form

$$u_e - c\delta^* = E; \quad E = u_{ext} - \alpha_{ext}^*; \quad c = \frac{4u_\infty}{\pi \Delta x} > 0; \tag{3.3.9}$$

$$=> \frac{\mathrm{d}u_e}{\mathrm{d}\xi} = c\frac{\mathrm{d}\delta^*}{\mathrm{d}\xi} + \frac{\mathrm{d}E}{\mathrm{d}\xi}, \tag{3.3.10}$$

where the assumption of a constant c along the streamwise direction is assumed. Obviously, it is only true for equidistant grids. However, the interaction law has no effect on the converged result hence, neither does the assumption. Therefore, for the unknowns $\boldsymbol{U} = \{\delta^*, H\}^T$, the integral boundary layer equations can be rewritten as

$$\frac{1}{H}\frac{\mathrm{d}\delta^*}{\mathrm{d}\xi} - \frac{\delta^*}{H^2}\frac{\mathrm{d}H}{\mathrm{d}\xi} + \left(2 + H - M_e^2\right)\frac{\delta^*}{Hu_e}\left(c\frac{\mathrm{d}\delta^*}{\mathrm{d}\xi} + \frac{\mathrm{d}E}{\mathrm{d}\xi}\right) = \frac{C_f}{2} \tag{3.3.11}$$

$$\frac{\delta^*}{H}\frac{\mathrm{d}H^*}{\mathrm{d}H}\frac{\mathrm{d}H}{\mathrm{d}\xi} + \left(2H^{**} + H^*(1-H)\right)\frac{\delta^*}{Hu_e}\left(c\frac{\mathrm{d}\delta^*}{\mathrm{d}\xi} + \frac{\mathrm{d}E}{\mathrm{d}\xi}\right) = 2C_D - H^*\frac{C_f}{2} \tag{3.3.12}$$

Thus, in the matrix form $A\dfrac{\mathrm{d}\boldsymbol{U}}{\mathrm{d}\xi} = R$:

$$A = \begin{bmatrix} \dfrac{1}{H} + c\left(\dfrac{2}{H} + 1 - \dfrac{Me^2}{H}\right)\dfrac{\delta^*}{u_e} & -\dfrac{\delta^*}{H^2} \\ c\left(\dfrac{2H^{**}}{H} + \dfrac{H^*}{H}(1-H)\right)\dfrac{\delta^*}{u_e} & \dfrac{\delta^*}{H}\dfrac{\mathrm{d}H^*}{\mathrm{d}H} \end{bmatrix}; \tag{3.3.13}$$

$$R = \begin{bmatrix} \dfrac{Cf}{2} - \left(\dfrac{2}{H} + 1 - \dfrac{Me^2}{H}\right)\dfrac{\delta^*}{u_e}\dfrac{\mathrm{d}E}{\mathrm{d}\xi} \\ 2C_D - H^*\dfrac{C_f}{2} - \left(\dfrac{2H^{**}}{H} + \dfrac{H^*}{H}(1-H)\right)\dfrac{\delta^*}{u_e}\dfrac{\mathrm{d}E}{\mathrm{d}\xi} \end{bmatrix} \tag{3.3.14}$$

To avoid and prevent any singularity, the determinant of the matrix A must be greater than zero:

$$\frac{1}{H}\frac{\mathrm{d}H^*}{\mathrm{d}H} + \frac{c\delta^*}{u_e}\left[\left(\frac{2}{H} + 1 - \frac{Me^2}{H}\right)\frac{\mathrm{d}H^*}{\mathrm{d}H} + \left(\frac{2H^{**}}{H} + \frac{H^*}{H}(1-H)\right)\right] > 0 \tag{3.3.15}$$

And finally, a condition on c can be determined:

$$c > \frac{-\dfrac{u_e}{\delta^* H}\dfrac{\mathrm{d}H^*}{\mathrm{d}H}}{\left[\left(\dfrac{2}{H} + 1 - \dfrac{Me^2}{H}\right)\dfrac{\mathrm{d}H^*}{\mathrm{d}H} + \left(\dfrac{2H^{**}}{H} + \dfrac{H^*}{H}(1-H)\right)\right]} \tag{3.3.16}$$

Fig.3.1.1 shows that $\dfrac{\mathrm{d}H^*}{\mathrm{d}H} < 0$ for attached flows and > 0 for separated flows. Moreover, the second term of the denominator is always negative since H is always higher than 1 and H^* and H^{**} are always positive. Hence, a sign analysis illustrates than if c is positive, the condition is fulfilled automatically for attached flows. However, the right-hand side of the condition can become positive for separated flows. Thus, a large value of c is required and the simulation can breakdown for coarse grids. Therefore, the mesh size is fixed by the condition of the flow. The main issue is that, for transonic application, the mesh size is also determined by the size of the shock.

This chapter concludes the theoretical analysis of the viscous-inviscid interaction. The viscous solver has been formulated and coupled with the inviscid solver by a quasi-simultaneous interaction. The next chapter will explain the numerical implementation of the model into *Flow*.

Chapter 4

Numerical Simulation

In this chapter, the theoretical formulation of the viscous-inviscid interaction scheme are implemented in *Flow*. The procedure of discretization of the integral boundary layer equations by a finite-difference method is introduced. The techniques employed to stabilise the numerical computation are explained and issues with the initial conditions from the inviscid solver are shown. Finally, the convergence is defined.

4.1 Solution procedure

Fig. 4.1.1 illustrates the solution procedure of the viscous-inviscid interaction implemented in *Flow*. The first step is the prescription of the input parameters by the user. Step 2 is the computation of the inviscid equations hence, it will not be detailed here. More details can be found in Crovato [1].
Then, steps 3 & 4 & 5 are consecrated to the initialization of the simulation. This initialization consists in the manipulation of the data from the inviscid solver, the processing of values that are used as initial conditions and the determination of the boundary conditions for the airfoil and for the wake.
After that, the boundary layer equations are solved in step 6. To do so, they are discretized and then, resolved with a Newton procedure. The simulation around the airfoil is performed in a first time. During the simulation, the transition is checked at every station. When transition occurs, a special processing is done at this location. Then, the simulation of the wake is performed. For the case studied in this project, the wake is assumed to be always turbulent. A convergence analysis is done after the resolution of the boundary layer equations and if the solution is converged, the simulation stops and the outputs of the viscous-inviscid interaction are post-processed. If not, the new blowing velocites are given as boundary conditions to the inviscid solver and a new coupling iteration is done until the convergence is reached.

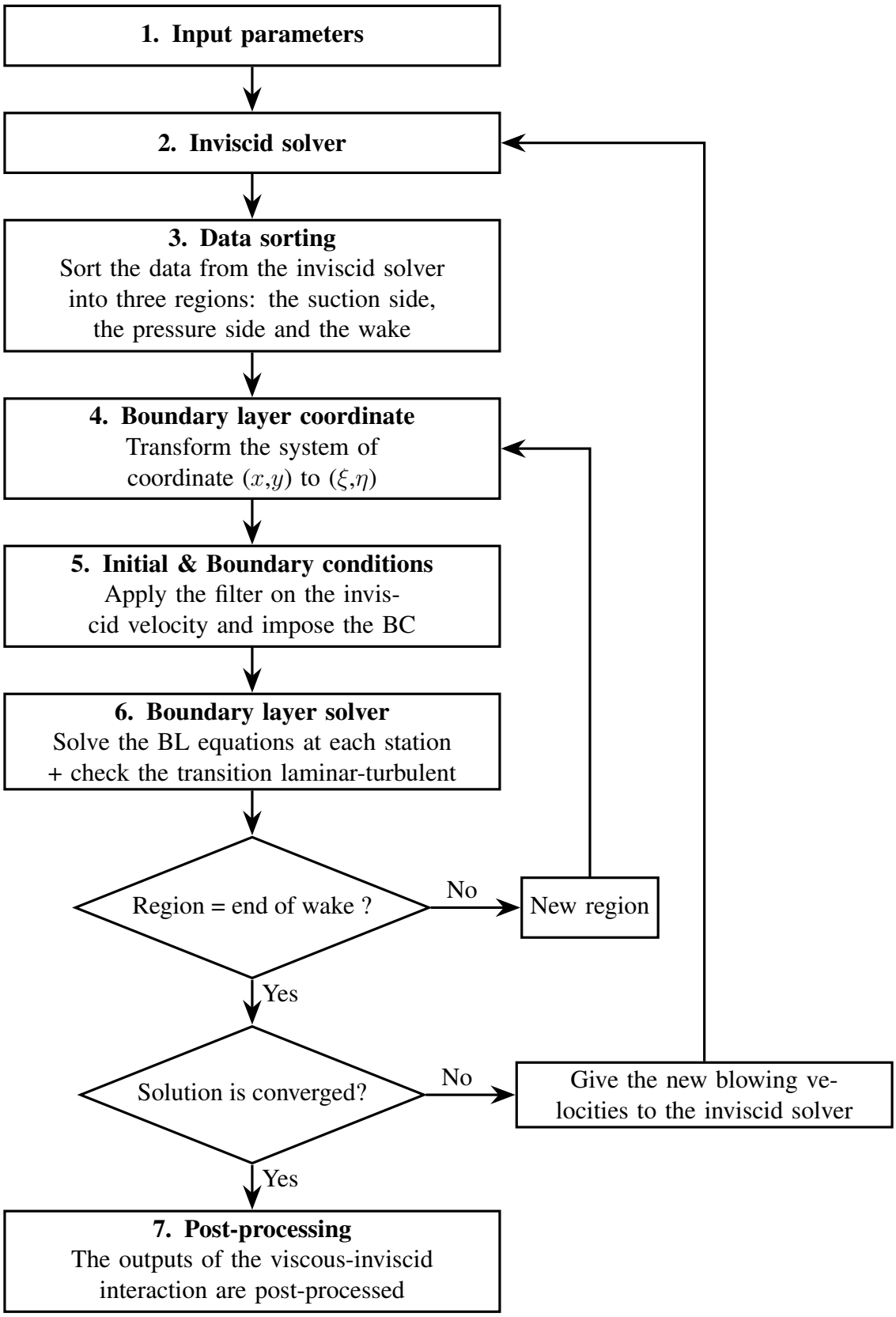

Figure 4.1.1: Solution procedure of the viscous-inviscid interaction.

4.2 Initialization

4.2.1 Input parameters

The computation needs a few input parameters given by the user to start. These input parameters are listed in Tab. 4.2.1 and are given for each simulation in Chapter 5.

User
Reynolds number Re [-]
Freestream Mach number M_∞ [-]
Angle of attack α [°]
Mesh size at the leading-edge [m]
Mesh size at the trailing-edge [m]
Mesh file

Table 4.2.1: Input parameters given by the user to the inviscid and viscous solvers.

4.2.2 Data sorting and coordinate transformation

When the simulation of the inviscid solver is over, its results need to be given to the viscous solver. Tab. 4.2.2 lists the parameters exchanged between the inviscid solver and the viscous solver during the interaction.

Inviscid -> Viscous
Position in x and y of the nodes for the airfoil and the wake
Value of u and v at the nodes for the airfoil and the wake
Value of M_e and ρ_e at the nodes for the airfoil and the wake
Numerotation of the nodes
Numerotation of the elements

Table 4.2.2: Data recovered by the viscous solver from the inviscid solver

where u is the velocity in the x-direction, v is the velocity in the y-direction, M_e is the Mach number at the edge of the boundary layer and ρ_e is the density at the edge of the boundary layer.
First of all, the data must be sorted in a given order once they are obtained from the inviscid solver. As a matter of fact, the latter works on unsorted data whilst the boundary layer computation needs to be performed by marching downstream. Therefore, the data must be sorted for the two physical boundaries: the airfoil and the wake, as illustrated in Fig. 4.2.1.

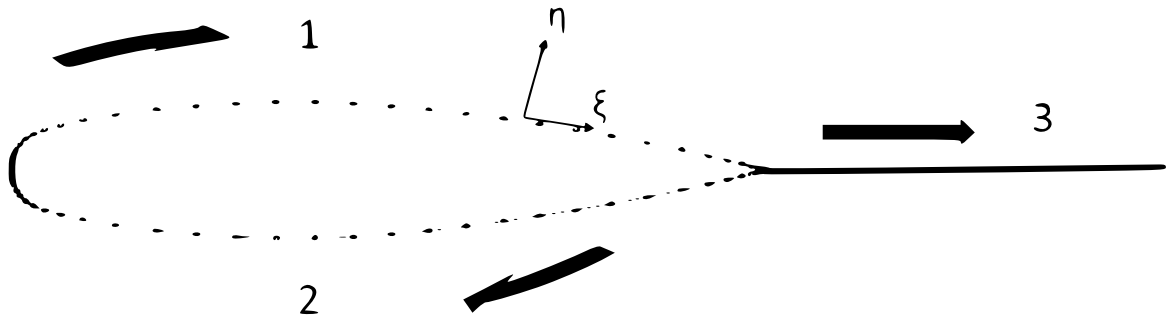

Figure 4.2.1: Sorting of the data for the viscous solver on the NACA 0012. The airfoil is sorted from region 1 (stagnation point to trailing-edge) to region 2 (trailing edge to stagnation point). The region 3 represents the wake.

After that, a transformation of coordinates is done such that only the streamwise coordinate ξ remains in the computation. The velocity at the edge of the boundary layer u_e is defined from u and v thanks to a rotation matrix. The rotation angle is the angle formed by the element and the x-axis.

4.2.3 Initial conditions

Since the computation is iterative, initial conditions are required. In this case, the initial conditions are the edge velocity u_e, the edge density ρ_e and the edge Mach number M_e distributions given by the inviscid solver. However, these values comes from an unstructured finite-element computation. Therefore, it is not defined at the nodes level but at the element level. To replace it at a node, an average of the values of the connected elements to this node is done. But, due to the unstructured mesh, the variation of the distributions along the streamwise coordinate present irregularities as seen in Fig. 4.2.2.

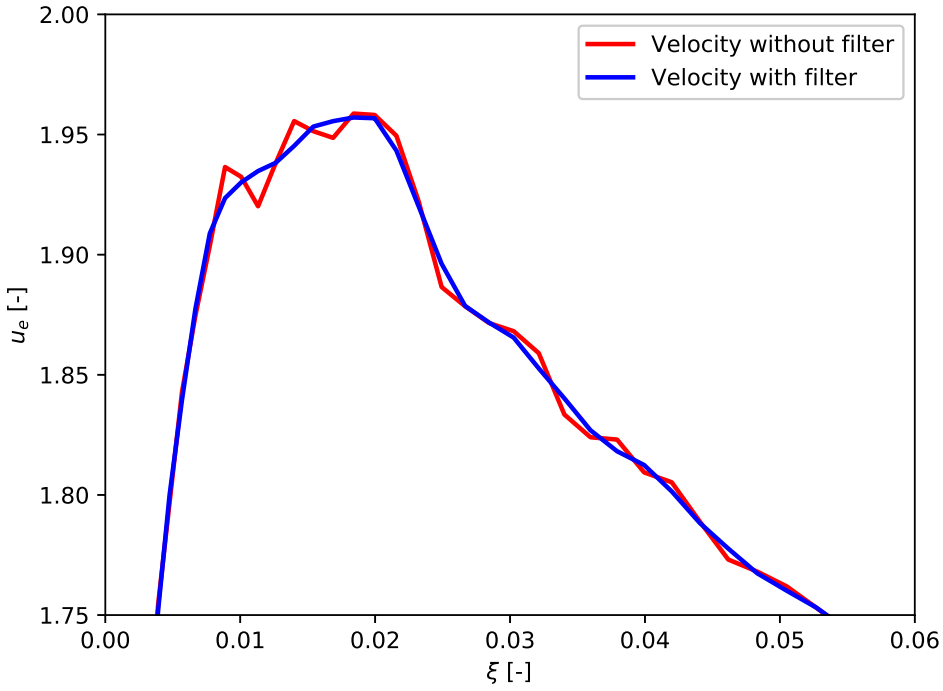

Figure 4.2.2: Illustration of the variation of the velocity along the chord on the suction side of the NACA 0012 airfoil from the inviscid solver at $Re = 10^7$, $\alpha = 5°$ and $M_\infty = 0.5$ with and without the application of a filter.

To avoid the irregularities, which can cause discontinuities and solution breakdown, an Savitzky-Golay filter has been implemented. Theoretical details can be found in Savitzky and Golay [53]. The purpose of the filter is to improve the smoothness of the data. In this approach, a polynomial of degree p fits each successive subset of $2m$+1 ($m < p/2$) points by the method of the least square. Then, an estimation of the smoothed signal can be given at the central point of each sub-set by a single set of convolution coefficient.

Therefore, the smoothed signal depends on:

- The degree of the polynomial which is usually two or three. If $p = 2$ the curvature is taken into account and if $p = 3$, the inflexion points are taken into account;
- The subset of point (the bandwidth) must be large enough to have an adequate smoothing but not to large to avoid killing the pressure peak and needed oscillations caused by the boundary layer equations in the case of this work.

The issue with the filter is that the inviscid velocity is smoothed at each iteration step since this velocity is averaged inside the inviscid solver. Hence, small ondulations induced by the boundary layer computation are damped, e.g the variation of velocity after the transition from laminar to turbulent flow as shown in Fig. 4.2.3. Finally, the solution crashes with this damping.

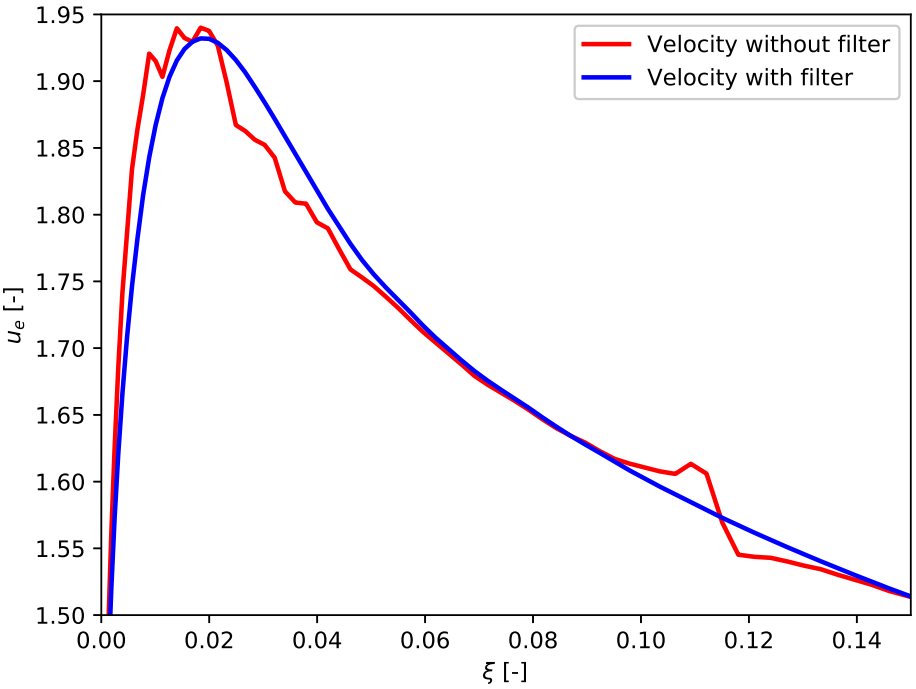

Figure 4.2.3: Illustration of the damping of the small oscillations from the boundary layer computation after the filtering of the velocity from the inviscid solver on the suction side of the NACA 0012 airfoil at $Re = 10^7$, $\alpha = 5°$ and $M_\infty = 0.5$.

Therefore, even if the curve in Fig. 4.2.3, with $p = 3$ & $m = 51$, is smoother than the curve in Fig. 4.2.2, with $p = 2$ & $m = 7$, the latter does not kill the small oscillations and the system converges to the good solution. Hence, compromises must be done between good accuracy and survivability of the simulation. Further investigations on different filtering parameters will be done in Chapter 5.

4.2.4 Boundary conditions

Finally, boundary conditions must be applied to the set of parabolic boundary layer equations. Hence, Dirichlet boundary conditions are imposed at the stagnation point ($\xi = 0$) for the laminar unknowns, at transition ($\xi = \xi_{tr}$) for the turbulent unknowns and the beginning of the wake. The conditions are derived from the Falkner-Skan family for the shape parameter H and from Thwaites for the momentum thickness θ, as proposed in Schlichting [26] and Moran [33]. At the transition, it is mandatory to impose a condition on the amplification rate ratio N and on the shear stress coefficient $C_\tau^{1/2}$. The first one defined the point of transition. The second one is needed to start the turbulent boundary layer computation. The boundary condition imposed here was derived by Drela [11]. As no useful empirical relation is formulated, the shear stress coefficient is assumed to be at 0.7 times its equilibrium value at transition. The boundary conditions imposed at the wake are derived from Cook and McDonald [54] and Drela [55]. Tab. 4.2.3 lists the boundary conditions.

Variables	**Stagnation point**	**Transition**	**Wake**
θ	$\sqrt{0.075 / \left(Re \frac{\mathrm{d}u_e}{\mathrm{d}\xi} \Big\vert_{\xi=0} \right)}$	/	$\theta_{\text{upper}} + \theta_{\text{lower}}$
H	2.23	/	$\frac{(H\theta)_{\text{upper}} + (H\theta)_{\text{lower}}}{\theta_{\text{upper}} + \theta_{\text{lower}}}$
u_e	0	/	$u_{e_{\text{inv}}}$
N	0	9	/
$C_\tau^{1/2}$	/	$0.7 C_{\tau EQ}^{1/2}$	$\frac{(C\tau\theta)_{\text{upper}} + (C_\tau\theta)_{\text{lower}}}{\theta_{\text{upper}} + \theta_{\text{lower}}}$

Table 4.2.3: List of the boundary conditions imposed at each new iteration.

Finally, the inflow at infinity is $u_\infty = 1$.

4.3 Boundary layer solver

4.3.1 Discretization scheme

The equations used for the laminar and turbulent flows are the momentum integral equation (Eq. 2.2.7), the kinetic shape parameter equation (Eq. 2.2.16) and the interaction law (Eq. 3.3.8). For the laminar part, the amplification ratio rate (Eq. 2.2.31) is added to model the transition. For turbulent flow, the shear-lag equation (Eq. 2.2.40) is added to take into account the Reynolds stresses. The four unknowns that are solved are the momentum thickness θ, the shape parameter H, the velocity at the edge of the boundary layer u_e and the amplification rate N in the case of a laminar flow or the square root of the shear stress coefficient $C_\tau^{1/2}$ in the case of a turbulent flow.

Since only the first derivative along the streamwise direction comes into play, the set of equations of the boundary layer is parabolic. Moreover, this set is characterized by first-order ordinary differential equations which are greatly non-linear and coupled. Hence, a space marching through each station of the boundary layer is performed. A finite-element method with an unstructured mesh is employed for the computation of the inviscid flow as seen in Chapter 2 and a finite-difference method is applied to the boundary layer equations. In the latter case, the mesh is not equally distributed and more points are added near the leading-edge of the airfoil as illustrated in Fig. 4.3.1. The computation is done for the airfoil and the wake.

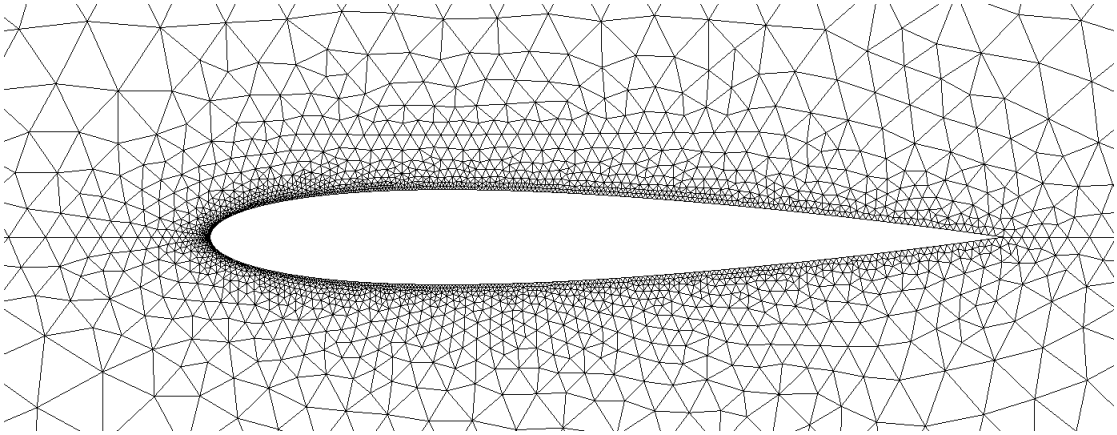

Figure 4.3.1: Illustration of the mesh on a NACA0012 airfoil for the inviscid and viscous flow.

The equations are discretized with a second order trapezoidal scheme since it has the smallest truncation error of the second-order A-stable scheme, as written in Hirsch [56]. However, upwinding has been added to the set of equations in order to improve the stability of the computation. As a matter of fact, the kinematic shape parameter equation (2.2.16) is relatively stiff at the transition. This is due to small quantity θ in the term $\theta\frac{\mathrm{d}H^*}{\mathrm{d}\xi}$. Since there is a rapid analytic change in H^* it leads to numerical difficulties to resolved it with the available mesh size. Therefore, instead of a central difference, a backward Euler scheme is applied. In practice, an upwind bias is added to the following variables,

$$\begin{aligned} \theta_a &= \epsilon\theta_i + (1-\epsilon)\,\theta_{i-1}, & C_{\tau_a} &= \epsilon C_{\tau_i} + (1-\epsilon)\,C_{\tau_{i-1}}, \\ H_a &= \epsilon H_i + (1-\epsilon)\,H_{i-1}, & M_{e_a} &= \epsilon M_{e_i} + (1-\epsilon)\,M_{e_{i-1}}, \\ u_{e_a} &= \epsilon u_{e_i} + (1-\epsilon)\,u_{e_{i-1}}, & Re_{\theta_a} &= \epsilon Re_{\theta_i} + (1-\epsilon)\,re_{\theta_{i-1}}, \end{aligned}$$

where $\epsilon = 0.5$ for the trapezoidal scheme and $\epsilon = 1$ for the backward Euler scheme. This bias is switched to one at the boundary condition to ensure stability at these stations and just before the onset of transition when the amplification rate ratio is greater than 8 to the end of the transition further downstream in the turbulent flow. Finally, the set of equations becomes

$$f_1 = \frac{\theta_i - \theta_{i-1}}{\xi_i - \xi_{i-1}} + \left(2 + H_a - Me_a^2\right)\frac{\theta_a}{u_{ea}}\frac{u_{ei} - u_{ei-1}}{\xi_i - \xi_{i-1}} - \frac{C_{f_a}}{2}, \tag{4.3.1a}$$

$$f_2 = \theta_a\frac{H_i^* - H_{i-1}^*}{\xi_i - \xi_{i-1}} + \left(2H_a^{**} + H_a^*(1 - H_a)\right)\frac{\theta_a}{u_{ea}}\frac{u_{ei} - u_{ei-1}}{\xi_i - \xi_{i-1}} - 2C_{Da} + H_a^*\frac{C_{f_a}}{2}, \tag{4.3.1b}$$

$$f_3 = u_{e_a} - \frac{4u_\infty\delta_a^*}{\pi(\xi_i - \xi_{i-1})} - (u_{e_a})_{old} + \frac{4u_\infty(\delta_a^*)_{old}}{\pi(\xi_i - \xi_{i-1})_{old}}, \tag{4.3.1c}$$

$$f_{4_{\textbf{lam}}} = \frac{N_i - N_{i-1}}{\xi_i - \xi_{i-1}} - A_a, \tag{4.3.1d}$$

$$\begin{aligned} f_{4_{\textbf{turb}}} = {} & 2\frac{\delta_a}{C_{\tau_a}^{1/2}}\frac{C_{\tau_i}^{1/2} - C_{\tau_{i-1}}^{1/2}}{\xi_i - \xi_{i-1}} - 5.6\left(C_{\tau EQ_a}^{1/2} - C_{\tau_a}^{1/2}\right) \\ & - 2\delta_a\left\{\frac{4}{3\delta_a^*}\left[\frac{C_{f_a}}{2} - \left(\frac{H_{k_a}}{6.7H_{k_a}}\right)^2\right] - \frac{1}{u_{e_a}}\frac{u_{ei} - u_{ei-1}}{\xi_i - \xi_{i-1}}\right\}, \end{aligned} \tag{4.3.1e}$$

where A_a is simply the right-hand side of Eq. 2.2.31 evaluated at the middle point of the element. The closure terms like the skin friction coefficient are computed at the mid-point location for the trapezoidal scheme and at the point i for the backward Euler scheme, i.e $C_{f_a} = F\left(H_{k_a}, M_{e_a}, Re_{\theta_a}\right)$.

4.3.2 Newton procedure

Since the integral boundary layer system (4.3.1) is non-linear, it must be resolved iteratively. Hence, a Taylor expansion around $\boldsymbol{U}$ gives

$$f(\boldsymbol{U}^{n+1}) = f(\boldsymbol{U}^n) + \frac{\partial f(\boldsymbol{U}^n)}{\partial \boldsymbol{U}^n}\Delta\boldsymbol{U} + \mathcal{O}\left((\Delta\boldsymbol{U})^2\right), \tag{4.3.2}$$

where n is the number of iteration and $\Delta\boldsymbol{U} = \boldsymbol{U}^{n+1} - \boldsymbol{U}^n$. The second order terms can be neglected and since $f(\boldsymbol{U}^{n+1}) = 0$,

$$\frac{\partial f(\boldsymbol{U}^n)}{\partial \boldsymbol{U}^n}\Delta\boldsymbol{U} = -f(\boldsymbol{U}^n), \tag{4.3.3}$$

where the right-hand side represents the residual vector which must be reduced as much as possible per iteration. Finally, the Jacobian matrix[1] is defined as

$$J(\boldsymbol{U}^n) = \frac{\partial f(\boldsymbol{U}^n)}{\partial \boldsymbol{U}^n} = \begin{pmatrix} \frac{\partial f_1}{\partial H_i} & \frac{\partial f_1}{\partial \theta_i} & \frac{\partial f_1}{\partial u_{e_i}} & \frac{\partial f_1}{\partial C_{\tau_i}^{1/2}} \\ \frac{\partial f_2}{\partial H_i} & \frac{\partial f_2}{\partial \theta_i} & \frac{\partial f_2}{\partial u_{e_i}} & \frac{\partial f_2}{\partial C_{\tau_i}^{1/2}} \\ \frac{\partial f_3}{\partial H_i} & \frac{\partial f_3}{\partial \theta_i} & \frac{\partial f_3}{\partial u_{e_i}} & \frac{\partial f_3}{\partial C_{\tau_i}^{1/2}} \\ \frac{\partial f_4}{\partial H_i} & \frac{\partial f_4}{\partial \theta_i} & \frac{\partial f_4}{\partial u_{e_i}} & \frac{\partial f_4}{\partial C_{\tau_i}^{1/2}} \end{pmatrix}. \tag{4.3.4}$$

This Jacobian is computed numerically thanks to a finite-difference method by introducing a small perturbation inside the system.

After the linearization, a linear solver can be applied to Eq. 4.3.3. In this work, the linear system is resolved thanks to LU decomposition with partial pivoting and row interchanges, as explained in Strang [57]. By written the system of equation in the form

$$\boldsymbol{A}\boldsymbol{x} = \boldsymbol{b}. \tag{4.3.5}$$

The LU decomposition gives

$$\boldsymbol{P}\boldsymbol{A} = \boldsymbol{L}\boldsymbol{U}, \tag{4.3.6}$$

[1] Here it is for the turbulent case

where $\boldsymbol{P}$ is the permutation matrix, $\boldsymbol{L}$ is the lower triangle matrix and $\boldsymbol{U}$ is the upper triangle matrix. Then, the solution is computed in two logical steps,

$$1) \quad \boldsymbol{Ly} = \boldsymbol{Pb}, \tag{4.3.7}$$

$$2) \quad \boldsymbol{Ux} = \boldsymbol{y}. \tag{4.3.8}$$

Since the matrix are triangular, they can be solved directly by forward and backward substitution.

To optimize the system, a line search algorithm has been combined to the Newton iteration. The purpose of the line search is to increase the robustness of the computation and to increase its convergence. A schematization of the line search is shown in Fig. 4.3.2.

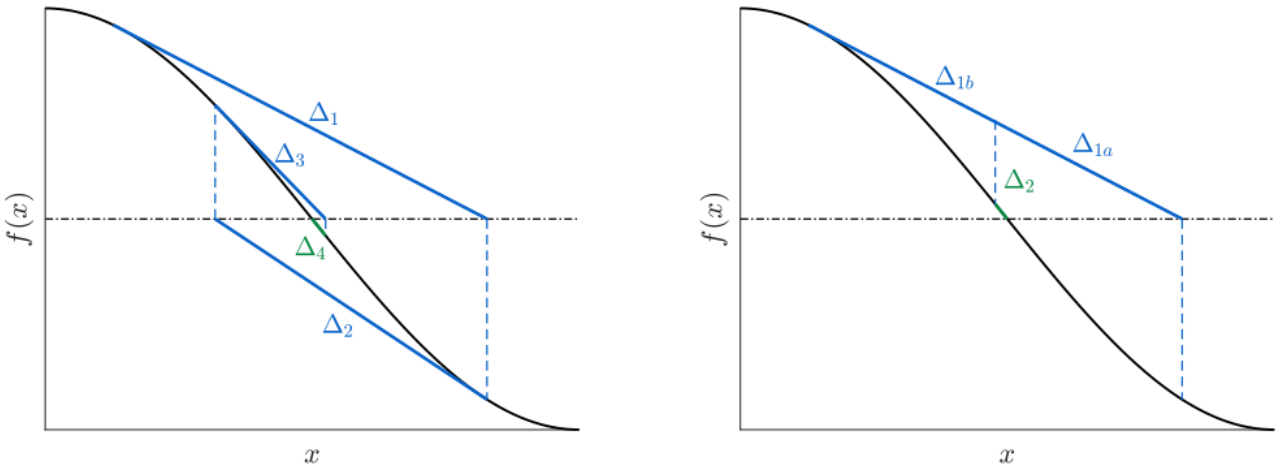

Figure 4.3.2: On the left: a basic Newton method; on the right: a Newton method combined with a line search. Taken from Crovato [4].

The line search used is a backtracking search line based on the Armijo–Goldstein condition, as written in Armijo [58]. The idea is to decrease the objective function $f(x)$ by shrinking the initial step size along a given search direction until the Armijo-Goldstein condition is fulfilled. This condition tests if the objective function at the new position has sufficiently decreased. The search direction $\boldsymbol{p}$ is assumed to be a descent direction to ensure that the objective function will decrease. Hence, the local slope of the function m is negative. The initial step size α_0 is assumed higher than zero and relatively large. The shrinking factor τ and a search control parameter c are defined between zero and one. Therefore, the

algorithm can be expressed as follows:

1) Start the iteration at $j = 0$;
2) Compute the objective function at the new position: $f(\boldsymbol{x} + \alpha_j \boldsymbol{p})$;
3) Check the Armijo-Goldstein condition: $f(\boldsymbol{x}) - f(\boldsymbol{x} + \alpha_j \boldsymbol{p}) \leq \alpha_j cm$;
4) If not fulfilled, increment j and set $\alpha_j = \tau \alpha_j$;
5) Repeat until condition is satisfied.

An usual value for c and τ is 0.5, as used by Armijo [58].

4.3.3 Transition

While each laminar station is computed with the laminar equations and each turbulent station is computed with the turbulent equations, it does not work during the transition. During this phase, the transition mostly occurs inside the element and not at a node. Hence, the flow in the element is both laminar and turbulent. Considering that the transition occurs between the $i^{th} - 1$ and the i^{th} points, the procedure is the following:

1) Laminar computation to point i;
2) $N_i > N_{\text{crit}}$ hence, transition occurs at $\xi_{tr} = \dfrac{(N_{\text{crit}} - N_{i-1})\,(\xi_i - \xi_{i-1})}{N_i - N_{i-1}} + \xi_{i-1}$;
3) Computation goes back to point $i - 1$;
4) Turbulent computation to point i;
5) Average the laminar and turbulent solutions for point i;

where $N_{\text{crit}} = 9$ in the present project. The average is performed with the percentage of the type of flow in the element,

$$w_{\text{lam}} = \frac{\xi_{tr} - \xi_{i-1}}{\xi_i - \xi_{i-1}}; \quad w_{\text{turb}} = \frac{\xi_i - \xi_{tr}}{\xi_i - \xi_{i-1}}. \tag{4.3.9}$$

And finally, the solutions at point i are

$$\theta_i = w_{\text{lam}}(\theta_i)_{\text{lam}} + w_{\text{turb}}(\theta_i)_{\text{turb}}; \quad H_i = w_{\text{lam}}(H_i)_{\text{lam}} + w_{\text{turb}}(H_i)_{\text{turb}}; \tag{4.3.10}$$

$$u_{e_i} = w_{\text{lam}}(u_{e_i})_{\text{lam}} + w_{\text{turb}}(u_{e_i})_{\text{turb}}; \quad C_{\tau_i} = w_{\text{turb}}(C_{\tau_i})_{\text{turb}}. \tag{4.3.11}$$

4.3.4 Wake

The wake is considered as one viscous layer. Then, the parameters computed at each wake station represent the total wake momentum and shape parameter. The flow in the wake is governed by the same set of equations (4.3.1) as for the airfoil. However, few modifications need to be done for the closure terms. Particularly for the equilibrium shear stress coefficient $C_{\tau EQ}$ which must be quadrupled from the boundary layer closure relation (Eq. 2.2.42), as defined by Green [16] from the data of Narasimha and Prabhu [59],

$$C_{\tau_{EQ}} = 4C_{\tau_{EQ}}\left(H^*, H_k, H, U_S\right). \tag{4.3.12}$$

Moreover, the skin friction coefficient is obviously set to zero in the wake. Thus, the inner layer contribution to the dissipation coefficient C_D (Eq. 2.2.38) vanishes while the outer layer term is doubled to consider the half-wake outer layer profile of the wake, as explained in Drela [55],

$$C_f = 0, \tag{4.3.13}$$

$$C_D = 2C_\tau\left(1 - U_S\right). \tag{4.3.14}$$

4.3.5 Stabilisation of the procedure

The integral formulation is relatively sensitive to perturbations. During the simulation, absurd transient values can occur and cause the computation to fail. In order to avoid this issue, some values have been bounded. The bounds have been defined either by trial and error or by further investigations of the work of Drela [32]. They are practical engineering solutions.

The first parameter to be bound is the momentum thickness Reynolds number Re_θ. For laminar flows, Re_θ cannot go below zero since it would be physically incorrect. For turbulent flows, Re_θ cannot be lower than 200. This limit avoids having too low values after the transition. The second parameter to be bound is the kinematic shape parameter H_k which is equal to the shape parameter H for incompressible flows. H_k must always be greater than one. Otherwise, the flow could be considered as a jet, which is not the case in the present work. Therefore, $H_k > 1.02$ for an airfoil and $H_k > 1.00005$ for the wake.

Then, the shear stress coefficient C_τ is also bounded at the transition. To avoid absurd transient values, $C_\tau > 0.03$ for the airfoil and $C_\tau > 0.05$ for the wake since the production of shear stress is higher in the latter. The last two bounded parameters are the thickness of the boundary layer δ which must be lower or equal to 12θ to avoid too large boundary layer and the slip velocity U_S which must be lower than one to avoid negative value inside Eq. 2.2.42. As a matter of fact, this is the square root of Eq. 2.2.42 that is used in the simulation.

4.4 Convergence

Fig. 4.1.1 summarizes the solution procedure for the viscous-inviscid interaction implemented in this work. In this procedure, three loops appear. The first one is hidden in the boundary layer solver, it is the loop over all the stations of one region. The second one is the loop over all the regions and the last one is the loop until the convergence is reached. While the first two loops have a physical end, the last one does not. Hence, a convergence criterion needs to be defined.

The convergence criterion for the boundary layer iteration is based on the drag coefficient c_d. A global parameter was chosen in order to overcome the fluctuations caused by the irregularities of the inviscid initial conditions. If a local parameter such as the skin friction coefficient was chosen to be the convergence criterion, these irregularities would make the solution impossible to converge with a good accuracy.

The drag coefficient is computed by applying the expression derived by Squire and Young [60] at the last point of the wake:

$$c_d = \left(2\theta \left(\frac{u_e}{u_\infty} \right)^{\frac{H+5}{2}} \right)_{\text{end of wake}} \tag{4.4.1}$$

The previous formula extrapolates the momentum thickness to downstream infinity and therefore, an asymptotic behaviour downstream of the point of application is assumed for the wake. This assumption is reasonable for the simulation in this work since the last point of the wake is considered far away from the trailing edge. Therefore, the convergence monitor is expressed as:

$$\epsilon = \frac{\left| c_d^n - c_d^{n-1} \right|}{c_d^n} < \epsilon_{\text{crit}} \tag{4.4.2}$$

where n is the iteration number and ϵ_{crit} is the value of the tolerance. When the given tolerance is reached, the computation ends and the final values of the boundary layer variables per station are written to files. Finally, these files are used to visualize the results as shown in Chapter 5.

Chapter 5

Application to 2D steady flow

In this chapter, the results of three test cases are presented. The first case is a simulation of an attached flow around the well-studied NACA 0012 airfoil. The case is performed by considering both an incompressible and a compressible flow. The second case is a simulation of a separated flow around the same airfoil. In this case, the flow is considered incompressible to avoid the apparition of transonic features at a high angle of attack. Finally, a simulation of a highly compressible flow around the RAE 2822 airfoil is performed. In this case, the angle of attack is small to study only the compressibility effects.
In this chapter, the attached flow case is used to validate the model and its implementation. The two other cases are used to understand the limits of the current implementation, to identify the possible issues and to propose solutions for a future work. The validation of the results is done thanks to the software *Xfoil* [61] based on the work of Drela [32]. An inviscid linear-vorticity panel method with a Karman-Tsien compressiblity correction is fully coupled with the two-equations integral dissipation method for the viscous solver.
However, for compressible cases, there are discrepancies in the pressure coefficients distribution along the airfoil between the inviscid solver of *Flow* and the inviscid solver of *Xfoil*. Due to this difference, the validation of the viscous solver could not be done entirely for the compressible regime. There will always be a source of error.
In order to determine the origin of this source of error, the inviscid solver of *Flow* and of *Xfoil* will be compared to a higher order simulation solving the Euler equations: *SU2* [62] [63] [64]. The latter is an open-source code for multiphysics simulations using a *finite-volume* method with an Euler implicit scheme to discretize the equations. A time marching procedure is applied to reach steady state. The comparison will show if the results of *Flow* are reliable or not. Moreover, for the last test case, *SU2* will be used to perform a RANS simulation based on the Spalart-Allmaras [65] turbulence model and a

Bas-Cakmakcioglu [66] algebraic transition model.
For all cases, the input parameters and a comparison of the initial velocity u_e between the inviscid simulations of *Xfoil* and *Flow* are presented. The boundary layer parameters shown in the following section are the shape parameter H, the skin friction C_f and the displacement thickness δ^*.

5.1 Mesh and filter convergence analyses

Before starting the simulations, convergence analyses are carried out to prove the relevance of the results in the case studies. First, a convergence analysis is performed on the mesh by varying the mesh size at the leading edge n_{LE} and at the trailing edge n_{TE}. Then, the impact of the filtering parameters are studied on the chosen mesh. These parameters are the bandwidth m and the polynomial order p. The convergence criteria are the lift coefficient c_l and the drag coefficient c_d. The mesh convergence analysis is performed with the best filtering parameters.

5.1.1 Attached flow around a NACA 0012

For the attached flow case around the NACA 0012 at a Reynolds number $Re = 10^7$ and an angle of attack $\alpha = 5°$, two flows are considered: an incompressible one and a compressible one at a Mach number $M = 0.5$. The mesh analysis is done with $m = 0$ and $p = 0$ for the incompressible case and $m = 7$ and $p = 2$ for the compressible case. The filter analysis is done with $n_{LE} = 0.001$ and $n_{TE} = 0.01$ for both cases.
Tab. 5.1.1 & Tab. 5.1.2 list the solutions of respectively the mesh and the filter convergence analyses for the attached incompressible flow case,

$n_{LE} \times n_{TE}$	c_l	c_d
0.01×0.01	0.5770	0.00588
0.001×0.01	0.5819	0.00620
0.001×0.005	0.5832	0.00627

Table 5.1.1: Mesh convergence of the incompressible attached flow around the NACA 0012

$m \times p$	c_l	c_d
0×0	0.5819	0.00621
7×2	0.5819	0.00620
11×2	0.5819	0.00606

Table 5.1.2: Filter convergence of the incompressible attached flow around the NACA 0012

Tab. 5.1.3 & Tab. 5.1.4 list the solutions of respectively the mesh and the filter convergence analyses for the attached compressible flow case,

$n_{LE} \times n_{TE}$	c_l	c_d
0.005×0.005	0.6882	0.00639
0.001×0.01	0.6948	0.00678
0.001×0.005	0.6954	0.00680

Table 5.1.3: Mesh convergence of the compressible flow around the RAE 2822

$m \times p$	c_l	c_d
5×2	0.6945	0.00678
7×2	0.6948	0.00671
11×3	/	/

Table 5.1.4: Filter convergence of the compressible flow around the RAE 2822

The second mesh size provides a good convergence for both cases. The lift coefficient is converged below two lift counts and the drag coefficient is converged below one drag count. The filter convergence analysis of the incompressible flow shows a good convergence for the two first cases, the simulation starts to diverge when the filtering parameters are increased. The filter convergence analysis of the compressible case shows that only the two first sets of parameters give a solution to the simulation. Therefore, the second mesh and the set of $p = 2$ and $m = 7$ filtering parameters are keeping for both flows for the rest of the case study.

5.1.2 Incompressible separated flow around a NACA 0012

The second analyses are performed on a separated incompressible flow around the NACA 0012 at a Reynolds number $Re = 10^7$ and an angle of attack $\alpha = 12°$. The mesh analysis is done with $m = 11$ and $p = 2$. The filter analysis is done with $n_{LE} = 0.00075$ and $n_{TE} = 0.01$. Tab. 5.1.5 & Tab. 5.1.6 list the solutions of respectively the mesh and the filter convergence analyses,

$n_{LE} \times n_{TE}$	c_l	c_d
0.005×0.05	1.3844	0.00434
0.001×0.01	1.3913	0.00952
0.00075×0.01	1.3930	0.01072
0.0005×0.01	1.3930	0.01110

Table 5.1.5: Mesh convergence of the incompressible separated flow around the NACA 0012

$m \times p$	$c_l[-]$	$c_d[-]$
7×2	1.3929	0.01045
11×2	1.3930	0.01072
13×2	1.3910	0.00971

Table 5.1.6: Filter convergence of the incompressible separated flow around the NACA 0012

In this case, the lift coefficient is well converged but the drag coefficient still varies. The variation in the drag coefficient is mainly due to a presence of a singularity at the point of separation as shown in Sec. 5.3. However, the difference between the third and fourth meshes is lower than four drag counts

and it is acceptable. The lift and the drag coefficients start to diverge when the filtering parameters are increased. Therefore, the third mesh size and the second set of filtering parameters are chosen for the second case study.

5.1.3 Highly compressible flow around a RAE2822

The third analyses are performed on a compressible flow around the RAE 2822 at a Reynolds number $Re = 6.5 \times 10^6$ and an angle of attack $\alpha = 0.5°$. The mesh analysis is done with $m = 21$ and $p = 2$. The filter analysis is done with $n_{LE} = 0.001$ and $n_{TE} = 0.005$. Tab. 5.1.7 & Tab. 5.1.8 list the solutions of respectively the mesh and the filter convergence analyses,

$n_{LE} \times n_{TE}$	c_l	c_d
0.005×0.01	0.4314	0.00387
0.001×0.01	0.4467	0.00391
0.001×0.005	0.4542	0.00392
0.001×0.001	0.4551	0.00392

Table 5.1.7: Mesh convergence of the compressible flow around the RAE 2822

$m \times p$	c_l	c_d
11×2	0.4551	0.00393
21×2	0.4542	0.00392
31×2	0.4530	0.00390

Table 5.1.8: Filter convergence of the compressible attached flow around the RAE 2822

The lift and the drag coefficients are converged respectively below one lift and one drag count. The increase of the filtering parameters shows again a divergence in the results. Therefore, the third mesh size and the second set of the filtering parameters are chosen for this test case.

5.2 Case 1: Attached flow around a NACA 0012 airfoil

To simulate an attached flow around the airfoil, an angle of attack $\alpha = 5°$, a Mach number $M_\infty = 0$ for the incompressible case and $M_\infty = 0.5$ for the compressible case are chosen. The angle of attack allows to compute quite high velocity gradients after the stagnation point without dealing with separated flow. The Mach number allows to have interesting compressibility effects without going to the transonic regime.

5.2.1 Input parameters

Input parameter	Values
Reynolds number	10^7
Mach number (only for compressible case)	0.5
Angle of attack	5°
Mesh size at the leading-edge	0.001 [m]
Mesh size at the trailing-edge	0.01 [m]
Polynomial order of the filter p	2
Bandwidth m	7

Table 5.2.1: Input parameters for the incompressible and compressible tests for the simulation of an attached flow around the NACA 0012.

A ratio of $1/10$ was chosen between the mesh size at the trailing edge and the mesh size at the leading edge. It allows to catch the high velocity gradient right after the stagnation point. Fig. 5.2.1 illustrates the mesh around the airfoil for the following simulation. The inviscid region is discretized by two-dimensional triangles which become one-dimensional elements in the viscous region.

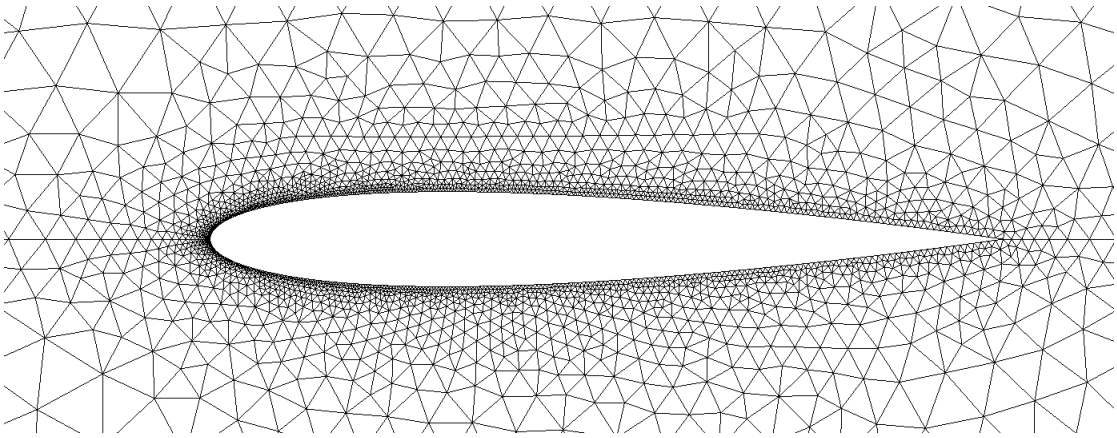

Figure 5.2.1: Representation of the geometry of the NACA 0012 and the mesh used for the first test case.

Fig. 5.2.2 shows the filtered initial velocity distributions for both the incompressible case (Fig. 5.2.2a) and the compressible case (Fig. 5.2.2b). As observed, the velocity peaks of *Flow* never reach the velocity peaks of *Xfoil* for the given configuration. A deeper investigation near the leading edge on the suction side shows the apparition of irregularities for the compressible velocity distribution as seen in Fig. 5.2.2d. It is not done on the pressure side since both velocity distributions are totally equivalent.

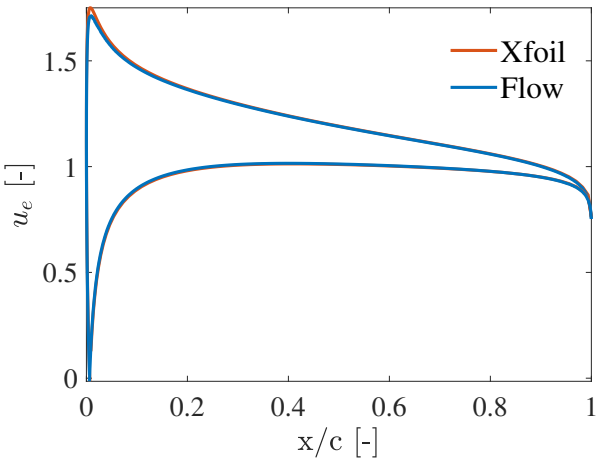

(a) Incompressible flow

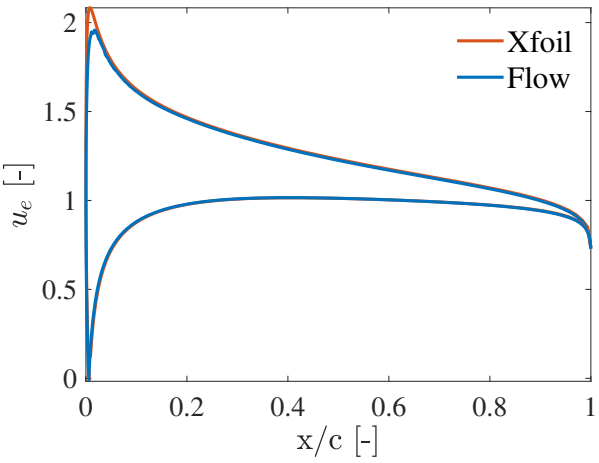

(b) Compressible flow at $M_\infty = 0.5$

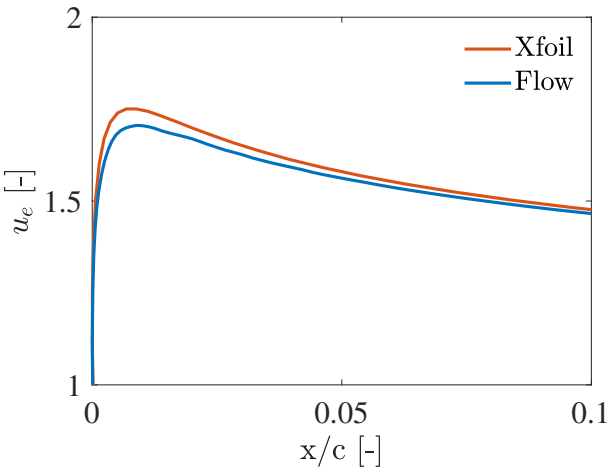

(c) Incompressible flow at leading edge

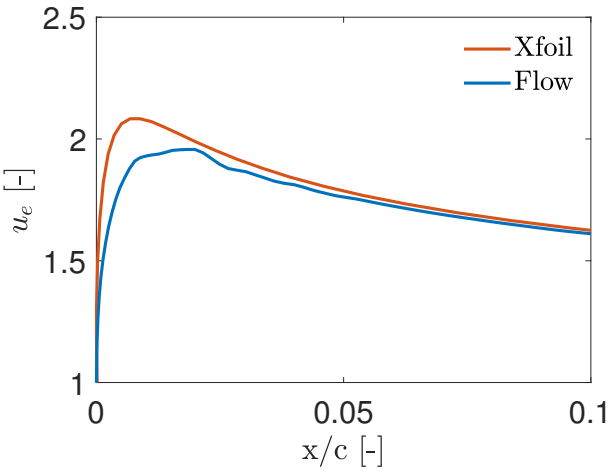

(d) Compressible flow at the leading edge at $M_\infty = 0.5$

Figure 5.2.2: Comparison between the inviscid velocity of *Xfoil* and *Flow* along the chord of the NACA 0012 at $Re = 10^7$ and $\alpha = 5°$.

5.2.2 Results

The first boundary layer parameter presented is the shape parameter H. The latter is interesting due to its stiffness during transition. It changes rapidly and the set of equations has to catch the variation without a refined mesh at the transition. Fig. 5.2.3 & Fig. 5.2.4 illustrate the variation of the shape parameter for both incompressible and compressible cases along the chord on the suction side and the pressure side. Along all the airfoil, the shape parameter of *Flow* matches almost perfectly with the one of *Xfoil* for both cases. The dramatic drop of the shape parameter at the transition is well caught by the numerical

simulation.

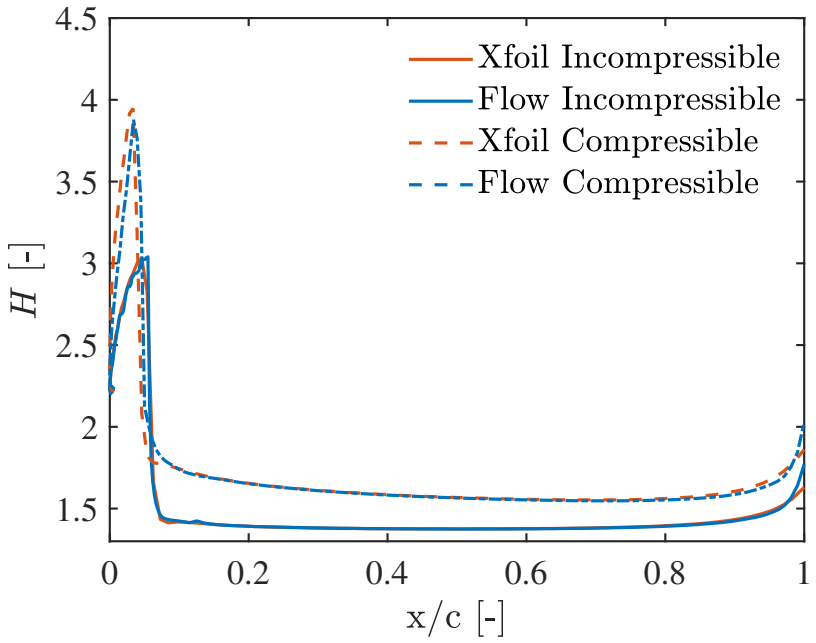

Figure 5.2.3: Variation of the shape parameter H on the suction side of the NACA 0012 at $Re = 10^7$, $\alpha = 5°$, $M_\infty = 0$ (solid lines) and $M_\infty = 0.5$ (dash-dot lines).

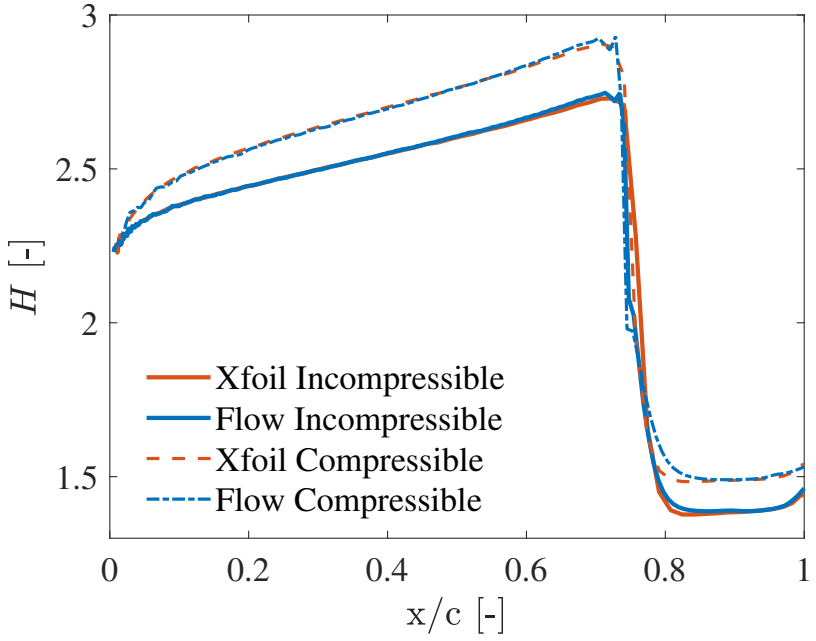

Figure 5.2.4: Variation of the shape parameter H on the pressure side of the NACA 0012 at $Re = 10^7$, $\alpha = 5°$, $M_\infty = 0$ (solid lines) and $M_\infty = 0.5$ (dash-dot lines).

The second boundary layer parameter presented is the skin friction coefficient C_f. This parameter is interesting due to its highly sensitivity to the other variables. Moreover, the skin friction coefficient can directly show the flow separation. Fig. 5.2.5 illustrates the variation of this parameter on the suction of the airfoil for both incompressible and compressible cases.

Again, for the incompressible case, the skin friction coefficient computed by *Flow* matches almost perfectly the one computed by *Xfoil*. For the compressible case, a higher peak is predicted by *Flow*. This difference continue further downstream. It can be explained by the presence of irregularities in the initial velocity distribution as seen in Fig. 5.2.2d. As a matter of fact, these irregularities are also presented in the initial Mach number distribution since the latter is a function of the velocity. As reminder, the skin friction coefficient is directly a function of the edge Mach number (see Eq. 2.2.34). Hence, if there is discrepancies between the initial conditions computed by the two inviscid solvers, there will be discrepancies between the skin friction coefficients computed by the two viscous solvers.

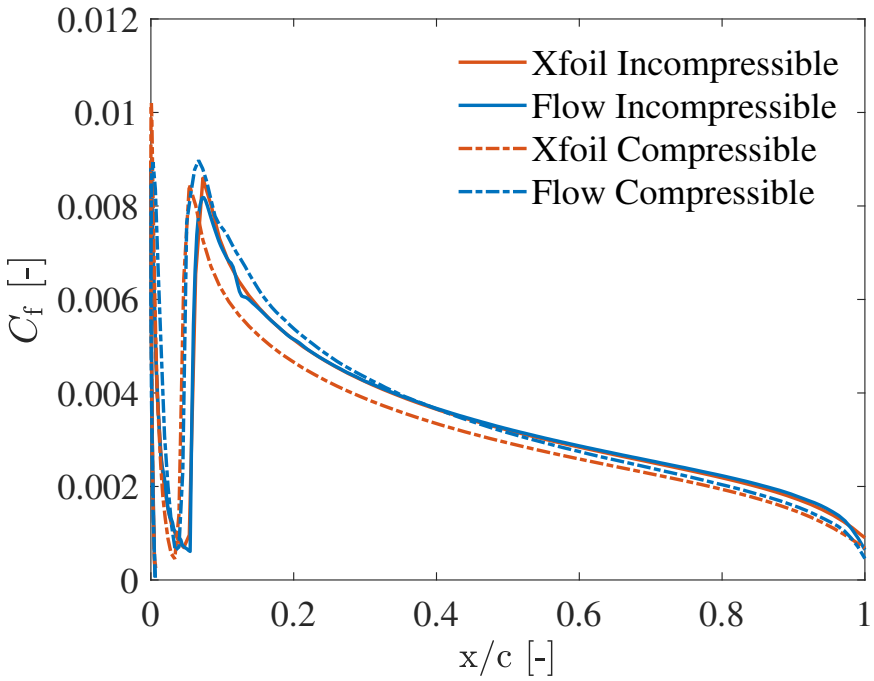

Figure 5.2.5: Variation of the skin friction coefficient C_f on the suction side of the NACA 0012 at $Re = 10^7$, $\alpha = 5°$, $M_\infty = 0$ (solid lines) and $M_\infty = 0.5$ (dash-dot lines).

On the pressure side, the first peak of the skin friction coefficient is better caught than the second one for both the incompressible and compressible cases as seen in Fig. 5.2.6. The issue represented here is the smoothing of the velocity distribution by the application of the filter as illustrated in Fig.4.2.3. Since the second peak occurs in a zone of lower velocity gradient and less dense grid points, the variation of the

velocity induced by the laminar to turbulent transition is more impacted by the smoothing procedure.

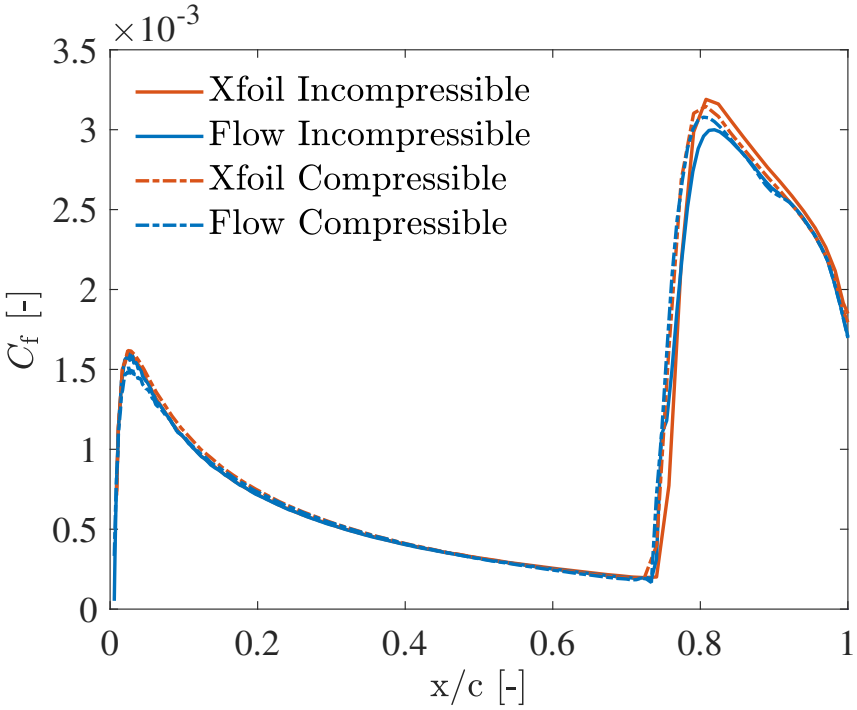

Figure 5.2.6: Variation of the skin friction coefficient C_f on the pressure side of the NACA 0012 at $Re = 10^7$, $\alpha = 5°$, $M_\infty = 0$ (solid lines) and $M_\infty = 0.5$ (dash-dot lines).

The third boundary layer parameter presented is the displacement thickness δ^*. It is a good summary of the boundary layer behaviour. Contrary to the skin friction coefficient, this parameter is not too sensitive to other variables. As a reminder, the displacement thickness is equal to the shape parameter H times the momentum thickness θ. While the first term is sensitive to the initial values, the second one is not. Moreover, the momentum thickness θ is a small quantity in front of the shape parameter H hence, it absorbs most of the perturbations.

Fig. 5.2.7 shows the variation of the displacement thickness on the suction side of the airfoil. The displacement thickness increases rapidly since the transition occurs almost at the leading-edge. The values computed by *Flow* match almost perfectly the values computed by *Xfoil* for both the incompressible and compressible cases except close to the trailing edge. *Flow* calculates a higher displacement thickness at this location. This is due to a different implementation of the Kutta condition.

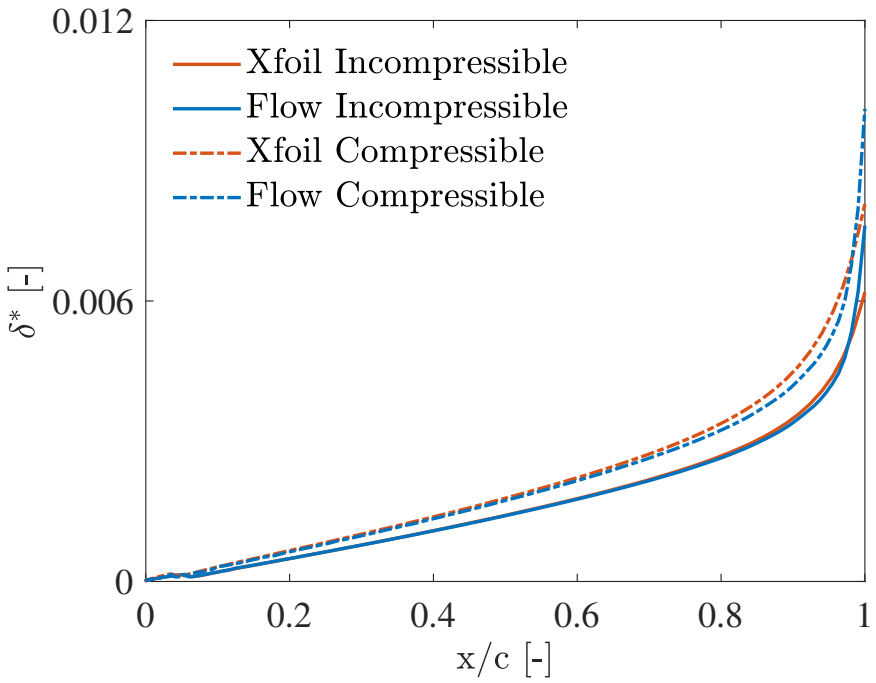

Figure 5.2.7: Variation of the displacement thickness δ^* on the suction side of the NACA 0012 at $Re = 10^7$, $\alpha = 5°$, $M_\infty = 0$ (solid lines) and $M_\infty = 0.5$ (dash-dot lines).

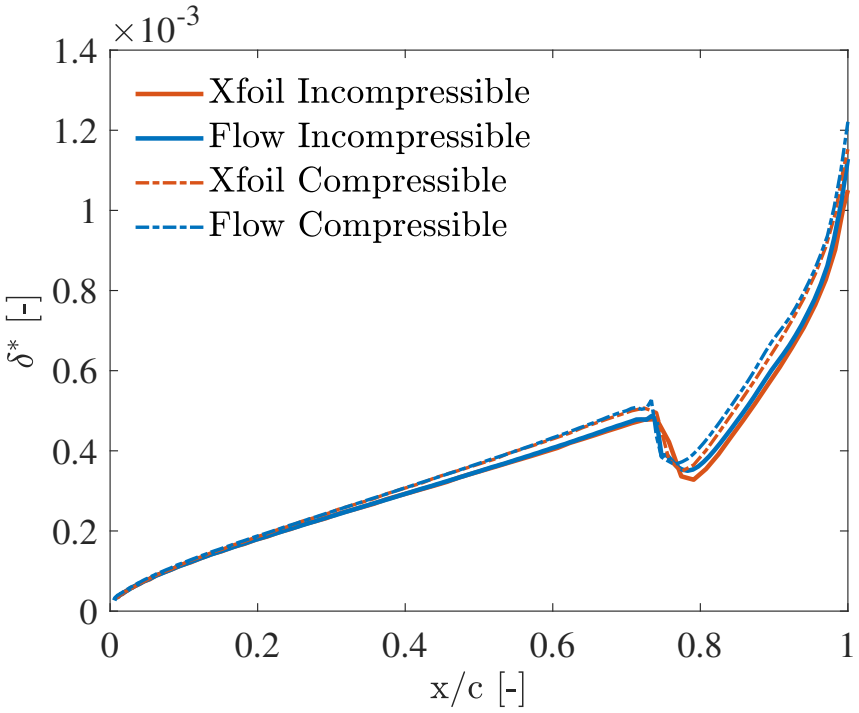

Figure 5.2.8: Variation of the displacement thickness δ^* on the pressure side of the NACA 0012 at $Re = 10^7$, $\alpha = 5°$, $M_\infty = 0$ (solid lines) and $M_\infty = 0.5$ (dash-dot lines).

On the pressure side, the increase of the displacement thickness δ^* is not so high since most of the flow is laminar along the airfoil as seen in Fig. 5.2.8. Hence, the drop of the displacement thickness due to the drop of the shape parameter H at the transition is easier to visualize. After the drop, the parameter increases rapidly due to the rapid increase of the momentum thickness θ in a turbulent flow. The values computed by *Flow* match again the values computed by *Xfoil* at almost any location for both the incompressible and compressible cases.

A comparison between the variation of the pressure coefficients along the airfoil from *Flow* and *Xfoil* is done in Fig. 5.2.9 for the incompressible case and in Fig. 5.2.10 for the compressible case. The inviscid pressure coefficients are added to the plots to show the impact of the boundary layer on the pressure distribution.
There is not much difference between the two inviscid solvers for the incompressible case, *Xfoil* and *Flow* predict almost the same suction peak, as seen in Fig. 5.2.9. Therefore, the comparison of the two viscous solvers shows a good correspondence between the distribution of pressure coefficients along the NACA 0012. Both predict quite the same reduction of the suction peak and a lower pressure coefficient at the trailing edge due to the viscous effects. Moreover, the transition locations are illustrated by the small variations of the pressure for the viscous solvers.

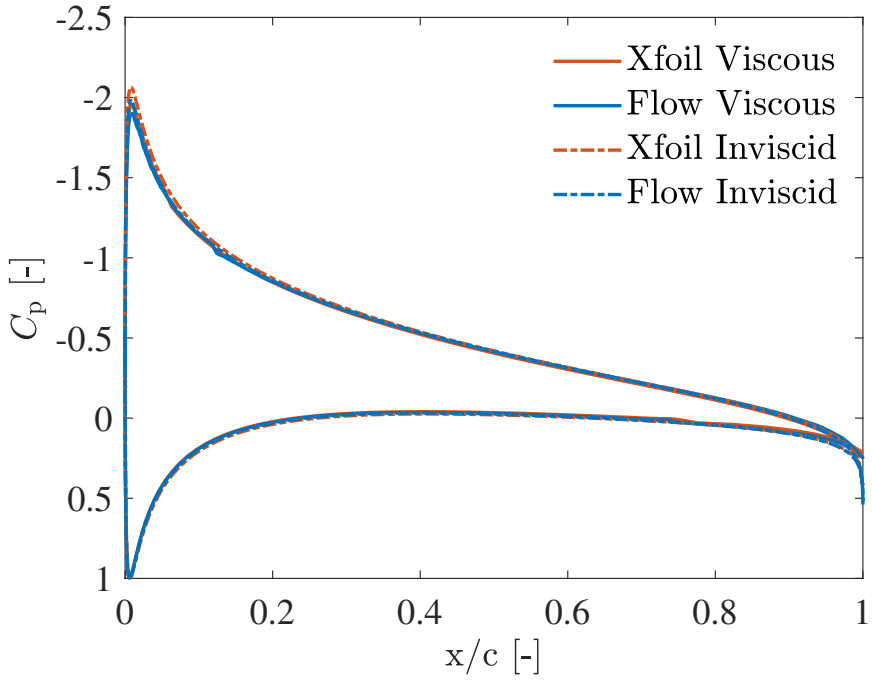

Figure 5.2.9: Pressure coefficients C_p distributions along the NACA 0012 in the case of an incompressible flow at $Re = 10^7$ and $\alpha = 5°$.

In Fig. 5.2.10, there is a large difference in the minimum pressure coefficient between *Flow* and *Xfoil*. Then, the results are compared with the higher fidelity solver *SU2* [1]. The latter shows that *Flow* predicts the correct minimum pressure coefficient contrary to *Xfoil* which tends to overestimate this peak. Then, the results of *Flow* are more reliable than *Xfoil* at that location. As previously, oscillations due to the initial velocity and Mach number distributions appear on the suction side of the airfoil in the viscous simulation of *Flow*.

Therefore, two sources of error can be defined in the simulation proposed by the two viscous solvers for the attached compressible case. The first one comes from the overestimation of the minimum pressure coefficient of *Xfoil*. The second one is due to the oscillations caused by the irregularities in the initial conditions in *Flow*.

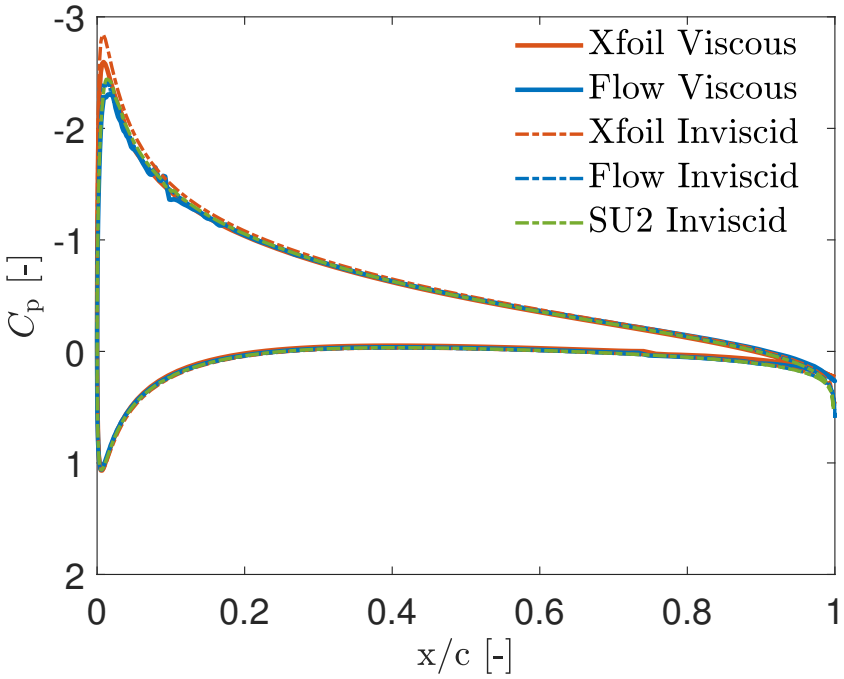

Figure 5.2.10: Pressure coefficients C_p distribution along the NACA 0012 in the case of a compressible flow at $M_\infty = 0.5$, $Re = 10^7$ and $\alpha = 5°$.

[1] The mesh convergence analysis is done in Appendix A.1.

5.2.3 Discussion

Tab. 5.2.2 shows the minimum pressure $C_{\mathrm{p_{min}}}$, the lift c_l and drag coefficients c_d as well as the locations of the transition as a percentage of the cord x/c on the NACA 0012 airfoil at $Re = 10^7$, $\alpha = 5°$, $M_\infty = 0$ for the incompressible flow and $M_\infty = 0.5$ for the compressible flow.

		$C_{\mathrm{p_{min}}}$	c_l	c_d	x_{tr}^{top}	x_{tr}^{bot}
Incompressible case	*Xfoil*	-1.953	0.56	0.0061	0.0531	0.7484
	Flow	-1.902	0.58	0.0062	0.0555	0.7397
Compressible case	*Xfoil*	-2.595	0.68	0.0067	0.0374	0.7391
	Flow	-2.305	0.69	0.0067	0.0384	0.7364

Table 5.2.2: Comparison of the aerodynamic loads and the locations of the transition between *Xfoil* and *Flow* for the NACA 0012 at $Re = 10^7$, $\alpha = 5°$.

These results prove that the theoretical model defined in this project and its numerical implementation work well for engineering applications such as the simulation of an attached flow around an airfoil. Each transition location is determined within an error of less than 0.5% of the chord. Even if the lift coefficient of *Flow* tends to be slightly higher than the one predicts by *Xfoil*, there is a good agreement between the aerodynamic loads computed with *Flow* and *Xfoil*. The discrepancies between the minimum pressure coefficient calculated by the two viscous solvers come from the difference in the inviscid solvers.

In summary, the viscous-inviscid interaction implemented in the present work is able to simulate with a good accuracy an attached flow around an airfoil. The flow can be either incompressible or compressible. For the latter case, sources of error from the inviscid solver must be taken into account such as the irregularities in the initial velocity and Mach number distributions due to the transformation of a finite-element simulation to a finite-difference simulation and the difference between the minimum pressure coefficient predicted by the two inviscid solvers.

5.3 Case 2: Separated flow around a NACA 0012 airfoil

To study the behaviour of *Flow* in the case of a separated flow, an angle of attack $\alpha = 12°$ is chosen and an incompressible flow is considered. As seen previously, more sources of error must be taken into account in the case of a compressible flow. Moreover, there is a risk of a transonic flow regime with such

a high angle of attack. This test case represents the NACA 0012 near stall condition ($\sim \alpha = 15°$) hence, a large portion of the flow along the airfoil is separated.

5.3.1 Input parameters

All the input parameters are listed in Tab. 5.3.1. A higher mesh size ratio than for the attached case is used between the leading edge and the trailing edge. The aim is to catch the high pressure peak and the high velocity gradients at the leading edge with accuracy. A higher bandwidth $m = 11$ is prescribed to improve the smoothness of the initial conditions.

Input parameter	**Values**
Reynolds number	10^7
Mach number	0
Angle of attack	12°
Mesh size at the leading-edge	0.00075 [m]
Mesh size at the trailing-edge	0.01 [m]
Mesh file	NACA 0012
Polynomial order of the filter p	2
Bandwidth m	11

Table 5.3.1: Input parameters for the simulation of a separated flow around the NACA 0012.

Fig. 5.3.1 illustrates the geometry of the airfoil and the mesh used for this simulation.

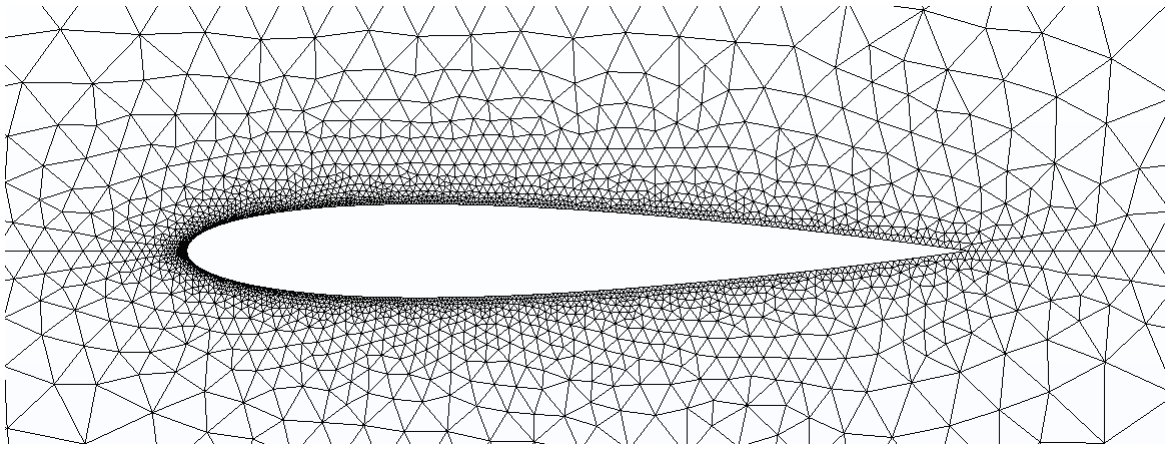

Figure 5.3.1: Representation of the geometry of the NACA 0012 and the mesh used for the second test case.

Fig. 5.3.2 shows the comparison between the filtered initial inviscid velocity distribution of *Flow* and the initial inviscid velocity distribution of *Xfoil*. There is almost a perfect match on the suction side (Fig. 5.3.2a) and the lower side (Fig. 5.3.2b). Therefore, no source of error is caused by the inviscid solver of *Flow*.

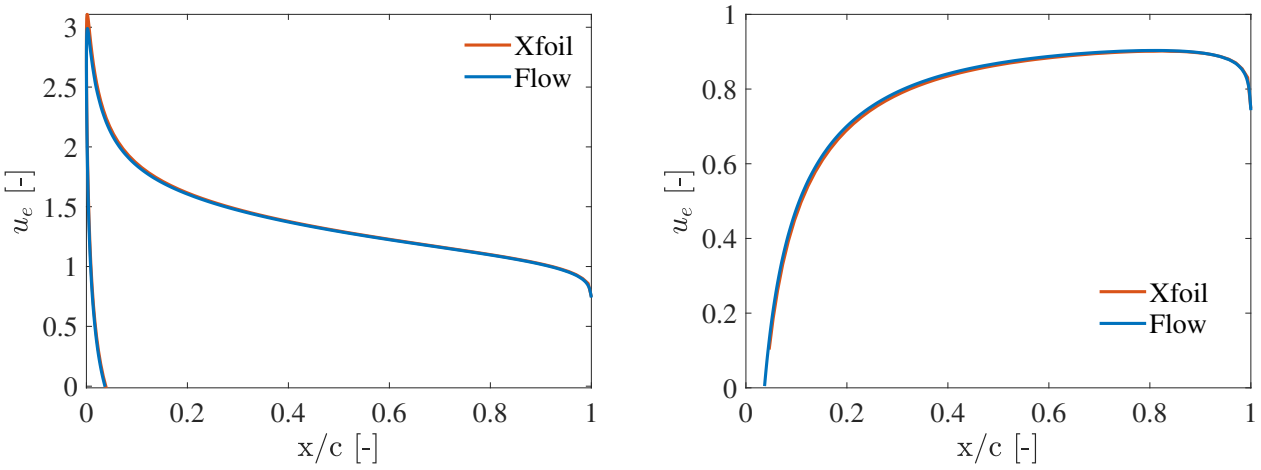

(a) Suction side

(b) Pressure side

Figure 5.3.2: Comparison between the inviscid velocity of *Xfoil* and *Flow* along the NACA 0012 at $Re = 10^7$ and $\alpha = 12°$.

5.3.2 Results

Fig. 5.3.3 shows the variation of the shape parameter H on the suction side of the airfoil. The first observation is the difference between the maximum shape parameter computed by *Flow* and *Xfoil*. The first one is not shown in Fig. 5.3.3 since it goes to more than twenty and details on the plot would be lost. The issue here is that the shape parameter acts as a singularity at the separation point. Even if *Flow* can handle the separation and the value is "numerically" correct, it does not represent the physics of the flow. The value computed by *Xfoil* is $H \sim 4$. However, *Xfoil* encounters the same problem with its *simultaneous* coupling which computed a high value of the shape parameter. Therefore, a kind of *inverse* coupling method was implemented to overcome the singularity. At the location of the separation, *Xfoil* prescribes the value of the shape parameter and it is not an unknown anymore.

Further investigations in the literature shows that the singularity could be avoided, or at least reduced, by implementing the *unsteady* integral boundary layer equations since unsteady effects become more important near the stagnation point, as explained in Bijleveld [18] and Ozdemir et al. [67]. Moreover, steady solutions may simply not exist for separated flows and the physics cannot be represented with these steady equations without prescribing the shape parameter.

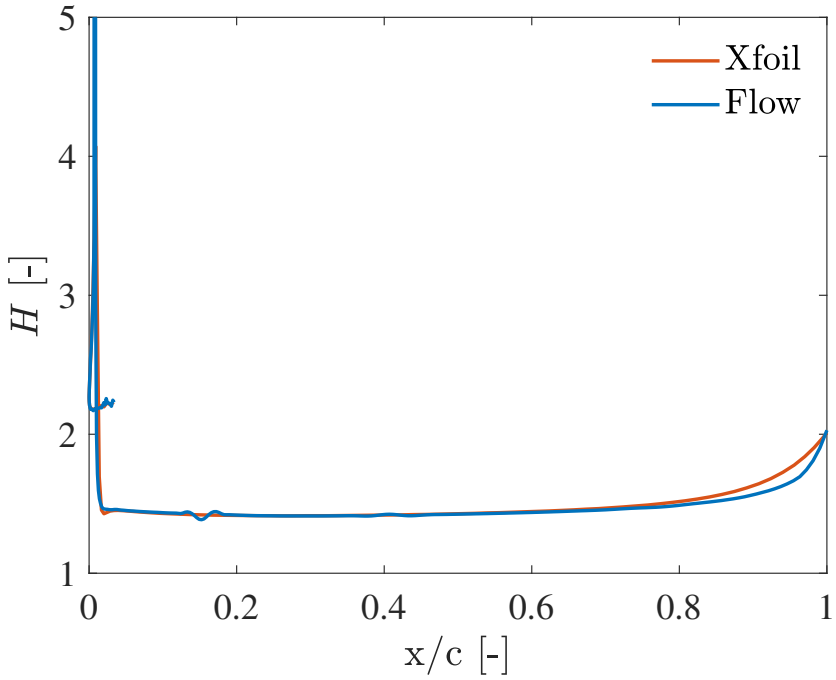

Figure 5.3.3: Variation of the shape parameter H along the chord on the suction side of the NACA 0012 at $Re = 10^7$ and $\alpha = 12°$.

The second observation is the apparition of oscillations before $x/c = 0.2$. Since the initial velocity is relatively smooth at that location, as seen in Fig. 5.3.5, these oscillations do not come from the irregularities of the initial conditions but come from the interaction between the inviscid and the viscous solvers. Currently, the author cannot explain the presence of these oscillations.

The same spurious features are observed on the pressure side of the airfoil, as seen in Fig. 5.3.4. There is a high increase of the shape parameter H near the separation point at the trailing edge. However, this separation point is predicted by *Flow* but not by *Xfoil*. Then, similar oscillations such as on the suction side are observed at the location $x/c = 0.75$.

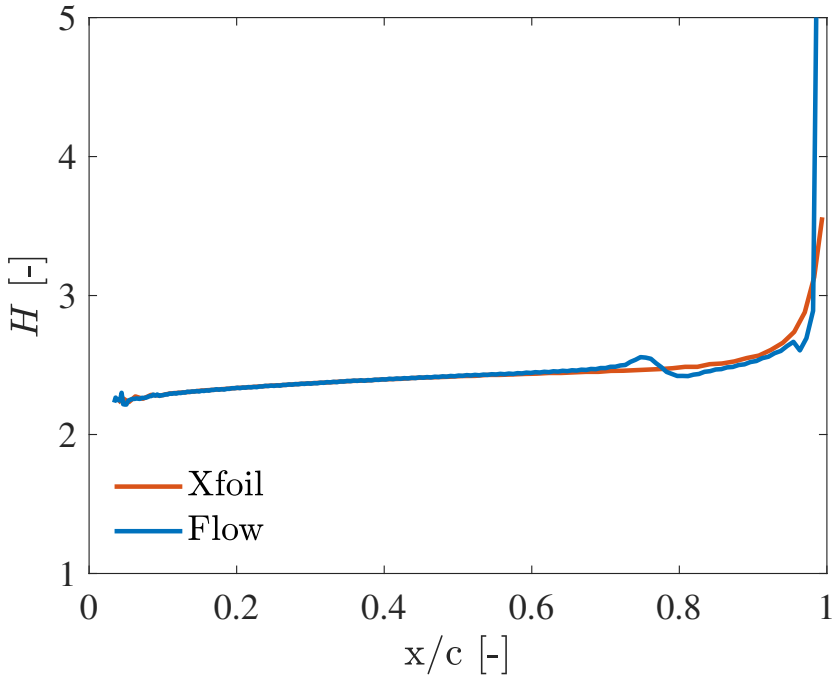

Figure 5.3.4: Variation of the shape parameter H along the chord on the pressure side of the NACA 0012 at $Re = 10^7$ and $\alpha = 12°$.

Fig. 5.3.5 shows the variation of the skin friction coefficient C_f on the suction side of the airfoil. Even if the shape parameter H computed at the separation is too high, there is a good agreement between the values predict by *Flow* and *Xfoil*. The separation is correctly predicted when the skin friction coefficient is below zero. The main discrepancies between the two software is the presence of oscillations below $x/c = 0.2$ in *Flow*.

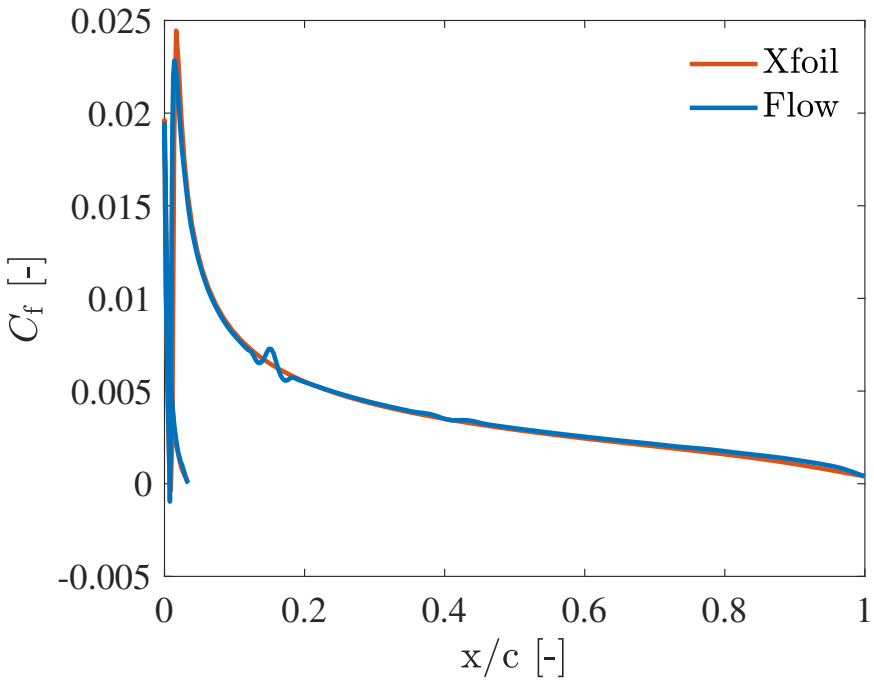

Figure 5.3.5: Variation of the skin friction coefficient C_f along the chord on the suction side of the NACA 0012 at $Re = 10^7$ and $\alpha = 12°$.

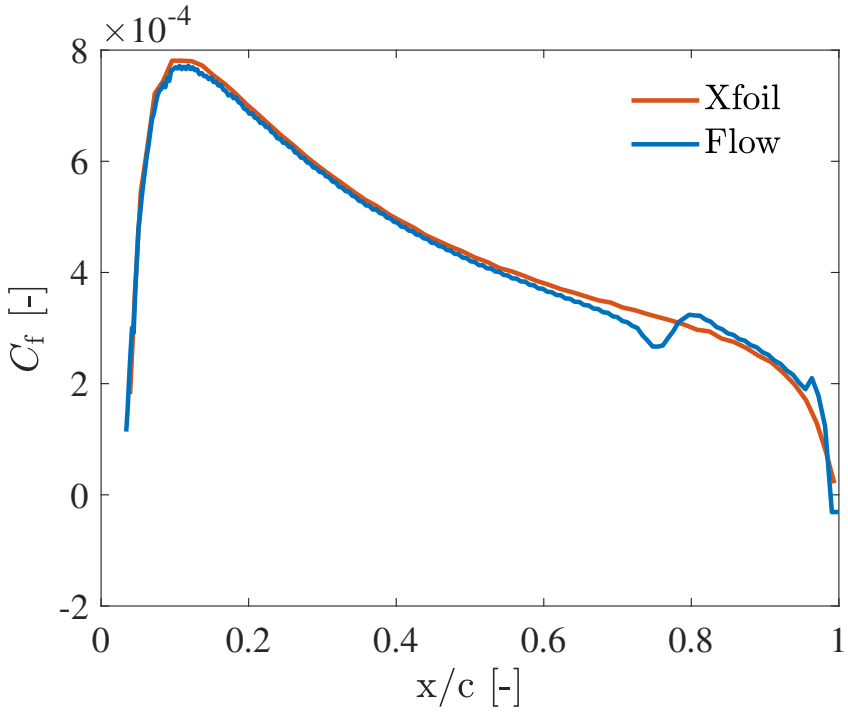

Figure 5.3.6: Variation of the skin friction coefficient C_f along the chord on the pressure side of the NACA 0012 at $Re = 10^7$ and $\alpha = 12°$.

On the pressure side, the peak is well caught by *Flow* as illustrated in Fig. 5.3.6. This is due to the good agreement between the inviscid solvers as shown in Fig.5.3.2b. There is a unexpected behaviour of the skin friction coefficient C_f at the location of the spurious oscillations such as on the suction side. At the trailing edge, *Flow* computes a laminar separation where the skin friction is below zero which is not predicted by *Xfoil*. Otherwise, there is a good correspondence between the values computed by the two viscous solvers.

Fig. 5.3.7 shows the variation of the displacement thickness δ^* on the suction side of the airfoil. It is a good summary of the what is happening in the boundary layer computation. The first point is a relatively higher displacement thickness prediction by *Flow* than *Xfoil* at the separation point due to the presence of the singularity. The second point is the presence of oscillations below $x/c = 0.2$ in *Flow*. The last point is an underestimation of the momentum thickness θ and the shape parameter H near the trailing edge. Otherwise, *Flow* tends to a similar behaviour than *Xfoil*.

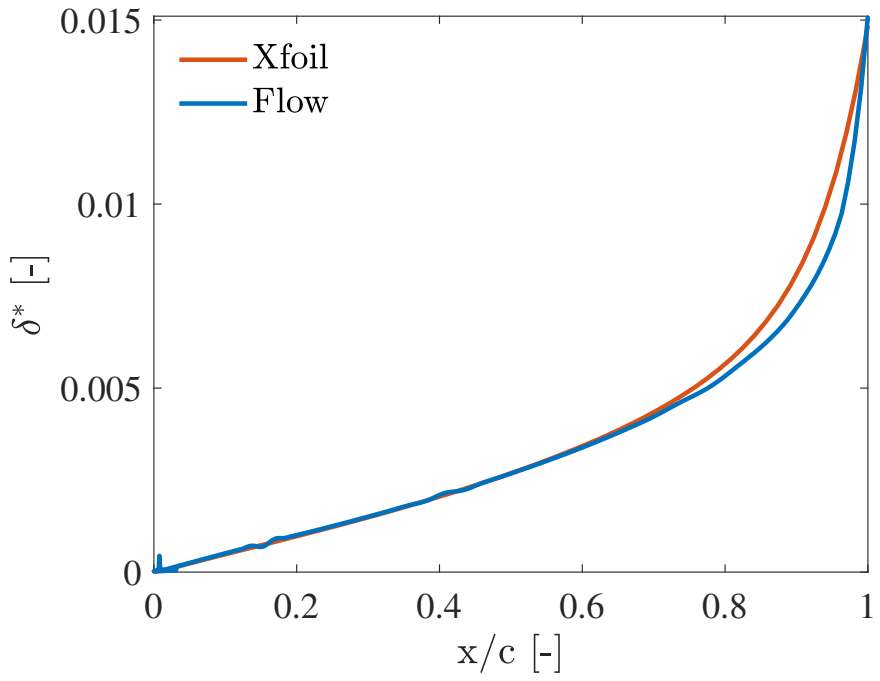

Figure 5.3.7: Variation of the displacement thickness δ^* along the chord on the suction side of the NACA 0012 at $Re = 10^7$ and $\alpha = 12°$.

Similarly, Fig. 5.3.8 shows the variation of the displacement thickness δ^* on the pressure side. The same comments are done. There are spurious oscillations at $x/c = 0.75$ and a relatively high increase of the boundary layer displacement thickness near the trailing edge, at the point of the flow separation. Since the flow remains laminar along the pressure side, the impact of the singularity on the displacement thickness is more important as on the suction side. As a matter of fact, the turbulent momentum thickness θ on the suction side is the driving parameter of the displacement thickness. On the pressure side, the driving parameter is the laminar shape factor H.

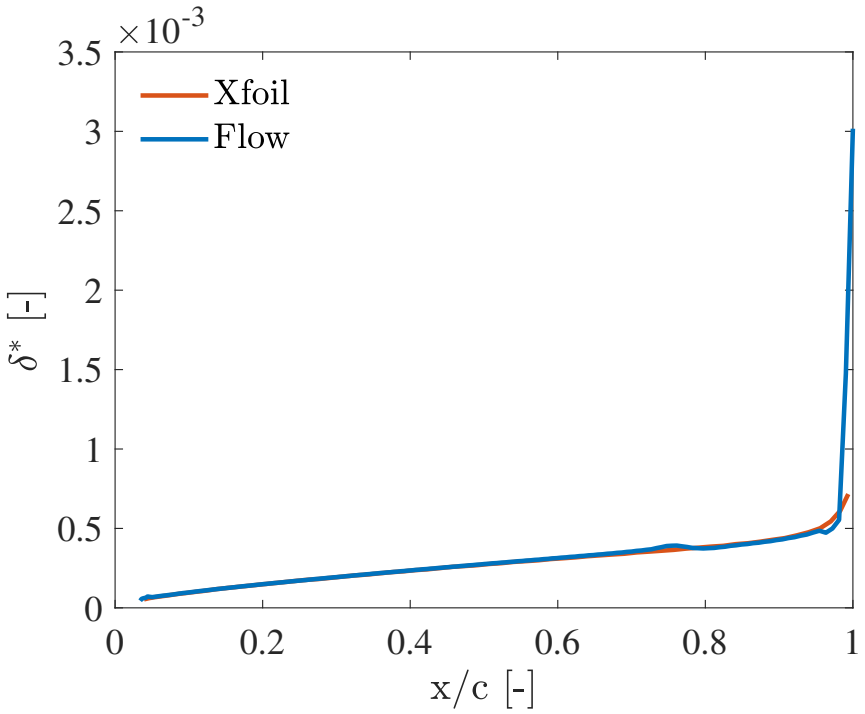

Figure 5.3.8: Variation of the displacement thickness δ^* along the chord on the pressure side of the NACA 0012 at $Re = 10^7$ and $\alpha = 12°$.

Finally, Fig. 5.3.9 illustrates the distributions of the pressure coefficients along the airfoil. Since the discussion between the two inviscid solvers is the same as for Fig. 5.2.9, these curves are not represented and only the curves from the viscous solvers are shown. The values computed by *Flow* match well the values computed by *Xfoil*. The suction peak is well caught and the trailing edge pressure is equivalent. The main issue from *Flow* is, again, the presence of oscillations below $x/c = 0.2$.

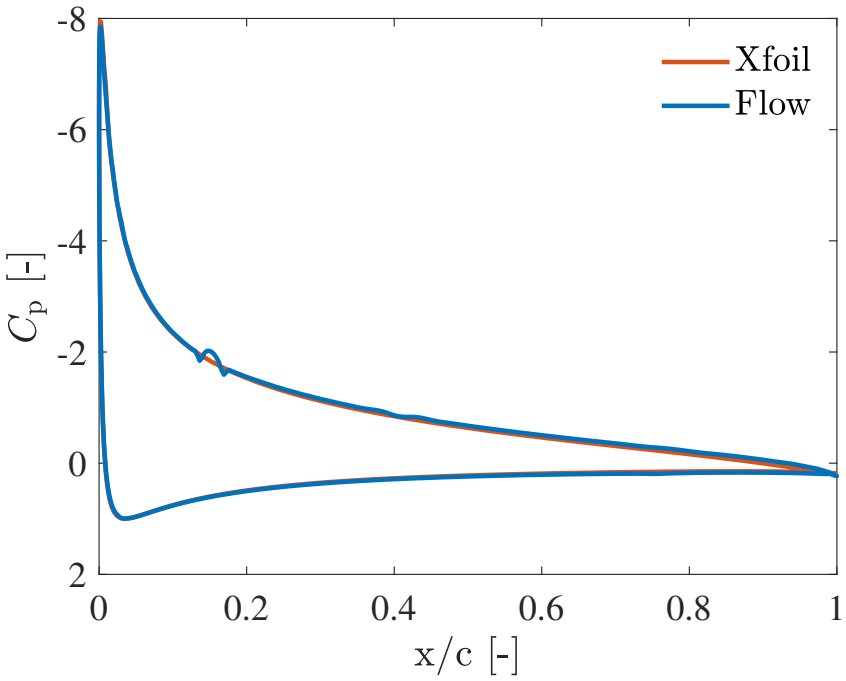

Figure 5.3.9: Pressure coefficients C_p distributions along the NACA 0012 at $Re = 10^7$ and $\alpha = 12°$.

5.3.3 Discussion

Tab. 5.3.2 lists the aerodynamic loads and the locations of the transition predict by both solvers for an incompressible separated flow around a NACA 0012 airfoil.

	$C_{p_{min}}$	c_l	c_d	x_{tr}^{top}	x_{tr}^{bot}
Xfoil	-7.947	1.33	0.011	0.011	1
Flow	-7.854	1.39	0.011	0.008	1

Table 5.3.2: Comparison of the aerodynamic loads and the locations of the transition between *Xfoil* and *Flow* for the NACA 0012 at $Re = 10^7$ and $\alpha = 12°$.

Even if in this case, the relative error on the top location of the transition is relatively high, it represents again an error lower than 0.5% of the percentage of the chord. Again, *Flow* overestimates the lift coefficient compared to *Xfoil*. However, the computed drag coefficients are the same. There is a good agreement between the values computed by *Flow* and *Xfoil*.

The purpose of this test case was to analyse the behaviour of the numerical simulation for a separated flow and to understand the limits of the viscous-inviscid interaction scheme implemented in this work. *Flow* provides good results for the test case and can be used for engineering applications. However, few problems appear; the first one is the shape factor singularity at the separation point and the second one is the apparition of spurious oscillations. *Flow* can handle the singularity but it is not physically correct. Further researches show that two solutions can be implemented to overcome the singularity: the development of an *inverse* coupling method as in *Xfoil* and the implementation of the unsteady boundary layer equations to better fit with reality near the separation point. On the other hand, there is currently no idea of solution to avoid the spurious oscillations.

Finally, the two first test cases show that the theoretical model derived in Chapter 2 & Chapter 3 meet the objectives of this work. *Flow* can deal with attached or separated, incompressible or compressible flows. However, there are still numerical problems that must be resolved in a future work.

5.4 Case 3: Highly compressible flow around a RAE 2822 airfoil

For the last test case, the purpose is to show the applicability of the numerical simulation for a highly compressible flow with a different airfoil than the NACA 0012. The RAE 2822 transonic airfoil was chosen since the aim of *Flow* is to simulate transonic flow, as explained in Crovato [1]. However, going to transonic flow capability is beyond the scope of this work. Therefore, the flow will be at the limit of the high subsonic condition to remain in the limit of validity of the Karman-Tsien compressibility correction used in *Xfoil* [32] and in the limit of validity of the model presented in this thesis. For that, an angle of attack of $0.5°$ and a Mach number $M_\infty = 0.7$ are chosen.

5.4.1 Input parameters

As explained in test case 1, the numerical simulation of compressible flows is more sensitive to irregularities in the initial conditions due to the dependence on the edge velocity u_e as well as the edge Mach number M_e. To overcome these irregularities, a stricter filter is applied. A bandwidth m of 21 points and a polynomial order p of 3 are prescribed. A mesh ratio of $1/5$ between the leading edge and the trailing edge is used. The number of points near the trailing edge is increased since the various peaks of pressure are not happening at the leading edge but further downstream for a supercritical airfoil.

Input parameter	**Values**
Reynolds number	6.5×10^6
Mach number	0.7
Angle of attack	$0.5°$
Mesh size at the leading-edge	0.001 [m]
Mesh size at the trailing-edge	0.005 [m]
Polynomial order of the filter p	3
Bandwidth m	21

Table 5.4.1: Input parameters for the simulation of a highly compressible flow around the RAE 2822 at $Re = 6.5 \times 10^6$, $\alpha = 0.5°$ and $M_\infty = 0.7$.

Fig. 5.4.1 illustrates the geometry of the supercritical airfoil and the mesh used for the simulation.

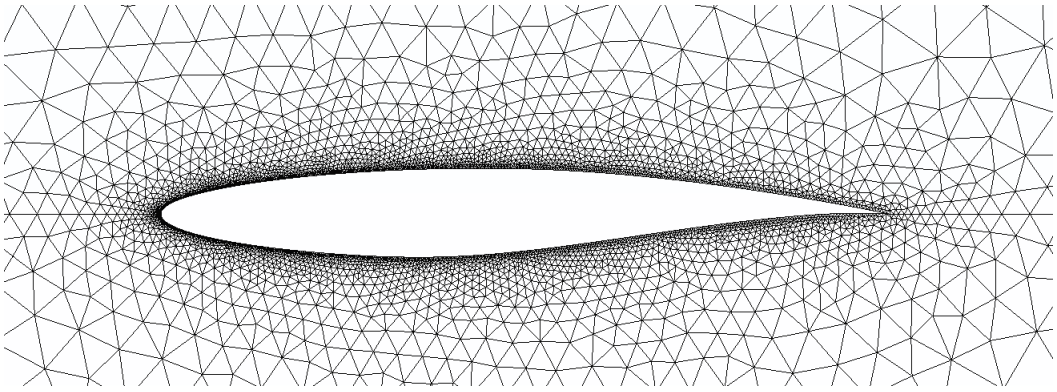

Figure 5.4.1: Representation of the geometry of the RAE 2822 and the mesh used for the simulation.

As seen in Fig. 5.4.2a, the filtered initial inviscid velocities computed by *Flow* and the initial inviscid velocities computed by *Xfoil* are different along the chord on the suction side. This difference will impact the boundary layer simulation and the parameters will present different behaviours. Then the results are compared to the higher fidelity simulation *SU2*. This comparison shows that the trend of *Flow* is similar to the one of *SU2* but the velocities are overestimated. On the other hand, the behaviour predicted by *Xfoil* does not match the behaviour of *SU2* at all. Therefore, the trend of the results of *Flow* will be more reliable than *Xfoil* for the simulation along the suction side of the RAE 2822 for this test case.
The pressure side presents an identical behaviour for the different inviscid solvers as seen in Fig. 5.4.2b. Each peak is well caught by *Flow* and there is no irregularities in the initial conditions.

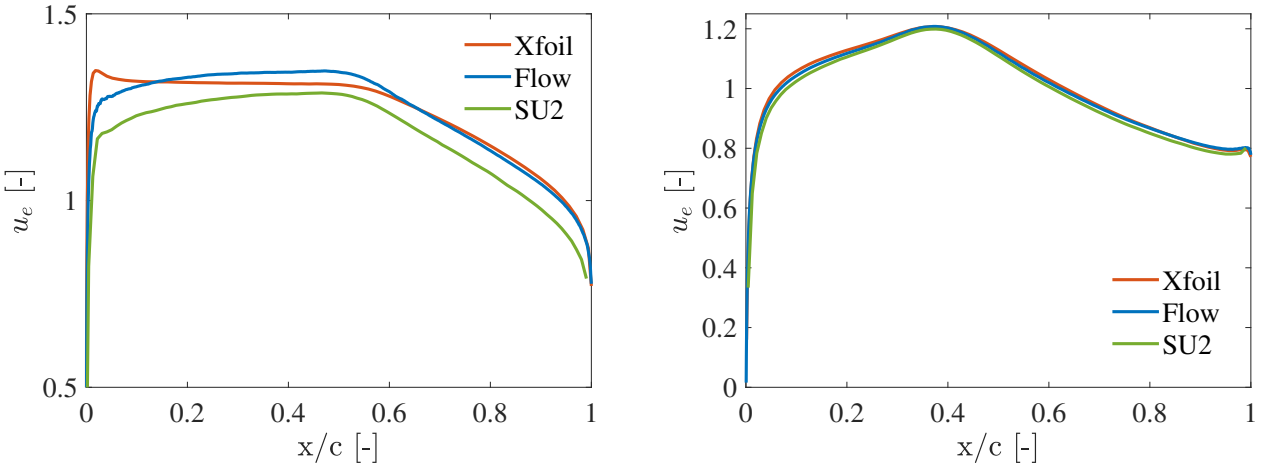

(a) Suction side

(b) Pressure side

Figure 5.4.2: Comparison between the inviscid velocity of *Xfoil* and *Flow* along the RAE 2822 at $Re = 6.5 \times 10^6$, $\alpha = 0.5°$ and $M_\infty = 0.7$.

5.4.2 Results

Fig. 5.4.3 shows the variation of the shape parameter H along the chord on the suction side of the RAE 2822 computed by *Flow* and *Xfoil*. As expected by the inviscid velocities, the results are not similar until the velocities become almost identical at $x/c \sim 0.65$. The shape parameter predicted by *Flow* is not constant during the laminar flow contrarily to the one predicted by *Xfoil* since the velocity is not constant on that portion of the suction side, as seen in Fig. 5.4.2a. Moreover, the transition location is determined further downstream than the one determined by *Xfoil*.

On the pressure side, the shape parameter H computed by both viscous solvers is almost equivalent, as seen in Fig. 5.4.4. This result was expected due to the good agreement between the inviscid velocities computed by the two inviscid solvers and represented in Fig. 5.4.2b. The only exception is at the transition where *Flow* computes a higher peak of shape parameter than *Xfoil*. This difference is mainly due to the prediction of a small laminar separation just before the transition by *Flow* and not by *Xfoil*.

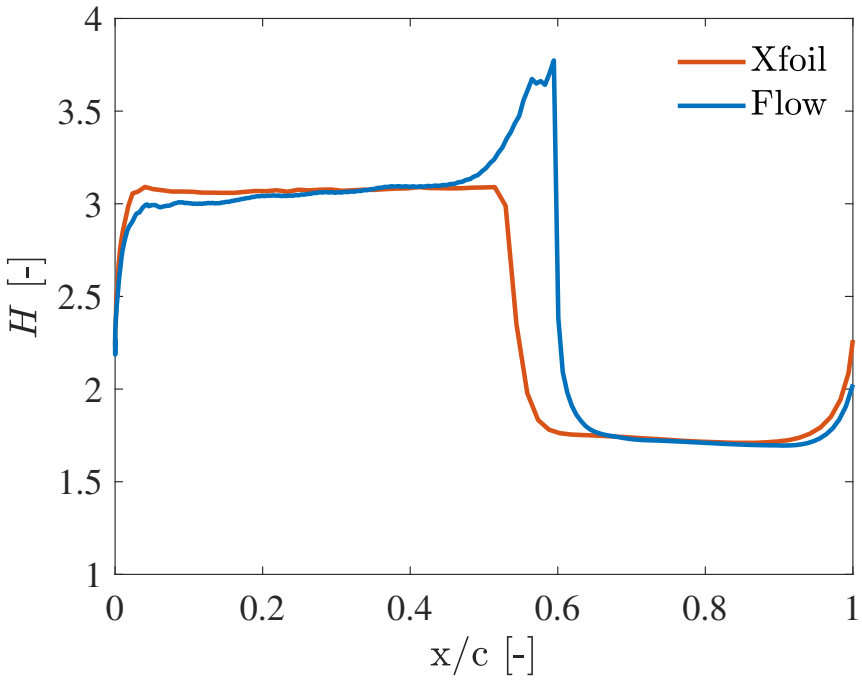

Figure 5.4.3: Variation of the shape parameter H along the chord on the suction side of the RAE 2822 at $Re = 6.5 \times 10^6$, $\alpha = 0.5°$ and $M_\infty = 0.7$.

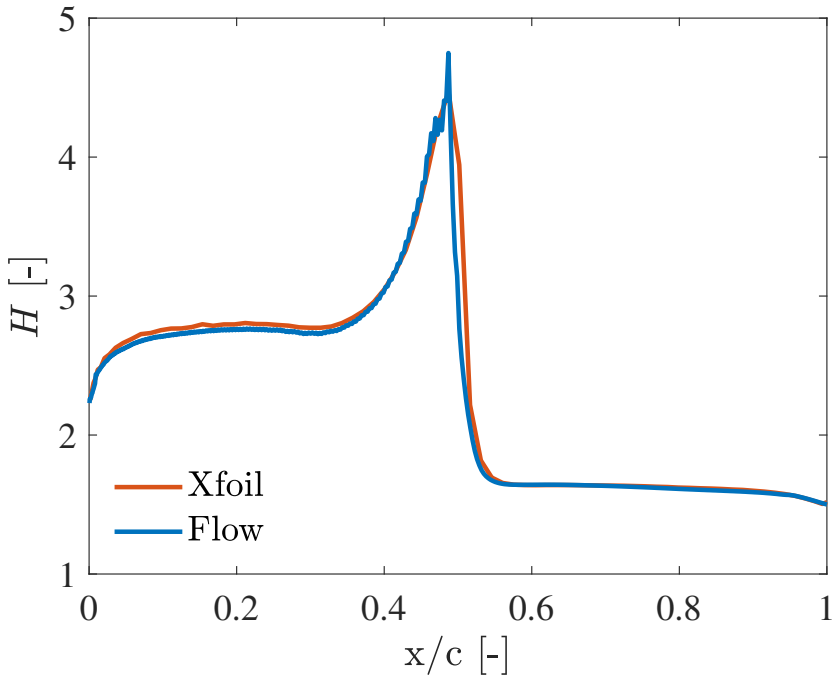

Figure 5.4.4: Variation of the shape parameter H along the chord on the pressure side of the RAE 2822 at $Re = 6.5 \times 10^6$, $\alpha = 0.5°$ and $M_\infty = 0.7$.

The skin friction coefficient C_f along the chord on the suction side is represented in Fig. 5.4.5. Again, the distributions are different from both viscous solvers due to the difference in the velocity distributions. However, the skin friction coefficient predicted by *Flow* behaves logically. First, it increases due to the velocity gradient at the leading edge. Then, it decreases up to the laminar to turbulent transition where it increases dramatically. Finally, it decreases until the end. This behaviour is similar to the behaviour predicted by *Xfoil* except that the transition is located further upstream for *Xfoil*.

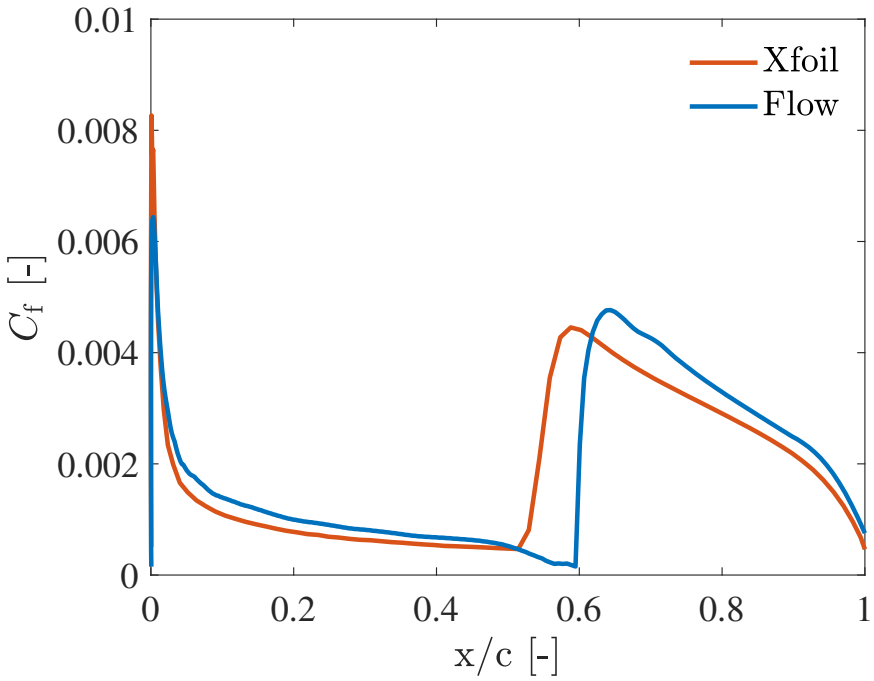

Figure 5.4.5: Variation of the skin friction coefficient C_f along the chord on the suction side of the RAE 2822 at $Re = 6.5 \times 10^6$, $\alpha = 0.5°$ and $M_\infty = 0.7$.

On the pressure side, there is a good agreement between the skin friction coefficients C_f computed by both viscous solvers, as seen in Fig. 5.4.6. The discrepancies between the two curves come from the small differences between the inviscid velocities. However, *Flow* predicts a small separation ($C_f \sim -10^{-6}$) before the transition while *Xfoil* does not.

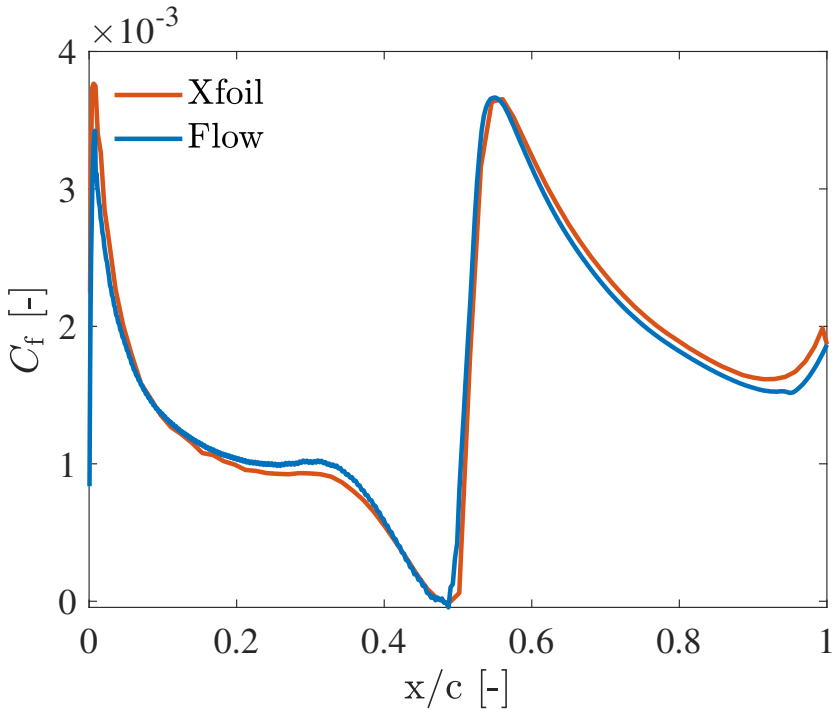

Figure 5.4.6: Variation of the skin friction C_f along the chord on the pressure side of the RAE 2822 at $Re = 6.5 \times 10^6$, $\alpha = 0.5°$ and $M_\infty = 0.7$.

As expected from the previous analysis, the displacement thickness δ^* computed by *Flow* is simply shift further downstream compared to the displacement thickness computed by *Xfoil*, as seen in Fig. 5.4.7. The behaviour is the same for both viscous solvers.

Fig. 5.4.8 shows the variation of the displacement thickness δ^* along the chord on the pressure side of the airfoil. The behaviour of *Flow* is in line with the expectations of the previous results. The values in the laminar and turbulent portions of the chord are equivalent between the two solvers. A higher peak of displacement thickness is computed by *Flow* at the transition location due to the presence of the small separation.

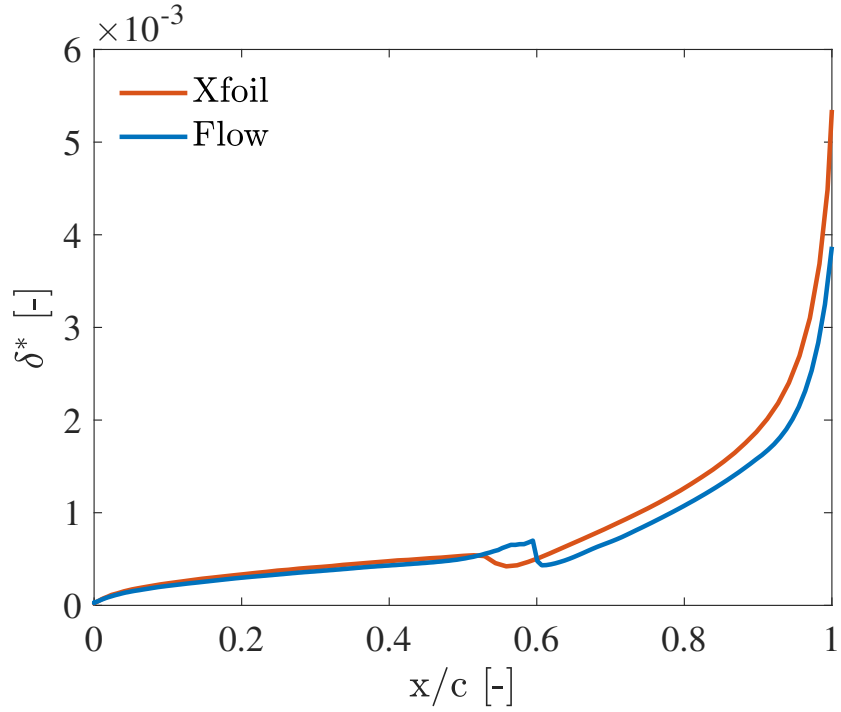

Figure 5.4.7: Variation of the displacement thickness δ^* along the chord on the suction side of the RAE 2822 at $Re = 6.5 \times 10^6$, $\alpha = 0.5°$ and $M_\infty = 0.7$.

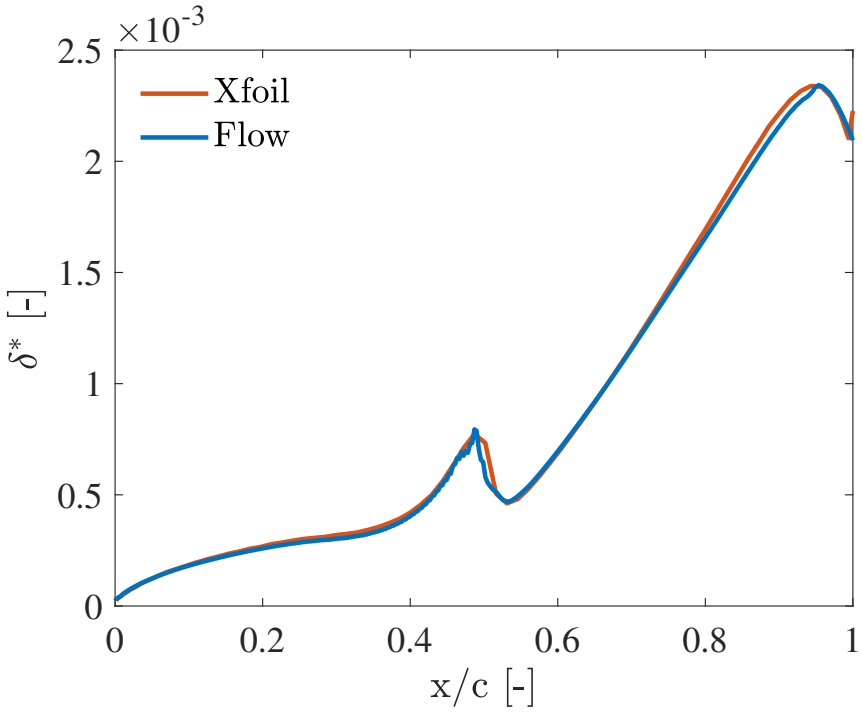

Figure 5.4.8: Variation of the displacement thickness δ^* along the chord on the pressure side of the RAE 2822 at $Re = 6.5 \times 10^6$, $\alpha = 0.5°$ and $M_\infty = 0.7$.

Fig. 5.4.9 illustrates the pressure coefficients distribution computed by *Flow* and *Xfoil* which solve the viscous-inviscid interaction scheme and computed by *SU2* which solves the RANS equations with a transition model[2]. The pressure coefficients distribution of *Flow* is relatively similar to the distribution of *SU2* and the transition locations are well predicted. The discrepancies between the two distribution come from the discrepancies between the inviscid velocities computed by both software as seen in Fig. 5.4.2a. On the suction, the prediction of *Flow* are better than *Xfoil*. On the pressure side, *Flow* tends to overestimate the pressure coefficients distribution contrarily to *Xfoil*.
The interesting feature is that the computational time of *Flow* was of the order of the seconds while the computational time of *SU2* was of the order of hours.

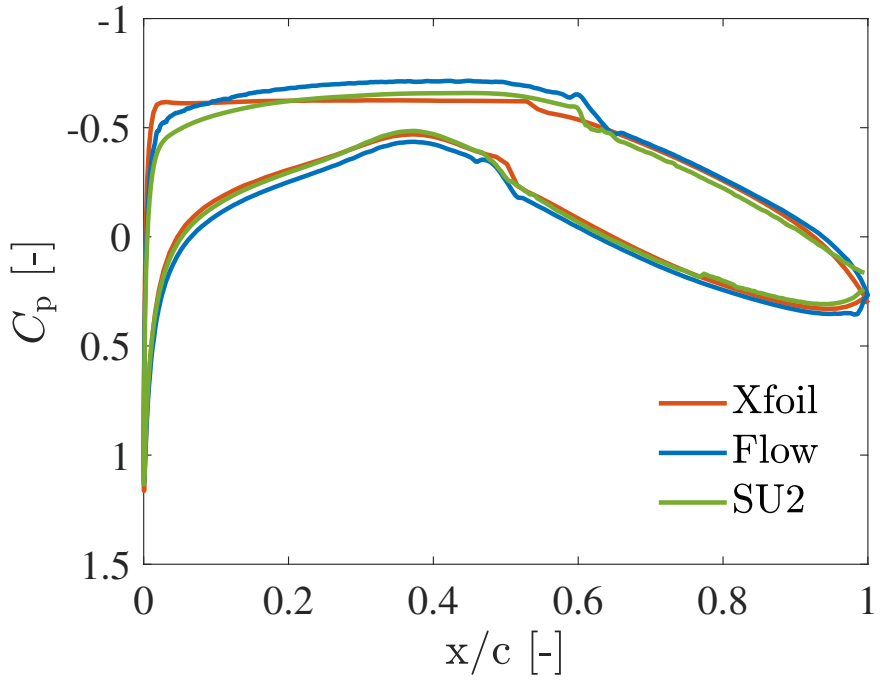

Figure 5.4.9: Pressure coefficients C_p distribution along the RAE 2822 at $Re = 6.5 \times 10^6$, $\alpha = 0.5°$ and $M_\infty = 0.7$.

[2]More details about the simulation in Appendix A.2.

5.4.3 Discussion

Tab. 5.3.2 lists the aerodynamic loads and the locations of the transition predicted by both solvers for a highly compressible flow around a RAE 2822.

	$C_{\mathrm{p_{min}}}$	c_l	c_d	x_{tr}^{top}	x_{tr}^{bot}
Xfoil	-0.625	0.373	0.0044	0.525	0.499
Flow	-0.714	0.454	0.0039	0.595	0.483
SU2	-0.659	0.359	0.0045	0.605	0.473

Table 5.4.2: Comparison of the aerodynamic loads and the locations of the transition between *Xfoil*, *Flow* and *SU2* for the RAE 2822 at $Re = 6.5 \times 10^6$, $\alpha = 0.5°$ and $M_\infty = 0.7$.

While the transition locations are accurately predicted by *Flow*, it is not the case for the aerodynamic loads. For the lift coefficient, the difference is mainly due to the difference between the initial inviscid velocities. For the drag coefficient, the difference is due to the underestimation of the momentum thickness θ by the viscous solver of *Flow*. Moreover, the strict filtering parameters can be a source of error during the interactions between the viscous and the inviscid solvers.

In this test case, the viscous-inviscid interaction has been tested on a highly compressible flow around a different airfoil than the NACA 0012 and compared to a RANS simulation. Even if *Flow* globally fits with the behaviour of *SU2*, various sources of error occur. The main error comes from the velocity prediction of the inviscid solver which overestimates the initial inviscid velocity. Then, the initial conditions are too smoothed by the viscous solver to ensure the proper functioning of the simulation. This error is repeated along all the interaction cycles. Further investigations should be carried out to make *Flow* fully effective.
However, the boundary layer parameters are well predicted by the viscous solver. There is almost a perfect match when the inviscid velocities of *Flow* and *Xfoil* are identical. Moreover, the computational time of *Flow* is of the order of the seconds which is interesting during preliminary design of an aircraft.

Chapter 6

Conclusions and perspectives

6.1 Conclusions

In this work, a viscous-inviscid interaction has been implemented in a finite element full potential solver. The combination of the inviscid and the viscous solvers allows to study the effects of the boundary layer in a flow around an airfoil with accuracy. These effects concern the global parameters such as the displacement thickness, the shape parameter or the skin friction coefficient. This method reduces the computational cost compared to a higher fidelity simulation such as *DNS* or *RANS* which is ideal during the preliminary design of an aircraft. The procedure implemented allows to simulate attached and separated flows and allows to take into account the compressiblity effects up to the high subsonic limit. The case studies were performed on a NACA 0012 airfoil and on a RAE 2822 supercritical airfoil.

First, the theoretical model has been defined. The inviscid formulation consists in the full potential equation discretized by a finite element method. This solver is the base of *Flow* and is already implemented in the beginning of the present thesis. Then, the viscous formulation is introduced by deriving the integral boundary layer equations from the boundary layer concept. This formulation allows to reduce by one the number of dimension and to take only the global parameters into account. The integral model used is the two-equations dissipation integral method which consists in the von Kármán equation and the kinetic energy shape parameter equation. For a laminar flow, an amplification ratio equation is added to the system to compute the transition location. For a turbulent flow, a shear lag equation is added to take into account the Reynolds shear stresses. Then, a set of closure terms is derived for both the laminar or the turbulent case. The main advantage of this model is that it can handle separation and compressibility effects.

After that, a coupling method has been investigated. This coupling is based on two parameters: the blowing velocity which describes the impact of the boundary layer on the inviscid flow and the edge of the boundary layer velocity which describes the impact of the external flow on the boundary layer. All the different methods existing in the literature have been presented and their strengths and weaknesses have been explained. From this analysis, two types of interaction are defined: the weak interaction which creates a hierarchy between the two solvers solution and the strong interaction which assumes no hierarchy between the solvers solution. The latter is preferable to handle separated flow. Hence, a quasi-simultaneous coupling has been chosen since it allows an easy implementation on an existing solver. The interaction law has been derived from the triple deck theory to be robust and simple.

The numerical procedure has been presented. The initialization of the computation is explained and the boundary and initial conditions are defined. Since the initial conditions from the inviscid solver present irregularities, a filter has been chosen. This filter allows to improve the smoothness of the initial conditions but it can reduce the accuracy of the results by smoothing the variation of the velocity brought by the viscous solver during the interaction procedure. Then, the boundary layer solver strictly speaking has been introduced. The equations are discretized with a finite-difference method. The scheme applied is the second order trapezoidal scheme except at the leading edge and the transition. To increase the stability at that locations, upwinding has been added to the set of equations and a backward Euler scheme is used instead of the trapezoidal scheme. The system of first order, non linear, coupled ordinary differential equations is resolved by a Newton procedure. First, the system is linearized by the use of the Jacobian matrix. Then, the linear system is resolved thanks to a LU decomposition. A backtracking line search algorithm has been also implemented to optimize the procedure. Special treatments have been put in place to take into account the transition and the wake and to improve the stability of the simulation. Finally, the convergence criterion based on the drag coefficient has been introduced.

Different test cases were performed to compare the viscous-inviscid interaction with the software *Xfoil*. The first investigated case was the simulation of an attached flow either incompressible or compressible at a Reynolds number $Re = 10^7$, an angle of attack $\alpha = 5°$, a Mach number $M_\infty = 0$ for the incompressible case and $M_\infty = 0.5$ for the compressible case. This test case has shown an excellent agreement between the values computed by *Flow* and *Xfoil* for both cases. For the compressible case, few discrepancies between the two software appeared due to the presence of oscillations in the solution computed by *Flow*. However, it has been proven that the differences originate from the inviscid solver of

Flow which gave irregular initial conditions to the viscous solver. Hence, the oscillations were created by these irregularities in this case. Apart from these differences, the viscous-inviscid interaction predicted correct boundary layer parameters, aerodynamic loads and transition locations for an attached flow either incompressible or compressible.

The second test case was carried out on the simulation of a separated incompressible flow at a Reynolds number $Re = 10^7$ and an angle of attack $\alpha = 12°$. Few discrepancies between the two software appeared. There is the presence of a singularity in the shape parameter at the point of flow separation and the presence of spurious oscillations on the suction and pressure sides which did not come from the inviscid solver. While possible solutions have been provided for the first one, the second one is still under resolution. However, the test case has illustrated that the viscous-inviscid interaction shows good agreements with *Xfoil* for the boundary layer parameters, the aerodynamic loads and the transition locations even in the case of separated flow.

The third case was performed on a highly compressible flow around the RAE 2822 airfoil at a Reynolds number $Re = 6.5 \times 10^6$, an angle of attack $\alpha = 0.5°$ and a Mach number $M_\infty = 0.7$. During this case, the viscous-inviscid scheme has been compared to a higher fidelity simulation, the RANS equations. Even if the viscous solver correctly computed the boundary layer parameters and the locations of the transition, it had difficulty to predict the correct pressure coefficients distribution and hence, the aerodynamic loads. The lift coefficient has been overestimated and the drag coefficient has been underestimated. However, the global behaviour of results from *Flow* fits with the results from *SU2* at a computational cost of the order of seconds.

Finally, the viscous-inviscid interaction method developed in *Flow* offers interesting features for flow simulations. The theoretical model is robust and the numerical implementation works well. However, further investigations must be performed on the different sources of error to make it fully efficient.

6.2 Further works

In this section, some indications are given for future works. Currently, the viscous-inviscid interaction scheme is limited to two-dimensional highly compressible but not transonic flows. However, the inviscid solver of *Flow* has been developed with the main objective to compute three-dimensional transonic flows.

6.2.1 Transonic capability

The first interesting future feature that could be added is the capability to compute viscous transonic flows. In order to do this, some of the current implementation issues must be dealt with such as the singularity in the shape parameter at flow separation and the oscillations from the inviscid solver. Currently, the latters tend to make the solution crash for transonic flows.

Therefore, to reach transonic capability, only a few modifications need to be done. The singularity can be overcome by the application of an inverse procedure such as in *Xfoil*. A weak condition can be imposed on the shape parameter at the point of flow separation and the correct behaviour of the flow will be recovered. The oscillations are disturbing in several respects, they cause perturbations at each coupling iteration and they induce unexpected behaviour in the code. To stop using the filter used to reduce the oscillations but which tends to dissipate the results, a new mesh procedure could be put in place when the viscous solver is employed. The mesh of the inviscid region could remain the same but a new structured mesh could be construct in the viscous region. Hence, smooth initial conditions could be retrieved from the inviscid solver and there would no longer be a need to filter this data at each iteration. During transonic flows, the mesh size is based on the size of the shock. Since the boundary layer equations are highly dependent on the mesh size, especially at the leading edge, it would be interesting to better control the mesh for the transonic viscous-inviscid interaction. Another solution could be to keep the filter but make it smarter. It could identify and separate the spurious oscillations from the needed oscillations determined by the boundary layer equations. In this way, less data would be lost during the interaction procedure.

Based on the ability to compute flows in the transonic regime, shock-wave boundary layer interactions could be investigated. Since this mechanism is highly unsteady, an adapation must be done for both the inviscid and viscous solvers. The inviscid solver is currently under investigation in order to model unsteady flows with the unsteady full potential equation. For the viscous solver, the unsteady integral boundary layer equations could be used instead of the steady ones. A great interest with these equations is that they decrease the sensitivity of the system to perturbations and hence, to the singularity and the oscillations present in the simulation.

6.2.2 Three-dimensional flow

Since the inviscid solver of *Flow* is able to compute three-dimensional flows, it would be interesting to extend the features of the viscous-inviscid interaction to handle this kind of flow. A traditional approach is to couple a 2D integral boundary layer formulation to a general 3D inviscid formulation. In practice, the 2D boundary layer equations are solved along strips which are stations defined in the streamwise direction of the flow along the wing as seen in Fig. 6.2.1.

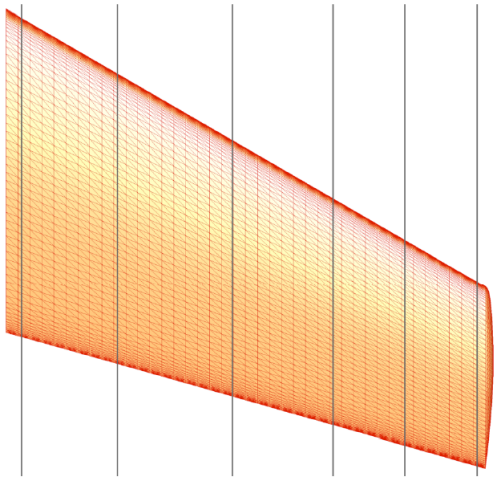

Figure 6.2.1: Strip distribution along the wing. Taken from Aftosmis et al. [41]

By extending the 2D integral formulation to include the effects of lateral divergence and sweep, the method will be valid in quasi-2D flows and could handle high aspect ratio, swept and tapered wings as well as fuselages. This method is implemented in the well known *Tranair* code, as explained in Bieterman et al. [68]. However, this method is limited in the case of real 3D flow features such as wing root and tip regions, wing/fuselage and tail/fuselage intersections.

To take these features into account, a 3D integral boundary layer formulation could be applied. A review of the various formulations can be found in van Garrel [69]. The simplest implementation is to formulate the method in curvilinear coordinates which cover the body surface. However, the presence of slope discontinuities causes difficulties with such coordinates since they appear as singularities in the surface curvature as noted by Drela [70].
To overcome this issue, the method could be formulated in terms of cartesian coordinates. In the work of Nishida [13], the integral boundary layer equations are defined by three equations. The first two equations represent streamwise profile modes and the last equation represents a crossflow mode. This method

gave results which were not accurate due to the single equation for the crossflow mode. Finally, Drela [70] improved the 3D formulation with cartesian coordinates by employing four equations to model the streamwise and crossover profiles.

In *Flow*, it would be interesting to implement the quasi-2D method in a first time. This method would work without modifying entirely the viscous solver such as the other methods. The only adaptations that must be done are the introduction of the effects of lateral divergence and sweep and the implementation of the strips along the wing.

Bibliography

[1] A. Crovato et al. “A full potential static aeroelastic solver for preliminary aircraft design”. In: *International Forum on Aeroelasticity and Structural Dynamics* (2019).

[2] L. Prandtl. “Ueber Fluessigkeitsbewegung mit kleiner Reibung”. In: *Verhandlungen des dritten internationalen Mathematischen Kongresses* (1905), pp. 484–491.

[3] A.E.P Veldman. “New, quasi-simultaneous method to calculate interacting boundary layers”. In: *AIAA paper* (1981).

[4] A. Crovato. “Steady Transonic Aerodynamic and Aeroelastic Modeling for Preliminary Aircraft Design”. PhD thesis. University of Liège, 2020.

[5] C. C. L. Sells. *Two-dimensional Laminar Compressible Boundary layer Programme for a Perfect Gas*. Tech. rep. R.A.E., 1968.

[6] Th. V. Kármán. “Über laminare und turbulente Reibung”. In: *ZAMM - Journal of Applied Mathematics and Mechanics / Zeitschrift für Angewandte Mathematik und Mechanik* (1921), pp. 233–252.

[7] J. D. Anderson. *Fundamentals of aerodynamics*. 5th. McGraw-Hill, Feb. 2011.

[8] E. Pohlhausen. “Der Wärmeaustausch zwischen festen Körpern und Flüssigkeiten mit kleiner reibung und kleiner Wärmeleitung”. In: *ZAMM - Journal of Applied Mathematics and Mechanics / Zeitschrift für Angewandte Mathematik und Mechanik* (1921), pp. 115–121.

[9] B. Thwaites. “Approximate calculation of the laminar boundary layer”. In: *Aeronautic* (1949), pp. 245–280.

[10] M.R Head. *Entrainment in the turbulent boundary layer.* Tech. rep. Aeronautical Research Council R&M 3152, 1960.

[11] M. Drela and M. Giles. “Viscous-Inviscid Analysis of Transonic and Low Reynolds Number Airfoils”. In: *AIAA Journal* (1987).

[12] J.L. Thomas. “Integral boundary-layer models for turbulent separated flows”. In: *17th Fluid Dynamics, Plasma Dynamics, and Lasers Conference,* 1 (1984).

[13] B. Nishida and M. Drela. “Fully simultaneous coupling for three-dimensional viscous/inviscid flows”. PhD thesis. Massachusetts Institute of Technology, 1995.

[14] J.C Le Balleur. “Strong Matching Method for Computing Transonic Viscous Flows Including Wakes and Separations on Lifting Airfoils”. In: *La Recherche Aérospatial* (1987).

[15] D.L Whitfield. “Analytical Description of the Complete Turbulent Boundary Layer Velocity Profile”. In: *AIAA Paper* (1978).

[16] D.J. Weeks J.E. Green and J.W.F. Brooman. *Prediction of turbulent boundary layers and wakes in compressible flow by a lag-entrainment method.* 3791st ed. Aeronautical Research Council. London, 1977.

[17] J.E. Green. *Application of Head’s Entrainment Method to the Prediction of Turbulent Boundary Layers and Wakes in Compressible Flow*. Tech. rep. R.A.E., 1976.

[18] H. Bijleveld. “A quasi-simultaneous interaction method for the determination of aerodynamic forces on wind turbine blades”. PhD thesis. University of Groningen, 2013.

[19] B. Ye. “The Modeling of Laminar-to-turbulent Transition for Unsteady Integral Boundary Layer Equations with High-order Discontinuous Galerkin Method”. MA thesis. Delft University of Technology, 2015.

[20] J.C Le Balleur. “Couplage visqueux-non visceux: méthode numérique et applications aux écoulements bidimensionnels transsoniques et supersoniques.” In: *La Recherche Aérospatial* (1978).

[21] D.L Whitfield. “Integral Solution of Compressible Turbulent Boundary Layers Using Improved Velocity Profiles”. In: *Arnold Air Force Station* (1978).

[22] M. Drela. “Two-dimensional Transonic Aerodynamic Design and Analysis Using the Euler Equations.” PhD thesis. Massachusetts Institute of Technology, 1986.

[23] R. Michel. *Etude de la transition sur les profils d’aile*. Tech. rep. ONERA Report, 1951.

[24] A.M.O Smith and N. Gamberoni. *Transition, Pressure Gradient, and Stability Theory*. Tech. rep. Douglas Aircraft Co., 1956.

[25] J.L van Ingen. *Suggested Semi-Empirical Method for the Calculation of the Boundary Layer Transition Region*. Tech. rep. Delft University of Technology, Dept. of Aerospace Engineering, 1956.

[26] H. Schlichting and K. Gersten. *Boundary-Layer Theory*. 9th ed. Springer, 2017.

[27] L.M.M Mack. *“Aerodynamic Analysis Requiring Advanced Computers*. Tech. rep. NASA, 1975.

[28] J.L van Ingen. "The e^N method for transition prediction. Historical review of work at TU Delft". In: *AIAA paper* (2008).

[29] C. Gleyzes, Jr. Cousteix, and J.L Bonnet. "Theoretical and Experimental Study of Low Reynolds Number Transitional Separation Bubbles". In: *Low Reynolds Number Airfoil Aerodynamics* (1985).

[30] T. W Swafford. "Analytical Approximation of Two-Dimensional Separated Turbulent Boundary-Layer Velocity Profile". In: *AIAA Journal* (1983).

[31] P. Bradshaw and Ferriss D. H. "Calculation of Boundary-Layer Development Using the Turbulent Energy Equation: Compressible Flow on Adiabatic Wall". In: *Journal of Fluid Mechanics* (1970).

[32] M.Drela. "Xfoil: An analysis and design system for low Reynolds number airfoils". In: *Springer* (1989).

[33] J. Moran. *An introduction to theoretical and computational aerodynamics*. John Wiley & Sons, LTD, 2003.

[34] T. Cebeci and J. Cousteix. *Modeling and Computation of Boundary-Layer Flows*. 2nd ed. Springer, 1999.

[35] M. J. Lighthill. "On displacement thickness". In: *Journal of Fluid Mechanics* 4.4 (1958), pp. 383–392.

[36] A.E.P Veldman. "Entrainment and boundary-layer separation: a modeling history". In: *Journal of Engineering Mathematics* (2017).

[37] S. Goldstein. "On laminar boundary layer flow near a position of separation". In: *The Quarterly Journal of Mechanics and Applied Mathematics* (1948), pp. 43–69.

[38] D. Catherall and K. W. Mangler. "The integration of the two-dimensional laminar boundary-layer equations past the point of vanishing skin friction". In: *Journal of Fluid Mechanics* 26.01 (1966), p. 163.

[39] L. Prandtl. *Führer durch die Strömungslehre*. Verlag Vieweg & Sohn, 1956.

[40] R.C. Lock and B.R. Williams. "Viscous-inviscid interactions in external aerodynamics". In: *Progress in Aerospace Sciences* 24 (1987), pp. 51–171.

[41] M. Aftosmis, M. Berger, and J. Alonso. "Applications of a Cartesian Mesh Boundary-Layer Approach for Complex Configurations". In: *44th AIAA Aerospace Sciences Meeting and Exhibit*. American Institute of Aeronautics and Astronautics, 2006.

[42] J.E. Carter. "Viscous-inviscid interation analysis of transonic turbulent separated flow". In: *AIAA paper* (1981).

[43] A. E. P Veldman. “The calculation of incompressible boundary layers with strong viscous-inviscid interaction”. In: *AGARD paper* (1980).

[44] G. W. Brune, P.E. Rubbert, and T.C. Nark. “New approach to inviscid flow/boundary layer matching”. In: *AIAA paper* (1974).

[45] J. Lees and B.L. Reeves. “Supersonic separated and reattaching laminar flows”. In: *AIAA paper* (1964).

[46] Tuncer Cebeci et al. “Airfoils with separation and the resulting wakes”. In: *Journal of Fluid Mechanics* 163 (1986), pp. 323–347.

[47] K. Stewartson and P.G.Williams. “Self-induced separation”. In: *Proc. R. Soc. London* (1969).

[48] A.F. Messiter. “Boundary-layer flow near the trailing edge of a flat plate”. In: *SIAM J. Appl. Math* (1970).

[49] V.Ya. Neiland. “Towards a theory of separation of the laminar boundary layer in a supersonic stream”. In: *Mekh. Zhid. Gaza,* (1969).

[50] P.Y Lagrée. *Notes on Triple Deck*. Tech. rep. CNRS & UPMC Université Paris, 2018.

[51] E.G.M. Coenen. “Viscous-Inviscid Interaction with the Quasi-Simultaneous Method for 2D and 3D Aerodynamic Flow.” PhD thesis. Rijksuniversiteit Groningen, 2001.

[52] A.E.P Veldman. “Quasi-Simultaneous Viscous-Inviscid Interaction for Transonic Airfoil Flow”. In: *AIAA paper* (2005).

[53] A. Savitzky and Golay M.J.E. “Smoothing and Differentiation of Data by Simplified Least Squares Procedures”. In: *Analytical Chemistry* (1964).

[54] P.H. Cook and M.A. McDonald. *Wind Tunnel Measurements in the Boundary Layer and Wake of an Airfoil with a Blunt Base at high Subsonic Speeds*. Tech. rep. RAE, 1984.

[55] M.Drela. “Integral Boundary Layer Formulation for Blunt Trailing Edges”. In: *AIAA paper* (1989).

[56] C.Hirsch. *Numerical computation of internal & external flows*. John Wiley & Sons, LTD, 2007.

[57] G. Strang. *Linear Algebra and Its Applications*. 4th ed. Brooks/Cole, 2004.

[58] L. Armijo. “Minimization of functions having Lipschitz continuous first partial derivatives”. In: *Pacific J.Maths* 16 (Jan. 1966).

[59] R. Narasimha and A. Prabhu. “Equilibrium and Relaxation in Turbulent Wakes”. In: *Journal of Fluid Mechanics* (1972).

[60] H.B. Squire and A.D. Young. *The calculation of the profile drag of aerofoils*. Tech. rep. A.R.C., 1938.

[61] M Drela and H Yougren. *Xfoil*. Version 6.99.

[62] F. Palacios et al. "Stanford University Unstructured (SU2): An open-source integrated computational environment for multi-physics simulation and design". In: *AIAA Journal* (2013).

[63] T.D. Economon et al. "Stanford University Unstructured (SU2): An open-source suite for multi-physics simulation and design". In: *AIAA Journal* (2016).

[64] Stanford University Unstructured (SU2). `https://su2code.github.io/`. Version 7.0.6.

[65] P.R. Spalart and S.R. Allmaras. "A One-Equation Turbulence Model for Aerodynamic Flows". In: *AIAA paper* (1992).

[66] S. C. Cakmakcioglu, O. Bas, and U. Kaynak. "A correlation-based algebraic transition model". In: *Journal of Mechanical Engineering Science* (2018).

[67] H. Ozdemir et al. "Unsteady Interacting Boundary Layer Method". In: *AIAA paper* (2017).

[68] M.B. Bieterman et al. *Boundary layer coupling in a general configuration full potential code*. Tech. rep. Boeing, 1994.

[69] A. van Garrel. *Integral boundary layer methods for wind turbine aerodynamics*. Tech. rep. Netherlands Agency for Energy and the Environment, 2003.

[70] M. Drela. "Three-Dimensional Integral Boundary Layer Formulation for General Configurations". In: *AIAA paper* (2013).

Appendix A

Numerical simulation

A.1 Convergence analysis of *SU2*

The convergence analysis of *SU2* was based on the inviscid compressible attached flow around the NACA 0012 at an angle of attack $\alpha = 5°$ and a Mach number $M_\infty = 0.5$. The convergence is done on the mesh size n and the monitor criteria are the lift coefficient c_l and the drag coefficient c_d. Tab. A.1.1 lists the solutions of the mesh analysis,

n	c_l	c_d
0.0100	0.6496	0.00929
0.0050	0.6989	0.00243
0.0025	0.7127	0.00139
0.0020	0.7065	0.00147

Table A.1.1: Mesh convergence of *SU2*.

The drag coefficient converges at less than one drag count between the third and the fourth mesh sizes but the lift coefficient still varies. However, the difference in the pressure coefficient distribution is negligible and the fourth mesh is used for the simulation of both the NACA 0012 compressible case and the RAE 2822 highly compressible case.

A.2 RANS simulation

First of all, *SU2* needs an inflow turbulence intensity Tu to start the simulation. Eq. 2.2.27 relying the critical amplification ratio N_{crit} to the freestream turbulence has been used. To remain coherent with the viscous-inviscid interaction of *Flow*, the critical amplification ratio was set to 9. Then,

$$Tu = \exp\left(\frac{-8.43 - N_{\text{crit}}}{2.4}\right), \tag{A.2.1}$$

$$= 0.07\%, \tag{A.2.2}$$

which is a correct value for external flows.

Then, a value of $y^+ \sim 1$ must be ensure on the grid cell such that the first grid point lies in the viscous sublayer. By taking into account a Reynolds number $Re = 6.5 \times 10^6$, the first grid spacing is equal to $\Delta y = 0.00414$ [mm]. The post-processing analysis shows a $y^+ \sim 0.9$.

Similarly to the inviscid *SU2*, a convergence analysis of the mesh size at the leading edge n_{LE} and at the trailing edge n_{TE} has been performed with the lift c_l and the drag c_d as convergence criteria. Tab. A.2.1 lists the solutions of the convergence analysis,

$n_{LE} \times n_{TE}$	c_l	c_d
0.005×0.01	0.365	0.0051
0.002×0.005	0.359	0.0045

Table A.2.1: Mesh convergence of the RANS simulation.

In this work, the purpose of the RANS simulation is not to computed with extreme accuracy the flow around the RAE2822 but to compare the global behaviour of the viscous-inviscid interaction with the higher order simulation. Therefore, a variation of 6 lift and drag counts is small enough and the second mesh is keep for the test case.
A triangular mesh was used for the external flow while a quadrangular mesh was used for the boundary layer. Farfield conditions have been imposed on the inlet, outlet, top and bottom part of the domain while no slip conditions has been imposed on the airfoil.